Università degli Studi di Padova

FACOLTÀ DI SCIENZE MATEMATICHE FISICHE E NATURALI

Dipartimento dei Fisica ed Astronomia

Corso di Laurea Magistrale in Fisica

Study of Near-Infra Red (NIR) fluorescence properties of Single-Walled Carbon Nanotubes (SWCNTs) as possible candidates for imaging of some biological objects

Candidato:

Matteo De Rosa

Matricola n. 1057820

Relatore:

Dott.ssa Laura De Nardo

Correlatore:

Prof. Nikolay Uzunov

Anno Accademico 2016-2017

Study of Near-Infra Red (NIR) fluorescence properties of Single-Walled Carbon Nanotubes (SWCNTs) as possible candidates for imaging of some biological objects

March 23, 2017

Contents

Introduction

IInorganic nanostructured materials have been actively pursued in recent years for biological research thanks to their interesting properties. Among them single-walled carbon nanotubes (SWCNTs) are quasi one-dimensional materials with small band-gap that have unique physical and chemical properties for applications in life sciences and medicine, including in vivo sensing and imaging. For the development of biologically applicable fluorescence-based sensors, the important characteristics are the quantum yield, the photostability and the tissue transparency in the sensor emission range. Semiconducting SWCNTs are characterized by a fluorescence emission in the near-infrared (NIR) region, from 820 to 1600 nm, where the absorption by biological tissues is usually minimal (biological tissues allow for relatively high transmission and penetration of NIR light near $\sim 1\mu m$ for detection within an organism or under the surface of tissues). Furthermore SWCNT have demonstrated an essentially infinite photobleaching threshold, with a steady fluorescence emission even under high excitation fluence ($1.3 \times 10^7 \mathrm{Wm}^{-2}$). These two factors render SWCNT ideally suited for in vivo and in vitro sensor applications because the fluorescence in the NIR region produces less autofluorescence background than visible wavelength light and the photostability allows real-time monitoring of SWCNT fluorescence over extended periods of time, while, for comparison, organic fluorophores and even quantum dots undergo photobleaching upon continuous illumination. The ability shown by the SWCNTs to maintain constant fluorescence emission under continuous illumination ensures reproducibility in fluorescence measurements but also permits the possibility to develop sensors with indefinite lifetimes. Despite SWCNTs are considered the only fluorophores to date that do not photobleach over extended periods of time, a previous research of the group of interdisciplinary physics of the Laboratory for Radiopharmaceutical and Molecular Imaging (LARIM) in the National Laboratories of Legnaro (LNL), demonstrated that the fluorescence emission from sodium cholate water solutions of SWCNTs, excited by a laser with a wavelength of 830 nm, diminishes with the time. The dependence of the intensity emission with respect to the storage time was studied for an overall period of 8 hours, keeping the sample in a dark storage at a temperature of 20 °C. The experimental data where fitted with a simple model showing that it could be considered as a two-component process. This first observation suggested the importance to perform a more detailed investigation in order to better understand the processes involved over

a longer time scale. For these reasons the photoluminescence intensity of a SWCNT solution has been investigated as *a function of the storage time and the storage temperature*.

This thesis is organized in two sections. The first section is a descriptive part and it is organized in two chapters.

In the *first chapter* of this thesis a panorama of the possible applications of SWCNTs in biology and medicine are presented. It is explained how SWCNTs surface chemical functionalization play a key role in both enhancing the biocompatibility of these nanoscale objects and imparting them analyte-specific sensing capabilities which can be exploited to use SWCNTs as selective probes and for imaging.In the same chapter it is presented why SWCNTs are particularly suited for bioapplications.

In the *second chapter* a general overview of the main structural descriptors of the SWCNTs is presented, together with an explanation of the physical models that have been employed to describe the optical transitions empirically observed for these carbonic objects.

The second section represents the experimental part and it is organized in two chapters too.

The *third chapter* describes a special measurement compartment realized ad hoc for this experiment, consisting of cuvette holder where the SWCNT solutions can be measured and stored at a fixed constant temperature for periods of time as long as several weeks. The experimental setup is based on two Peltier cells with electronic temperature control and environmental conditions monitoring, capable of controlling temperatures in the range 5°C-50°C.

The *forth chapter* presents the fluorescence emission measurements performed with two different samples of SWCNT. The data have been collected by taking repeated measurements of the emission fluorescence between regular time intervals along the data acquisition for an overall amount of time of about 250 hours, *i.e.,* for a period of ~ 30 times greater than in the previous investigation. In the same chapter we outline the conclusion and the limits of the present investigation and suggest future prospectives.

Chapter 1

Applications of carbon nanotubes in biology and medicine

1.1 Carbon nanotubes (CNTs) generalities

Nanomaterials having dimensions ranging form one nanometer up to several hundred nanometers are comparable with many biological macromolecules, such as enzymes, antibodies and DNA plasmid. With respect to molecular and bulk scales materials, nanomaterials exhibit different physical properties which in these few decades have attracted the interest in several field of research, including biology and medicine. Nanobiotechnology by means of chemical methods links the physical with biological sciences in the development of new tools and platforms for the understanding of biological systems, disease diagnosis and medical treatments [1, 2, 3]. Among these nanomaterials, carbon nanotubes (CNTs) have attracted in the past decades the scientific interest in several fields of study and application thanks to their unique physical, mechanical and chemical properties [4, 5, 6, 7, 8]. A carbon nanotubes, although not produced directly from graphite, can be envisioned as hollow cylinders of graphite sheets [9]. In particular, a single-walled carbon nanotube (SWCNT) is a graphene[1] sheet rolled into a cylindrical shape so that the structure is quasi-one dimensional with axial symmetry, and in general exhibiting a spiral conformation, called *chirality*. These nanotubes can have a diameter of about 0.7-10.0 nm, though the most of the ones experimentally observed have diameters < 2 nm, and they can be considered as one-dimensional nanostructures if the two ends[2]

[1] Graphene is a single, two-dimensional layer of graphite

[2] The ends are often called caps and consist of "hemisphere" of fullerene; each caps is made with six five-membered carbon ring (pentagons) and an appropriate number of six-membered carbon ring (hexagons) that are placed properly in order to fit perfectly the section of the cylinder.

of a carbon nanotube are neglected and the attention is focused on the large aspect ratio of the cylinder (i.e., length/diameter which can be as large as 10^4-10^5) [10]. Another possibility is a multi-walled carbon nanotube (MWCNT), that is a tube comprising several, concentrically arranged single-wall carbon nanotubes. They have similar lengths to the single-wall tubes, but much larger diameters (inner and outer are around 5 and 100nm, respectively, corresponding to $\approx$ 30 coaxial tubes) [9].

Nanotechnology is an interdisciplinary research field involving physics, chemistry, engineering, biology and medicine, that has great potential for early detection, accurate diagnosis, and personalized treatment of diseases. In the last few years SWCNTs, thanks to their attractive and unparalleled physical properties including but not limited to electric conductance, high mechanical stiffness, light weight, transistor behavior, piezo-resistance, thermal conductivity, luminescence, electrochemical bond expansion and their versatile chemistry, as well as their size, shape and structure, have been studied for potential biological applications [11]. SWCNTs (and nanoparticle in general) have dimensions of many order of magnitude smaller than a human cells, and therefore they can offer unprecedented interactions with biomolecules both on the surface of and inside the cells, which may revolutionize disease treatments and diagnosis.

In this introduction different applications and studies conducted in biology and medicine with CNTs are summarized in order to give a panorama of the vast possibility of applications which these nanomaterials represent, leaving to the successive chapters a more physical and formal presentation of these nanoobjects.

1.2 Functionalization of carbon nanotubes for biological applications

When dealing with biological systems there are several aspects that have to be considered. For biomedical applications a compound has to be soluble in aqueous solutions, but unfortunately raw CNTs are not because of they highly hydrophobic surfaces. For this purpose *surface chemistry* or *functionalization* is required to solubilize CNTs and to render biocompatiblity and low toxicity. Surface functionalization can be *covalent* or *noncovalent*.

Under the covalent case falls the chemical reactions by which bonds are formed with the nanotube sidewalls. An example are the oxidation reactions, which form carboxyl groups at the ends of the tube as well as at defects on the sidewalls. A second example are the cycloaddition reactions, which occur into the aromatic sidewalls instead of tube ends and sidewall defects as in the other case. Oxidation reactions produce oxidized CNTs that are soluble in water solutions, but in presence of salts they suffer aggregation due to charge screening effects. Considering that most biological solutions are high salt content, this approach cannot be a suitable choice for biological applications. In order to overcome this limitation a further modification has been introduced by attach-

ing, to the oxydized CNTs, hydrophilic polymers such as poly(ethylene glycole) (PEG). In this way covalent PEGylated SWCNTs are obtained which are stable in biological solutions, and can be used both *in vitro* and *in vivo* applications [13, 27]. Figure 1.2.1 presents different types of covalent functionalization of CNTs. A side effect of the covalent method is that the intrinsic physical properties of the CNTs are often destroyed after the chemical reactions. A consistent decrease of the intrinsic SWCNTs photoluminescence and Raman scattering has been observed after covalent modification, due to the disrupted nanotube structure. Therefore this type of functionalization is not indicated for potential optical applications of SWCNTs [11].

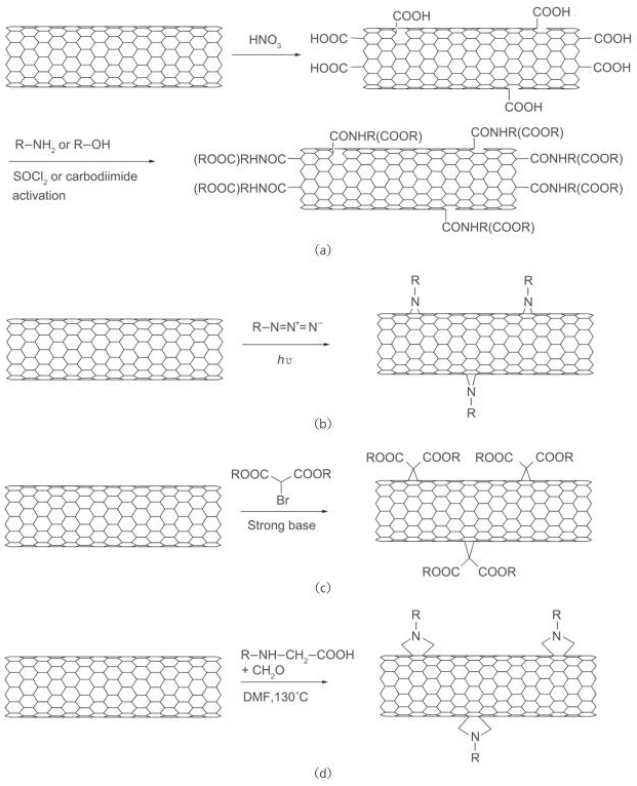

Figure 1.2.1: Schemes of covalent functionalization of carbon nanotubes: (a) CNTs are oxidized and then conjugated with hydrophilic polymers (b) photoinduced addition of azide compounds with CNTs; (c) Bingel reaction on CNTs; (d) 1,3-dipolar cylcoaddition on CNTs. For biological applications, "R" in the figure is normally a hydrophilic domain which renders CNTs water soluble. Further conjugation of bioactive molecules can be applied based on such functionalizations [11]. Taken from [11].

In the noncovalent case favorable interactions between the hydrophobic do-

main of amphiphilic[3] surfactant molecules (or polimers) and the CNT surface are exploited affording aqueous nanotubes wrapped by surfactant. Except for shortening of the tubes, due to the process of sonication needed for this functionalization, the chemical structure of the π-network [4] of carbon nanotubes is not disrupted, and consequently the physical properties are essentially preserved, making this noncovalent approach promising for imaging and multiple biomedical applications. A few methods used for this type of SWCNT functionalization are schematically presented in figure 1.2.2 [11]. A way that has been used is to bind aromatic molecules to the polyaromatic graphitic surface of the SWCNTs. This method exploits the $\pi - \pi$ interaction between aromatic molecules (such as single-strand DNA, pyrene and its derivatives) and the nanotubes surface [14, 28, 29, 30, 31]. Another possibility that has been used is to suspend CNTs in aqueous solution by mean of amphiphiles. The amphiphiles hydrophobic parts are attached to the nanotube surface via van der Waals interactions and hydrophobic effects, while the polar heads are oriented toward the aqueous phase. An example is given by the noncoavalent functionalization of SWCNT by PEGylated phospholipids (PL-PEG). Being the phospholipids the major cell membrane component, they guarantee biocompatibility. The two hydrocarbon chains of the lipid are strongly attached to the nanotube surface with the hydrophilic PEG chain extending in the aqueous phase, giving water solubility. Ideally well noncovalent functionalized SWCNT should be able to meet some important general aspects needed for biological applications. For example biocompatibility, nontoxicity, and sufficient stability are characteristics required to resist detachment from the nanotube surface in biological solution. Furthermore the amphipathic coating molecules should have very low critical micelle[5] concentration (CMC)[6] so that the nanotube coating would result stable after removal of most of the excess coating molecules from the CNT suspension. Finally, the coating molecules should have functional groups which are available for bioconjunction with antibodies or other molecules to create various functional CNT conjugates for different biological applications [11]. Functionalized SWCNTs meeting the above characteristics have been used in several biomedical applications including biological sensing, imaging, drug delivery *in vitro* with cells and *in vivo* with animals [13, 14, 15, 16, 17, 18, 19, 20].

[3] *amphiphilic or amphipathic* is a term describing a compound having both hydrophilic and lipophilic properties[12]

[4] The π-network refers to the structure formed by the π bonds on the carbon nanotubes surface, which are formed by $sp^2 - hybridization$. A more detailed explanation is given in 2.3.

[5] Surfactants in solution are often association colloids, *i.e.*, they tend to form aggregates of colloids dimension, which exist in equilibrium with the molecules or ions from which they are formed [12]

[6] concentration of the surfactant molecules above which micelles are formed and all additional surfactant added to the system go to micelles [12]

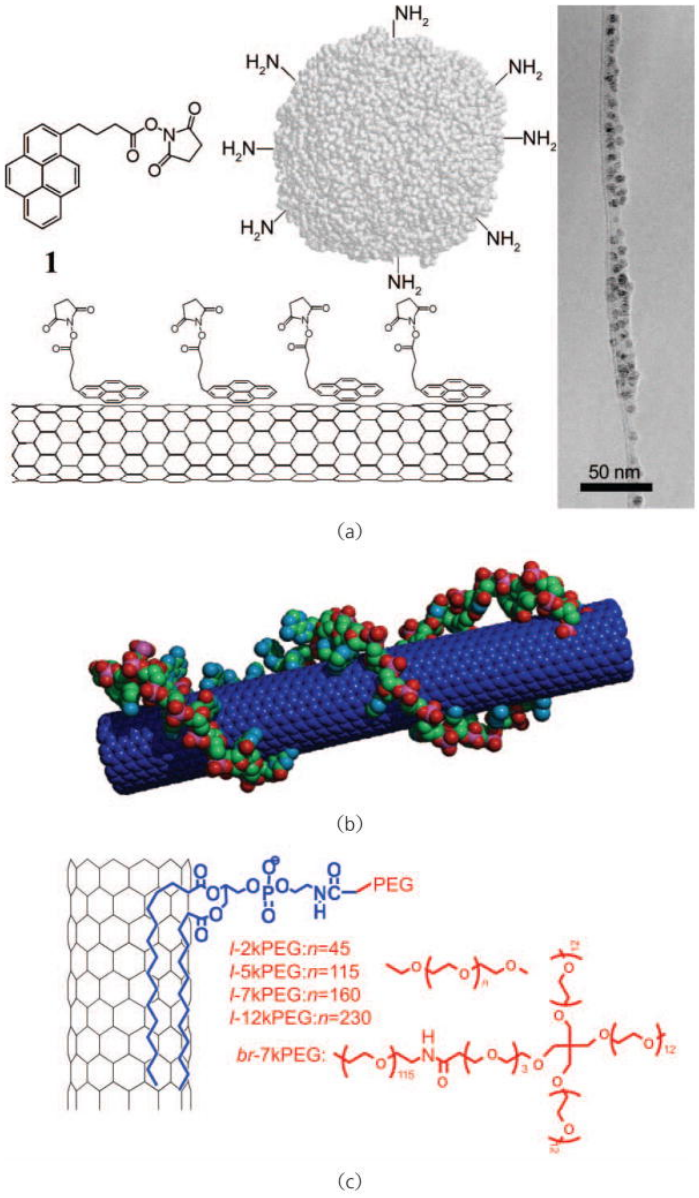

Figure 1.2.2: Schemes of noncovalent functionalization of SWCNTs. (a) Proteins are anchored on the SWNT surface via pyrene $\pi-\pi$ stacked on a nanotube surface. Right: A transmission electron microscope (TEM) image of an SWNT conjugated with proteins [11]. Copyright 2001 American Chemical Society [28]. (b) A SWNT coated by a single-stranded DNA via $\pi-\pi$ stacking [11]. Copyright 2005 the National Academy of Sciences [14]. (c) A SWNT functionalized with PEGylated phospholipids [11]. Copyright 2005 the National Academy of Sciences [19]. Taken from [11].

1.3 CNTs Toxicity

As previously anticipated, biocompatibility and nontoxicity, or more directly safety, is the first requirement for any material used in medicine. For this reason many of the research conducted on these nanomaterials have explored their potential toxic effects. The conclusions acquired varied consistently, depending on the type of the nanomaterial used and on the functionalization methodology adopted. Unfunctionalized raw nanotubes were shown to be toxic to mice after inhalation and intratracheally instilled into animals, showing obvious pulmonary toxicity including unusual inflammation and fibrotic reaction due to the aggregation of hydrophobic raw CNTs into the lung airways [21, 22, 23, 24]. On the contrary various studies conducted both *in vitro* and *in vivo* by several groups have shown no obvious toxicity of properly functionalized carbon nanotubes [25, 26, 27, 29, 32]. Therefore the current status seems to be that toxicity depends on the material preparation, especially geometry and surface functionalization. Carefully functionalized CNTs with a biocompatible surface coating have been demonstrated to be nontoxic *in vitro* and *in vivo* in mice [11].

1.4 Delivery of biomolecules by carbon nanotubes

Functionalized CNTs can be exploited for drug delivery of biomolecules, thanks to their ability to enter cells by themselves without obvious toxicity [25, 33]. Depending on the nanotubes size and functionalization, the CNT cellular absorbing mechanism may undertake different ways including endocytosis and passive diffusion [25, 34, 35, 36, 37, 38, 39]. CNTs have been used to deliver several types of biological objects, ranging from small drug molecules to biomacromolecules, such as proteins, DNA and RNA into different types of cells and with different techniques to link the cargoes onto the CNTs , exploiting covalent and noncovalent approaches [11]. Once taken inside the cell by a endocytosis process, the SWCNTs are able to exit cells through exocytosis [38]. Targeting ligands have been used to target CNTs to specific types of cells *in vitro* or to tumors *in vivo [13, 14, 15, 18, 40]* . To deliver targeted drug with CNTs it is necessary the conjunction of both targets and drug molecules to the same nanotube, operation that requires special designed strategies [11, 13, 40]. While various small drug molecules are able to diffuse into cells, biomacromolecules, including proteins, DNA and RNA, rarely cross cell membrane by themselves. In order to use these macro-objects for therapeutic applications it is necessary to use intracellular delivery. Protein can be either conjuncted or noncovalently absorbed on nanotubes for this purpose. Once the protein has been translocated inside the cell by the nanotube, it can become bioactive after being released from endosomes. CNTs can be modified with positive charges to bind DNA plasmids for gene transfection. Small interfering RNA (siRNA) can be bind to a CNT, forming a CNT-based siRNA delivery, which have shown efficacy *in vitro* and even *in vivo* [11, 41].

1.5 Biological imaging using CNTs

The particular properties of the CNTs make them useful as optical probes for biological and molecular imaging. Molecular imaging , in particular, can be defined as "the visualization, characterization and measurements of biological processes at the molecular and cellular levels in human and other living system" [42]. This field takes advantage of traditional imaging techniques (*i.e.,* molecular magnetic resonance imaging (MRI), magnetic resonance spectroscopy (MRS), optical bioluminescence, optical fluorescence, targeted ultrasound, single photon emission computed tomography (SPECT), and positron emission tomography (PET)) and molecular imaging agents to measure the expression of indicative molecular markers at different stages of disease. CNTs have been explored in almost every single molecular imaging modality, including several others such as Raman spectroscopy and photoacustic tomography (PAT).

In the MRI technique protons (or other nuclei) of a certain tissue are excited by means of an external field, and their interaction with each other and with the surrounding molecules is detected. The image is obtained exploiting the endogenous contrast arising from the different relaxation times of different tissues. To amplify these relaxation time discrepancies, some exogenous contrast agents can be used. Moreover one can selectively choose to enhance the longitudinal or transverse relaxation time in relation to the particular agent selected. Traditionally, Gd^{3+}-chelates have been used to enhance the first and iron oxide nanoparticle for the second. The MRI efficacy of Gd^{3+}-funtionalized SWCNT was found to be forty times grater than Gd^{3+}-based contrast agent in current clinical use. Moreover, it was discovered that these Gd^{3+}-containing SWCNT are also sensitive to the pH value of the environment, very stable, and maintain their integrity when challenged by buffer solution, serum, heat, as well as pH cycling. For these reasons Gd^{3+}-containing SWCNT might be useful in early detection of cancer, where the extracellular pH of tumors can drop to pH 7.0 or below. The inherent MRI low sensitivity can be partially compensated by operating with high magnetic fields (4.7T-14T), exploiting longer time acquiring data period, or by means of contrast agents. Currently it is unclear if Gd^{3+}-containing SWCNT can be molecularly targeted for *in vivo* studies, therefore further investigations are needed before clinical applications [43].

Individual semiconducting SWCNTs have small band gaps on the order of $\sim$ 1eV, depending on the diameter and chirality of a given nanotube. This band gap allows for fluorescence in the NIR range (900-1600nm) which is particularly useful in biological imaging because it could exploit the so called *tissue transparency window*, which is a optical window that characterizes all the biological tissues where they show high optical transparency, between near 800 and 1000nm, and simultaneously low autofluorescence. Furthermore SWCNT are characterizes by a large separation between the excitation (550-850nm) and the emission bands (900-1600nm) which ulteriorly reduces the background from autoflourescence and Raman scattering [11, 43]. Moreover SWCNTs NIR fluorescence does not photobleach under high excitation power, so that SWNT-based sensors could persist indefinitely [11]. On the contrary conventional biological

fluorophores, including fluorescent quantum dots, typically emit fluorescence at visible wavelengths and often photobleach rapidly. Considering that tissues are strongly absorbing and autofluorescent at visible wavelengths, SWCNT-based sensors for biological purposes could outperform conventional visible wavelength fluorophores in biological tissues [44]. Initially raw SWCNTs (bundle of SWCNTs containing several species of SWCNT bind together by van der Waals forces) were analyzed in order to obtain photoluminescence but without obtaining great results. Successively NIR flourescence from micelle-encapsulated SWCNT was demonstrated [45]. Taking advantage of their intrinsic fluorescence, nonspecific uptake of SWCNTs in phagocytic cells have been studied [47]. Later NIR fluorescence was used to track endocytosis and exocytosis of SWCNTs in NIH-3T3 cells in real time [38]. Moreover a bio-inert PEGylated SWCNTs conjugated with antibodies was developed as NIR flourescent tags for selective probing of cell surface receptor (see figure 1.5.1). This demonstrated both how this functionalized nanomaterial opportunely designed was good for selective probing of cell surface receptors and how SWCNTs was a good imaging NIR fluorophore [15].

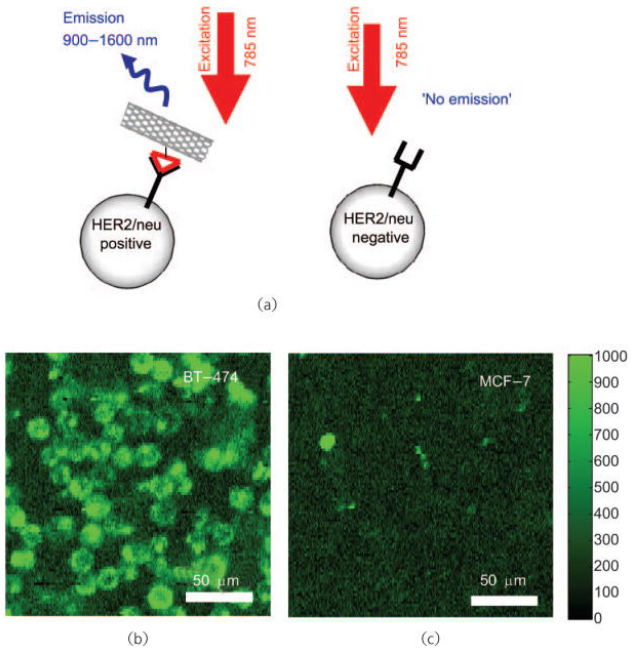

Figure 1.5.1: SWCNT as NIR fluorescent labels. (a) Schematic of targeting cells with SWCNT-antibody (Herceptin) conjugate. (b) NIR photoluminescence image of antigen-positive (HER2/neu positive) cells treated with the SWNT-antibody conjugate. The high level of fluorescence signal indicates surface binding of the SWNT-antibody conjugate. (c) NIR photoluminescence image of antigen-negative (HER2/neu negative) cells. Very little NIR signal is seen owing to the low non-specific binding of the SWNT-Herceptin conjugate and low cellular autofluorescence. Copyright 2008 American Chemical Society [15]. Taken from [11].

NIR Fluorescence imaging of nanotubes was first reported inside a small living animal such as the Drosophila melanogaster (fruit flies), where larvae were fed by food containing SWCNT and imaged by NIR fluorescence microscopy. The NIR fluorescence signal of SWCNT was imaged both in intact living larvae (see figure 1.5.2), and in dissected tissue specimens, structurally identified and counted to estimate the biodistribution [46]. Successively, in one study, chemically pristine SWCNTs were intravenously injected to rabbits and monitored ex vivo through their characteristic NIR fuorescence signal in the blood sample and excised tissue[48]. In a more recent work the high relative quantum yield of SWCNTs dispersed in sodium cholate was combined with the biocompatibility of SWCNTs dispersed in phospholipid-polyethylene glycol (PL-PEG) . These exchange-SWCNTs conjugates were then used as a NIR fluorescence contrast agent for target cell imaging and as *in vivo* NIR fluorescence imaging agents in live mice [32].

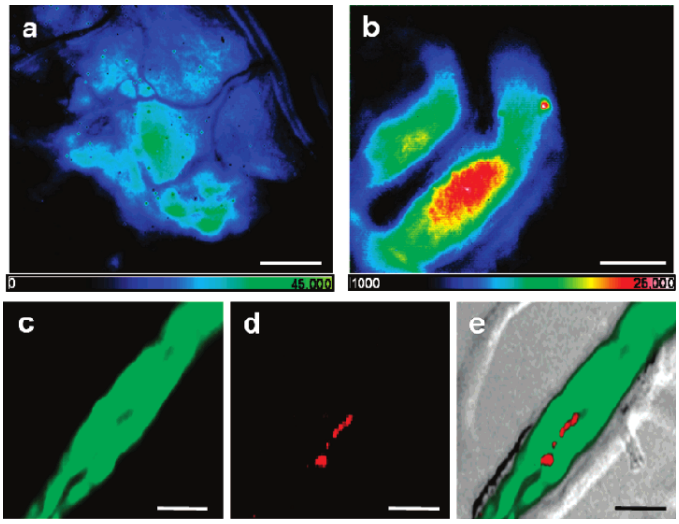

Figure 1.5.2: SWCNTs in the Drosophila gut and blood system. (a,b) NIR emission (color-coded for intensity) from SWCNTs in the gut of a living larva viewed through the larval cuticle. (b) Boluses of food containing SWNTs in a loop of the gut of a living larva. (c, d, e) SWNT NIR emission showing accumulation in the dorsal vessel. (c) Green fluorescence from green fluorescent protein expressed exclusively in the dorsal vessel. (d) NIR fluorescence from nanotubes (false colored in red). (e) Overlay of these two images on the corresponding bright field image[46]. Taken from [11].

In addition to SWCNTs fluorescence direct detection in immunoassy formats, other studies have demonstrated the possibility to use *band gap modulation* and *charge transfer effect* via photoluminescence for transduction and quantification of specific biomolucules. In one of these studies SWCNT noncovalent functionalized with 24-mer ssDNA [7], the dielectric constant at the SWCNT surface is altered by hybridiation of cDNA in proximity of the SWCNT surface, producing an increase of the band gap energy by 2meV. This bang gap variation was observed as blue shift in the emission [49]. The same research team demonstrated, utilizing a similar noncovalent modification strategy, signal transduction via fluorescence quenching for measuring glucose concentration at physiologically relevant condition [50]. Moreover, via photoluminescence, direct detection of protein binding events by relief of band gap fluorescence quenching have been shown. Small molecule quencher may be removed from the surface of SWCNTs by avidim and albumin in a specific and non-specific manner respectively [51].

Due to poor penetration and intense scattering of NIR light, SWCNTs flu-

[7] 24-mer ssDNA is a oligonucleotide, *i.e.*, a short DNA or RNA molecule, oligomer, which are characterized by the sequence of nucleotide residues that make up the entire molecule. The length is usually denoted by "-mer" (from Greek *meros*, "part"), and express the number of nucleotides in the molecule. Therefore 24-mer ssDNA is a small bit of single strand DNA having a length of 24-mer or 24 nucleotides.

orescence approach can be used only for clinical applications in tissues and lesions close to the surface of the skin, or tissues accessible by endoscopy, and intraoperative visualization. For these reasons, SWCNTs fluorescence imaging is more suited for imaging involving cell- or small animal-based applications [43]. Moreover careful preparation techniques are needed in making suspension of pristine, unbundled SWCNTs in bio-inert coatings to optimize the SWCNTs quantum yield in order to maximize their potential as effective fluorophores. Many factor can affect the quantum yield, such as exciton quenching by bundle [52], sidewalls defects [53], and length [54], and several studies have found contradictory results which differ about an order of magnitude [45, 55, 56], therefore further studies are needed to clarify this aspect.

Another technique that is acquiring a great success is the Raman spectroscopy, which can differentiate the "spectral fingerprint" of many molecules, having excellent multiplexing capabilities. Raman spectra are characterized by narrow spectral features, which can be easily distinguished from the autofluorescence background since this is an anelastic scattering process instead of an absorption/emission imaging. However this technique has a low sensitivity due to the inherent weak magnitude of the Raman scattering effect, which hampers the possible employ of Raman spectroscopy for biomedical application [43]. SWCNTs exhibit strong resonance Raman scattering , presenting a Raman spectra characterized by intense and sharp peaks, such as the radial breathing mode (RBM) and tangential mode (G-band) [57]. These peculiar spectra together with the robustness of the Raman signals against photobleaching, allow long term imaging acquisition and tracking [11, 35, 19], and make this technique suitable for optical imaging. Exploiting the RBM peak or the G-band, Raman microscopy has been used for imaging SWCNT in liver cells and tissue slices [35, 19, 20, 27]. Another study has exploited the fact that SWCNTs with different isotope composition evidence shifted G-band peaks for creating "colored SWCNTs" that can be used as multicolor contrast agents. SWCNTs of the same isotope are conjugated with a specific targeting ligand. In this fashion each "colored SWCNT" will target only a specific receptor among various cells having different receptor profiles. Using different colored SWCNTs it is possible to obtain multicolor Raman imaging of cells (see figure 1.5.3)[58].

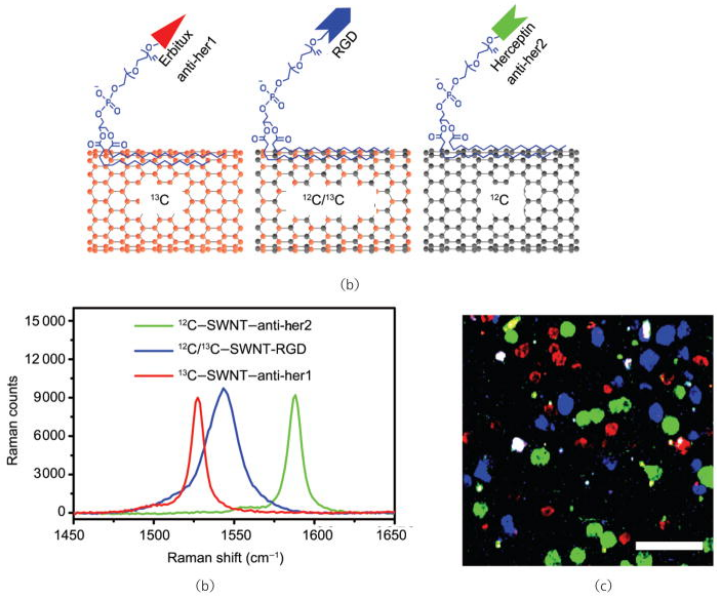

Figure 1.5.3: Multi-color Raman imaging with isotopically modified SWNTs. (a) Schematic illustration of SWNTs with three different isotope compositions conjugated with different targeting ligands. (b) Different G-band peak positions relative to each "colored SWCNT". (c) A deconvoluted confocal Raman spectroscopy image of a mixture of three cell lines with different receptor expressions incubated with the three-color SWNT mixture. Copyright 2008 American Chemical Society [58]. Taken from [11].

Tumor imaging *in vivo* using SWCNTs as Raman probes has been conducted in live mice (see figure 1.5.4). RGD[8] conjugated PEGylated SWCNTs have been intravenously injected into living mice bearing a tumor xenograft, showing strong Raman signals in the tumor, while low signal have been observed after the injection of non-targeted SWCNTs [60, 61].

The peculiarity of the SWCNTs to have strong absorption for visible and NIR wavelengths, have opened new opportunities for the nano-objects to be used in photothermal treatments to kill cancer cells and photoacoustic imaging. NIR laser irradiation of SWCNTs has been used to cause cell destruction with specific SWCNT internalizaton [14, 62]. In photoacustic tomography (PAT), the photoacustic effect is exploited to obtain cross-sectional imaging. Irradiating the tissues by means of a short-pulsed laser beam, the light absorbed is firstly converted into heat, and then the tissues thermoelastic expansion converts the heat in a rise of pressure. The raising pressure propagates via tissues as an ultrasonic wave, which is detected and converted in electronic signals by mean

[8] Arginylglycylaspartic acid (RGD) is a tripeptide that constitute a major recognition system for cell adhesion[59]

of ultrasonic transducers placed on the tissues surface. SWCNTs can be used as photoacustic contrast agent for imaging purpose [43]. This technique has higher spatial resolution with respect to traditional ultrasound systems, and deeper tissues penetration capabilities than fluorescence imaging [63]. RGD-conjugated SWCNTs have been used as PAT contrast agents in molecular imaging of cancer in a mouse tumor model (see figure 1.5.4)[64]

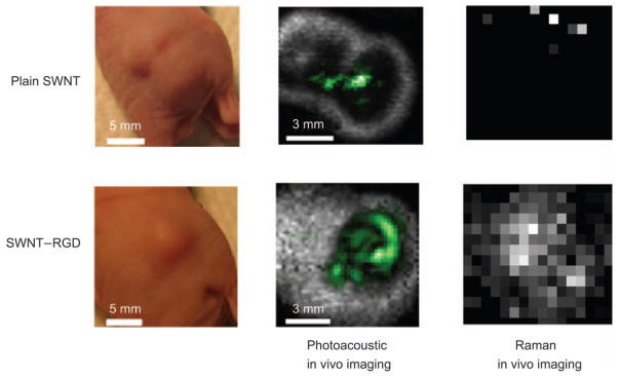

Figure 1.5.4: In vivo tumor imaging with SWNTs. In vivo photoacoustic and Raman images of tumors in live mice. Copyright 2008 American Chemical Society [61], 2008 Nature Publishing Group [64], and 2008 the National Academy of Sciences [60]. Taken from [11].

Finally some words must be spent about the radionuclide-based imaging using SWCNTs. Imaging technique based on radionuclide (such as PET and SPECT) are extensively used in daily medical activity, therefore from a clinical point of view they have a higher relevance with respect to other optical imaging techniques. A favorable aspect is that PET and SPECT do not suffer tissue penetration limit, and are both sensitive (down to picomolar level) and quantitative. A low mass amount of radiolabeled pharmaceuticals are administered through inhalation, ingestion or injection. Gamma camera can be used in planar imaging to obtain 2D images, or in SPECT imaging to obtain 3D images. The use of lead collimators, which defines the angle of incidence, make the SPECT detection efficiency very low. PET, on the contrary, has higher detection efficiency (up to $\sim 10\%$) [43]. In a study of *in vivo* tumor targeting, SWCNTs with two different PEG coatings conjugated with both RDG peptide and radiolabels ($^{64}\mathrm{Cu}-\mathrm{DOTA}$) have been monitored by micro-PET over time after being injected into mice (see figure 1.5.5). It was found that the SWCNTs functionalized in this fashion are highly stable *in vivo* and the PEG chain length can significantly affect the blood circulation time and as a consequence the biodistribution. RGD-conjugated SWCNTs with long PEG coating have shown relatively long circulation half life (about 2 hours) and low uptake by the RES (reticuloendothelial system) [18, 43]. In another study, PET imaging was carried out to evaluate the tissue biodistribution and pharmacokinetics of ^{86}Y la-

beled SWCNTs in a mouse model. It was found that ^{86}Y cleared from the blood in about 3 hours and distributed predominantly to the kidneys, liver, spleen and bone. Radiolabeled nanoparticles represent a class of probes that differs from other imaging modalities because it is an indirect method of nanoparticle detection, because the radionuclide-based imaging detects the radiolabel instead of the nanoparticle itself. Considering the fact that the nanoparticle biodistribution is obtained by assessing the localization of the radionuclide, its conjunction with the nanoparticle must be sufficiently stable under physiological condition in order to obtain reliable measurements of the tumor-targeting efficacy and pharmacokinetics. Detachment of the radionuclides from the nanoparticles can cause significant differences between the nanoparticle and the radionuclide distibution [43].

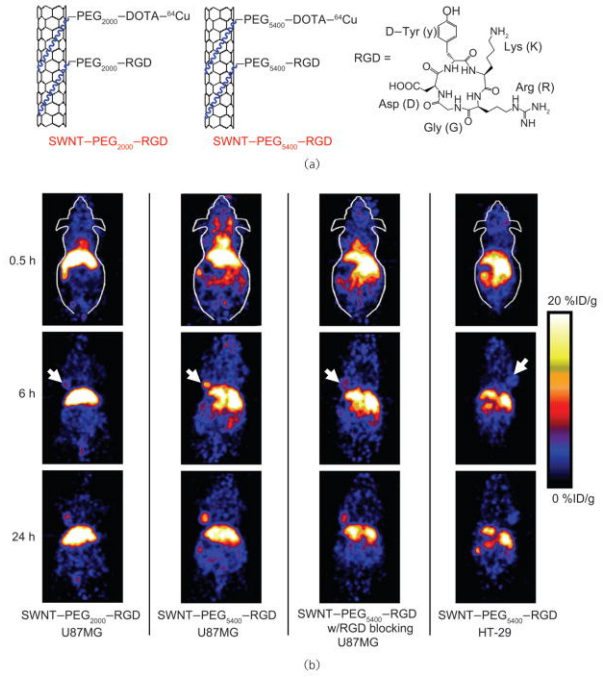

Figure 1.5.5: In vivo tumor targeting with SWNTs. (a) Scheme of PEGylated SWNTs with RGD conjugation and radiolabeling. (b) Micro-PET images of mice. Arrows indicate the tumors. The second column images show how an efficient tumor targeting could only be realized when SWCNTs were coated with long PEG, in contrast to the low tumor uptake visible in the first column images, which are taken with SWNTs coated with shorter PEG chains that have shorter blood circulation time compared to the longer chains, and thus have lower probability to bind to the tumor receptor [11]. The 3rd and 4th column are control experiment. Copyright 2007 Nature Publishing Group [18]. Taken from [11].

Chapter 2

Single-Walled Carbon Nanotubes

2.1 Classification of Carbon Nanotubes

An essential aspect about the structure of a carbon nanotube is the orientation of the six-membered carbon ring in the honeycomb lattice relative to the axis of the nanotube. The direction of the hexagon in the honeycomb lattice can be taken almost arbitrary, without any distortion of the hexagon except for the curvature effect due to cylindrical form of the rolled honeycomb lattice sheet [10]. In order to describe and characterize the different types of nanotubes it's a standard approach to use the descriptor of the honeycomb lattice, thanks to the fact that, from a microscopic point of view, the structure of carbon nanotubes is strictly related to graphene.

When dealing with discrete atoms, ions, or polymer strings of solid matter, the *Bravais lattice* concept is used to formally define a crystalline arrangement. A crystal lattice, by definition, is a *periodic array* of points, where each point is *indistinguishable* from any other and has *identical surroundings*. Consequently, the crystal looks the same when viewed from any equivalent lattice point. The Bravais lattice denotes all the possible crystallographic lattice that can form two- and three-dimensional structures[1] and is defined as a regular periodic arrangement of points in space, all of them connected by translation vectors $\boldsymbol{R}_n = n_1\boldsymbol{a}_1 + n_2\boldsymbol{a}_2 + n_3\boldsymbol{a}_3$, where $\boldsymbol{a}_1$, $\boldsymbol{a}_2$, $\boldsymbol{a}_3$ are the *primitive or fundamental translational vectors* and n_1, n_2, n_3 are any tern of *integer numbers* (negative, positive or zero) .The parallelepiped formed by $\boldsymbol{a}_1$, $\boldsymbol{a}_2$, $\boldsymbol{a}_3$ is called *primitive unit cell*, its volume is $\Omega = \boldsymbol{a}_1 \cdot (\boldsymbol{a}_2 \wedge \boldsymbol{a}_3)$. The honeycomb lattice is not a Bravais lattice, because the latter requires that all lattice sites are equivalent and any vector connecting two lattice sites is a lattice vector. These conditions are

[1] The number of different Bravais lattices is determined by symmetry considerations, in particular the requirements of translational symmetry limit the possible rotation axes therefore restricting as result the effective number of Bravais lattice [95].

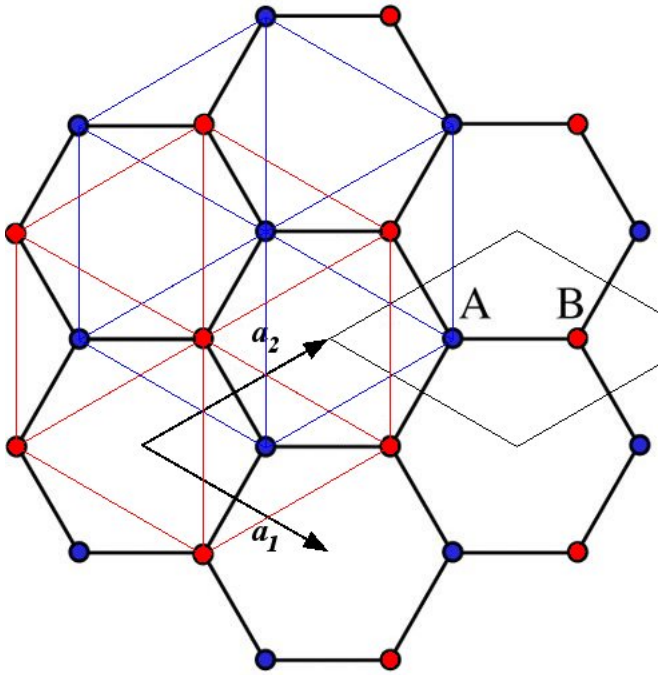

Figure 2.1.1: The honeycomb lattice with the two fundamental translational vector $\boldsymbol{a_1}$ and $\boldsymbol{a_2}$and the honeycomb unit cell (black rhombus). The two inequivalent carbon atoms, labelled as A and B, are colored in blue and red respectively. Also part of the two sublattice, relative to each type of atom, are drawn with the color of the lines consistent with the color used for the atoms.

not satisfied if the honeycomb atom locations are considered as lattice points, in fact it can be easily noticed that it would be impossible to define a lattice translational vector joining a carbon atom with any of its first neighbours, because the opposite of such a vector would point at the center of the hexagons, where no atom exists. The Bravais lattice for the graphene is a hexagonal lattice [93]. The *primitive unit cell of the honeycomb lattice*, containing two inequivalent[2] carbon atoms, is the area characterized by two vectors $\boldsymbol{a}_1$ and $\boldsymbol{a}_2$ having

[2]These atoms, lets call them C_A and C_B for semplicity, are *inequivalent* from a crystallographic point of view. Suppose that a $C_A$atom is chosen as origin and then a translation by a general lattice vector $\boldsymbol{R} = r_1\boldsymbol{a_1} + r_2\boldsymbol{a_2}$ with r_1 , r_2 integers, is applied. The result of the translation will be a shift onto another C_A atom. Same happens if a C_B atom is chosen as the origin. By imagination, by standing onto a C_A or on a C_B point one would see two different panoramas, in particular the two surroundings would be the same if, after moving from C_A to C_B , one would turn of 180°. In this sense C_A and C_B atoms are inequivalent.

magnitude $|\boldsymbol{a_1}| = |\boldsymbol{a_2}| = a_0 = 2.461$Å and forming an angle of 60°[3]. The contents of the unit cell is described by means of an appropriate set of *basis vectors* $\boldsymbol{d}_1, \boldsymbol{d}_2, ..., \boldsymbol{d}_\nu$ which individuate the equilibrium positions of the nuclei of all the atoms (or ions) in the unit cell; for the honeycomb lattice the carbon atoms are at the positions $\boldsymbol{d}_1 = \frac{1}{3}(\boldsymbol{a_1} + \boldsymbol{a_2})$ and $\boldsymbol{d}_2 = \frac{2}{3}(\boldsymbol{a_1} + \boldsymbol{a_2})$. A crystal with two or more atoms (or ions) in the primitive unit cell is called a *composite crystal* (or a *composite lattice*). The honeycomb lattice can be thought as composed by two interpenetrating hexagonal lattices, called *sublattices,* whose lattice points are all the equivalent carbon atom. In fact all the points of a given sublattice are related by translation vectors and thus must be occupied by atoms of the same type. In figure 2.1.1 the two types of carbon atom are shown in two different colors with their relative sublattices.

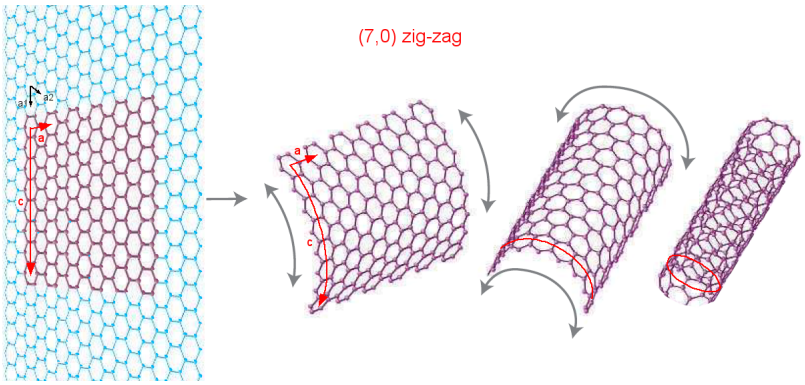

Figure 2.1.2: Schematically construction of a (7,0) SWCNT by means of the graphene rolled up process. Taken from [65].

In carbon nanotubes the graphene sheet is rolled up in such a way that a graphene lattice vector $\boldsymbol{c} = n_1\boldsymbol{a_1} + n_2\boldsymbol{a_2}$ becomes the circumference of the tubes (see figure 2.1.2). Each particular type of nanotubes is uniquely characterized by the so called *chiral vector* $\boldsymbol{c}$, that is usually denoted by the pair of integer (n_1,n_2). Many properties of the tubes vary greatly with the chiral vector for example their electronic band structure or the spatial symmetry or the property to be metallic or semiconducting.

In figure 2.1.3 paying a close attention along the chiral vector, four cycles can be seen. They are lattice points that lay on the chiral vector, and their number $n = GCD(n_1, n_2)$ is given by the great common divisor of (n_1, n_2) , since $\boldsymbol{c} = n\left(\frac{n_1}{n}\boldsymbol{a_1} + \frac{n_2}{n}\boldsymbol{a_2}\right) = n\boldsymbol{c}'$ is a multiple of another lattice vector $\boldsymbol{c}'$,

[3]There are infinite possible choices for the fundamental cell, for this reason usually as unit cell is used the so called *Wigner-Sietz cell*. For composite lattices, the Wigner-Seitz cell about a lattice point is defined by the property that any point of the cell is closer to that lattice point than any other. It can be operatively obtained by bisecting with perpendicular planes the vectors joining one lattice point with the nearest neighbours, second nearest neighbours, and so on, and considering the smallest volume enclosed [93].

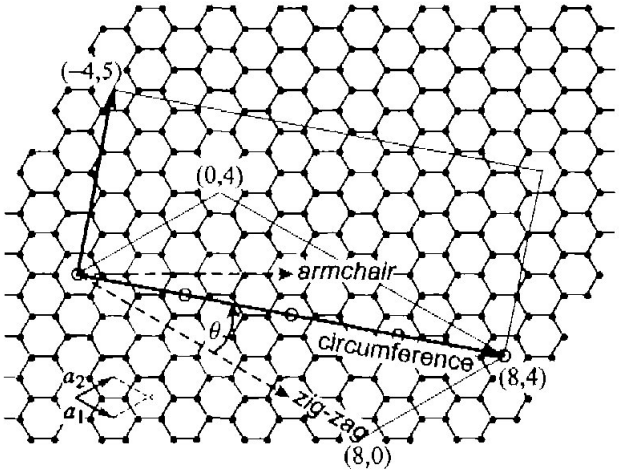

Figure 2.1.3: Graphene honeycomb lattice with the lattice vector $\boldsymbol{a_1}$ and $\boldsymbol{a_2}$. The chiral vector $\boldsymbol{c} = 8\boldsymbol{a_1}+4\boldsymbol{a_2}$ of the (8,4) tube is shown with the four graphene lattice points indicated by circles; the first and the last coincide if the sheet is rolled up. Perpendicular to $\boldsymbol{c}$ is the tube axis z, the minimum translational period is given by the vector $a = -4\boldsymbol{a_1} + 5\boldsymbol{a_2}$. The vectors $\boldsymbol{c}$ and $\boldsymbol{a}$ form a rectangle, if it is rolled along $\boldsymbol{c}$ into a cylinder. The zig-zag and armchair patterns along the chiral vector of zig-zag and armchair tubes, respectively, are shown. Taken from [9].

which in particular is the minimal lattice vector collinear with $\boldsymbol{c}$, and is called *reduced chiral vector*.

The *chiral angle* θ describe the deviation of the chiral vector $\boldsymbol{c}$ from the direction of $\boldsymbol{a_1}$. The expression to calculate θ is

$$\cos\theta = \frac{\boldsymbol{a_1}\cdot\boldsymbol{c}}{|\boldsymbol{a_1}|\cdot|\boldsymbol{c}|} = \frac{n_1 + n_2/2}{\sqrt{n_1^2 + n_1\cdot n_2 + n_2^2}} \tag{2.1.1}$$

For each tube with θ between 0° and 30° an equivalent tube with chiral angle between 30° and 60° is found with the difference that the helix of graphene lattice points around the tube changes from right-handed to left-handed. Because of the six-fold rotational symmetry of graphene, to any other chiral vector an equivalent one exist with $\theta < 60^\circ$. So usually it's common to restrict to the case with $n_1 \geq n_2 \geq 0$ or equivalently $0^\circ \leq \theta \leq 30^\circ$ [9]. Here it is possible to make the first symmetry classification: tubes of the type $(n, 0)$ (or $\theta = 0^\circ$) and (n, n) (or $\theta = 30^\circ$) are classified as *achiral* nanotubes (symmorphic), because their mirror image has an identical structure to the original one. The former go under the name *zig-zag* tubes while the latter are called *armchair*; the names arise from the shape of the cross-sectional ring as shown in figure 2.1.4. On the other hand all the others tubes are *chiral* nanotubes (non-symmorphic), since these types of structures are called axially chiral in the chemical nomenclature

[10].

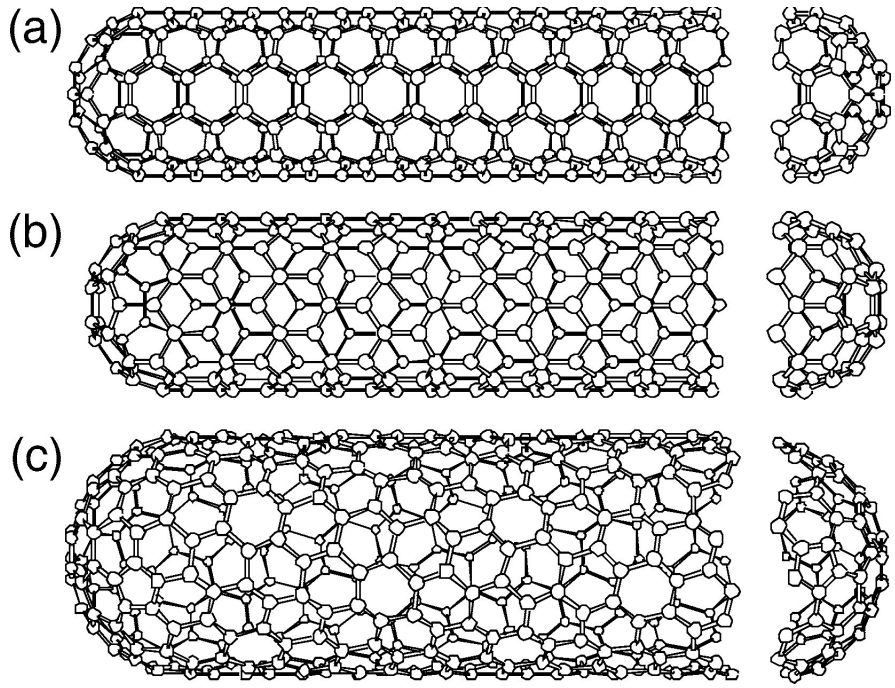

Figure 2.1.4: Schematic theoretical model for the three different types of single-wall carbon nanotubes: (a) the "armchair" nanotube, (b) the "zigzag" nanotube, and (c) the "chiral" nanotube. Taken from [10].

The parameters of the tubes (like diameter, unit cell, number of carbon atoms, and size of the first Brillouin zone) are determined by the geometry of the graphene lattice and the chiral vector. The diameter of the tube is given by the length of the vector $\boldsymbol{c}$

$$d = \frac{|\boldsymbol{c}|}{\pi} = \frac{c}{\pi} = \frac{a_0}{\pi}\sqrt{n_1^2 + n_1 n_2 + n_2^2} = \frac{a_0}{\pi}\sqrt{N} \tag{2.1.2}$$

where $N = n_1^2 + n_1 \cdot n_2 + n_2^2$. In order to define the tubes unit cell we need another vector $\boldsymbol{a}$, that is defined as the smallest vector perpendicular to $\boldsymbol{c}$, and which defines the translation period a along the nanotube axis. For example, for a (8,4) tube the smallest lattice vector along the tube axis is $a = -4\boldsymbol{a_1} + 5\boldsymbol{a_2}$. In general $\boldsymbol{a}$ is determined from the chiral indices (n_1, n_2) by

$$\boldsymbol{a} = -\frac{2n_2 + n_1}{n\mathcal{R}}\boldsymbol{a_1} + \frac{2n_1 + n_2}{n\mathcal{R}}\boldsymbol{a_2} \tag{2.1.3}$$

and

$$a = |\boldsymbol{a}| = \frac{3\sqrt{n_1^2 + n_1 n_2 + n_2^2}}{n\mathcal{R}} a_0 = \frac{3\sqrt{N}}{n\mathcal{R}} a_0 = \frac{3c}{n\mathcal{R}} \tag{2.1.4}$$

where $\mathcal{R} = 3$ if $3(n_1 - n_2)/n$ is an integer, otherwise $\mathcal{R} = 1$. Tubes with the same chiral angle, *i.e.*,with the same ratio n_1/n_2 are characterized by the same lattice vector $\boldsymbol{a}$. At this point the *nanotube unit cell* is fully determined: it is formed by a cylindrical surface with height a and diameter d . It's immediate to verify that for achiral nanotubes the relations 2.1.2 and 2.1.4 can be simplified into

$$\begin{array}{llll} n_1 = n, n_2 = 0 & a_{\mathcal{Z}} = \sqrt{3} \cdot a_0 & |\boldsymbol{c}_{\mathcal{Z}}| = n\, a_0 & (zig - zag) \\ n_1 = n_2 = n & a_A = a_0 & |\boldsymbol{c}_{\mathcal{A}}| = \sqrt{3} \cdot n\, a_0 & (armchair). \end{array} \tag{2.1.5}$$

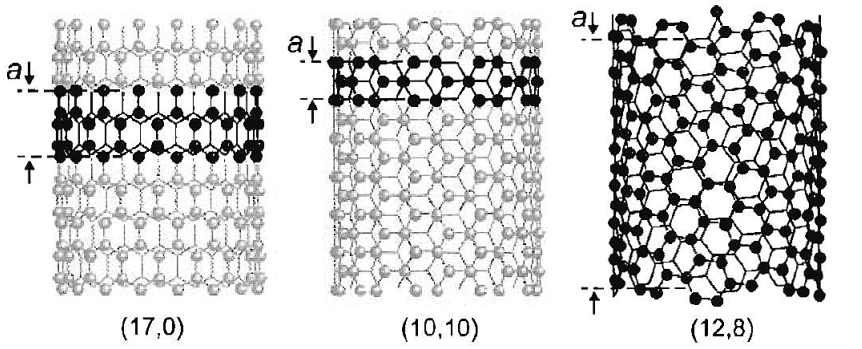

Figure 2.1.5: Structures of (17,0), (10,10), and (12,8) tubes. The unit cell is highlighted in black. Taken from [9].

In figure 2.1.5 are shown the structures of (17,0), (10,10), and (12,8) tubes, where the unit cell is posed in evidence, as well as the translational period a , in order to show how a varies strongly with the chirality of the tube; chiral tubes often have very long unit cell as it could be seen in the figure.

It is possible to calculate the number of carbon atoms in the unit cell n_c , simply taking the ratio between the area $S_t = a \cdot c$ of the cylinder surface ad the area S_g of the hexagonal graphene unit cell

$$q = S_t / S_g = \frac{2N}{n\mathcal{R}}. \tag{2.1.6}$$

Since the graphene unit cell contains two carbon atoms, there are

$$n_c = 2q = \frac{4N}{n\mathcal{R}} \tag{2.1.7}$$

carbon atoms in the unit cell of the nanotube [9]. The structural parameters of armachair, zig-zag, and chiral nanotubes are summarized in Table 2.1.

Table 2.1: Structural parameters of armchair ($\mathcal{A}$) , zig-zag ($\mathcal{Z}$) and chiral ($\mathcal{C}$) nanotubes. Taken from [9].

	Tube	N	$q = n_c/2$
$\mathcal{A}$	(n, n)	$3n^2$	$2n$
$\mathcal{Z}$	$(n, 0)$	n^2	$2n$
$\mathcal{C}$	(n_1, n_2)	$n_1^2 + n_1 n_2 + n_2^2$	$2N/n\mathcal{R}$

	Diameter d	Traslational period a	Chiral angle θ
$\mathcal{A}$	$\sqrt{3}na_0/\pi$	a_0	30°
$\mathcal{Z}$	na_0/π	$\sqrt{3}a_0$	0°
$\mathcal{C}$	$\sqrt{N}a_0/\pi$	$\sqrt{3N}a_0/n\mathcal{R}$	$\arccos((n_1 + n_2)/2)/\sqrt{N}$

2.2 Reciprocal space

For the study of crystals, besides the direct lattice in the ordinary space, it is important to consider also the reciprocal lattice in the dual (or reciprocal) space, because the physical properties are described by dispersion relation in reciprocal lattice space, rather than energy levels [95].

Reciprocal Lattice

Given a crystal with primitive translation vectors $\boldsymbol{a}_1$, $\boldsymbol{a}_2$, $\boldsymbol{a}_3$ in the direct space, we consider the three primitive vectors $\boldsymbol{k}_1$, $\boldsymbol{k}_2$, $\boldsymbol{k}_3$ in the reciprocal space, defined by the relations $\boldsymbol{a}_i \cdot \boldsymbol{k}_j = 2\pi\delta_{ij}$ (the numerical factor 2π is introduced as a matter of convenience to simplify some expressions later on), which defines the orthonormality relation between the primitive real and reciprocal lattice vector. If $\boldsymbol{a}_1$, $\boldsymbol{a}_2$, $\boldsymbol{a}_3$ are non co-planar vectors and form a right-handed system, also $\boldsymbol{k}_1$, $\boldsymbol{k}_2$, $\boldsymbol{k}_3$ are non co-planar vectors and form a right-handed system. All the points defined by the vectors of the type $\boldsymbol{K}_m = m_1\boldsymbol{k}_1 + m_2\boldsymbol{k}_2 + m_3\boldsymbol{k}_3$ constitute the reciprocal lattice, with m_1, m_2, m_3 integer numbers (negative, zero, or positive). The reciprocal lattice is related only to the translational properties of the crystal and not to the basis, which means that crystals with the same translational symmetry, but completely different basis, have the same reciprocal lattice[93]. Exploiting the orthonormality relation given above a more general ortho-normality relation can be obtained, which for a general lattice vector $\boldsymbol{R}_n = n_i\boldsymbol{a}_i$ and a general reciprocal lattice vector and $\boldsymbol{K}_m = m_j\boldsymbol{k}_j$ (i, j = 1, 2, 3) is given by

$$\boldsymbol{R}_n \cdot \boldsymbol{K}_m = 2\pi N_{nm} = 2\pi N_1 \,, \tag{2.2.1}$$

where $N_{nm} = N_1$ is an integer depending on n and m. From this relation it is clear that the reciprocal lattice is characterized by the set of wavevectors $\boldsymbol{K}_m$ satisfying $e^{i\boldsymbol{K}_m \cdot \boldsymbol{R}_n} = 1$, which means that all wave vectors $\boldsymbol{K}_m$ yield plane waves with the same periodicity of the associate Bravais lattice. An important relation that arise from 2.2.1 is $e^{i\boldsymbol{K}_m \cdot (\boldsymbol{r}+\boldsymbol{R}_n)} = e^{i\boldsymbol{K}_m \cdot \boldsymbol{r}}$ that holds for any $\boldsymbol{r}$, and for all $\boldsymbol{K}_m$, $\boldsymbol{R}_n$.

Brillouin Zone

As well as for the real space, where the concept of unit cell has been introduced, in the reciprocal space an anologous of the Wigner-Seitz cell can be introduced and goes under the name of *first Brillouin zone.* In particular the first Brillouin zone (or simply the Brillouin zone) of the reciprocal lattice has the property that any point of the cell is closer to the chosen lattice point than to any other. The first Brillouin zone can be obtained by bisecting with perpendicular planes nearest neighbours reciprocal lattice vectors, second nearest neighbours (and other orders of neighbours if necessary) and considering the smallest volume enclosed. Similarly, the second Brillouin zone is obtained continuing the bisecting operations and delimiting the second volume enclosed (with exclusion of the first zone), etc. The shape of the Brillouin zone is connected to the geometry of the direct Bravais lattice and as well as happens for the Bravais lattice, the number of possible types of Brillouin zone is limited.

SWCNT reciprocal lattice and Brillouin zone

The unit cell of carbon nanotubes has been determined in section 2.1, now it will be considered how to construct their Brillouin zone (BZ).

In the direction of the z-axis, which is also the direction of the tube axis, the reciprocal lattice vector $\boldsymbol{k}_z$ corresponds to the translational period $\boldsymbol{a}$; its length is

$$|\boldsymbol{k}_z| = k_z = 2\pi/a \tag{2.2.2}$$

.

As the tube is considered infinitely long[4] the wave vector $\boldsymbol{k}_z$ is continuous, and the first Brillouin zone in the z-direction is the interval $(-\pi/a, \pi/a]$ [5]. Along the tube's circumference , any wave vector $\boldsymbol{k}_m$ (or $\boldsymbol{k}_\perp$) must satisfy the boundary condition

$$m \cdot \lambda = |\boldsymbol{c}| = \pi \cdot d\,, \tag{2.2.3}$$

and therefore it is quantized according to

[4] In real case being the length L a finite quantity, also the wave vectors $\boldsymbol{k}_Z$ is quantized [10].

[5] It's used the notation where brackets types () and [] indicate open and close intervals, respectively.

$$k_m = \frac{2\pi}{\lambda} = \frac{2\pi}{|\boldsymbol{c}|} \cdot m = \frac{2}{d} \cdot m \tag{2.2.4}$$

where m is an integer taking the values $-q/2+1, ..., 0, 1, ..., q/2$. This boundary condition is understood in the following way : the wave function of a quasi-particle of the nanotube, such as an electron, must have a phase shift of an integer multiple of 2π around the circumference, *i.e.,* an integer number of wavelengths must be contained in the nanotube circumference, otherwise the wave function will vanish by interference. A wave with wave vector $k_m = \frac{2}{d} \cdot m$ has $2m$ nodes around the circumference[6]. The maximum $|k_m|$ (minimum wavelength) follows from the number of atoms in the nanotube unit cell ($n_c = 2q$) : a projection of the carbon atoms on the circumference of the tubes lead to equidistant pairs of them; then at least two pairs of atoms are necessary for defining a wavelength, *i.e.,* $|m| \leq q/2$. Therefore a wavevector of a SWCNT is described by a continuous part k_z, often called the *quasi-linear* momentum, and a quantized part k_m, where the integer m is often referred as *quasi-angular momentum*[7]. In this fashion, the states $|k\, m>$ in the first Brillouin zone are constituted by the q lines parallel to the z-axis separated by $k_m = 2/d$ and $k_z \in (-\pi/a, \pi/a]$. This quantized wave vector $\boldsymbol{k}_m$ and the reciprocal lattice vector $\boldsymbol{k}_z$ are found from the condition

$$\begin{aligned} \boldsymbol{k}_m \cdot \boldsymbol{c} &= 2\pi & \qquad \boldsymbol{k}_m \cdot \boldsymbol{a} &= 0 \\ \boldsymbol{k}_z \cdot \boldsymbol{c} &= 0 & \qquad \boldsymbol{k}_z \cdot \boldsymbol{a} &= 2\pi. \end{aligned} \tag{2.2.5}$$

Using these equations one obtains

$$\boldsymbol{k}_m = \frac{2n_1 + n_2}{qn\mathcal{R}}\boldsymbol{k}_1 + \frac{2n_2 + n_1}{qn\mathcal{R}}\boldsymbol{k}_2 \tag{2.2.6}$$

$$\boldsymbol{k}_z = -\frac{n_2}{q}\boldsymbol{k}_1 + \frac{n_1}{q}\boldsymbol{k}_2 \tag{2.2.7}$$

[6] Recalling the oscillations of a rope of length L with fixed ends, the first oscillation mode (or fundamental, $n = 1$) is give by a wavelength λ_1 equal to $2L$. In general the wavelength of the n-th mode is give by the relation $\lambda_n = 2L/n$, where $n = 1, 2, ...,$ and has $n + 1$ nodes along the rope. Substituting $L = c = \pi d$ and $k_{\perp,m} = 2\pi/\lambda_n$ and making explicit the wave vector magnitude one obtains $k_{\perp,m} = n/d$. Finally noting that in the case of a close rope the first and the last node are coincident, one has n nodes and therefore $n = 2m$ are effectively the number of nodes along the circumference.

[7] A system invariant under a given symmetry always implies a conservation law for a related physical quantity. In solid state physics an example is given by the Bloch's theorem, which states that in the periodic potential of the crystal lattice any wave function takes the form of a travelling plane wave modulated on microscopic scale by an appropriate function having the same lattice periodicity. The quasi-linear momentum k corresponds to the translational period, while the quasi-angular momentum m refers to both pure rotations and screw-axis operations [9].

[9]. With the expression 2.2.6 it is possible to give another explanation of the quantization of $\boldsymbol{k}_m$ seen above: since $q\boldsymbol{k}_m = \frac{2n_1+n_2}{n\mathcal{R}}\boldsymbol{k}_1 + \frac{2n_2+n_1}{n\mathcal{R}}\boldsymbol{k}_2 = (t_2k_1 - t_1k_2)$ corresponds to a reciprocal lattice vector of graphene, two wave vector which differ by $q\boldsymbol{k}_m$ are equivalent. Since t_1 and $t_2$do not have a common divisor except unity[8], none of the $q-1$ vectors $\mu\boldsymbol{k}_m$ (where $\mu = 1, \cdots, q-1$) are reciprocal lattice vector of two-dimensional graphite. Thus the q wave vector $\mu\boldsymbol{k}_m$ (where $\mu = 0, \cdots, q-1$) give rise to q discrete k_m vectors, which arise from the quantized wave vectors associated with the periodic boundary condition on $\boldsymbol{c}$ [10].

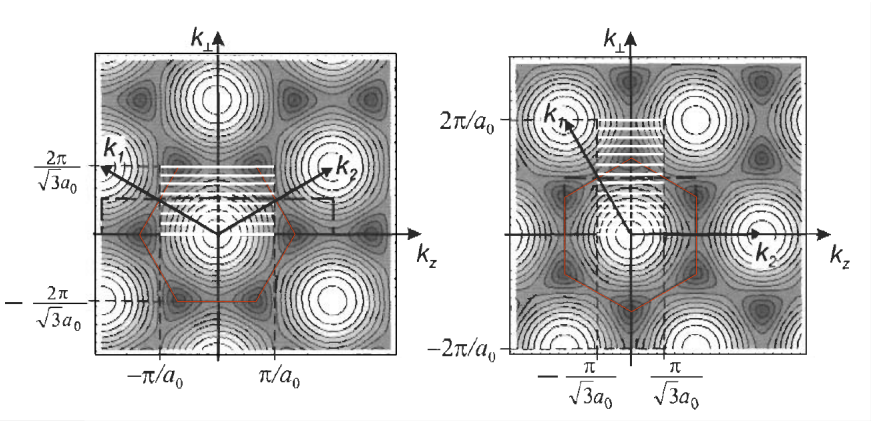

Figure 2.2.1: Examples of Brillouin zone: Shown as white thick lines are reported the BZ of a (7,7) armchair and a (13,0) zig-zag SWCNT. The background is a contour plot of the electronic band structure of graphene,where white indicates the maximum energy. Note that the graphene BZ (*i.e.,* the two heaxagons in red) are rotated one respect to the other by 30°. The nanotube BZ consists of $2n$ lines parallel to k_z (*i.e.*, 14 and 26, respectively), where k_z is the reciprocal lattice vector along the tube axis. Each line is indexed by $m \in [-n, n]$, where $m = 0$ corresponds to the line through the graphene Γ point ($k = 0$). The BZ boundary are given by $\pm\pi/a$ that yields $\pm\pi/a_0$ for armchair and $\pm\pi/\sqrt{3}a_0$ for zig-zag tubes. From the symmetry of the graphene hexagonal BZ, it can be seen that lines with index m and $-m$ are the same, as well as k and $-k$ for the same index m, therefore in the picture are shown only the lines with $n+1 \geq m \geq 0$. Taken from [9].

In figure 2.2.1 are shown the first BZ of a (7,7) armchair and a (13,0) zig-zag nanotube for $m \in [-n, n]$ in relation to the hexagonal Brillouin zone of graphene shown in figure 2.2.2 , where are indicated the high-symmetry points Γ, K and M , and the distances between them. The line through the graphene Γ point has the index $m = 0$. Increasing the diameter the number of lines increases, while their spacing decreases [9].

[8] The demonstration can be found in reference [10].

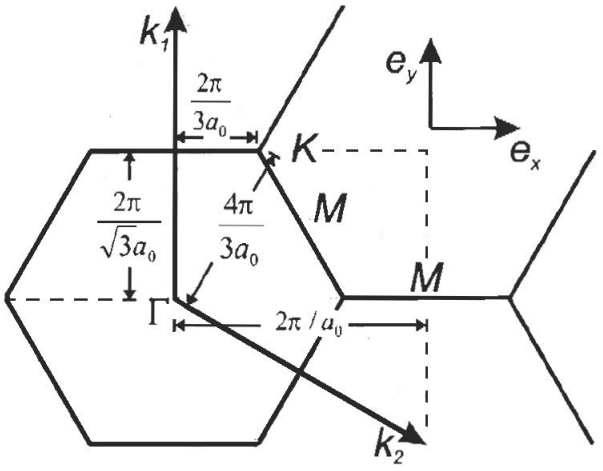

Figure 2.2.2: Graphene Brillouin zone: The high-symmetry points labelled byΓ, K, and M (for a more details about this topic see E.0.3) . The reciprocal lattice vectors k_1 , k_2 in Cartesian coordinates are $k_1 = (0, 1)\, 4\pi/\sqrt{3}a_0$ and $k2 = (\frac{\sqrt{3}}{2}, -\frac{1}{2})4\pi/\sqrt{3}a_0$. Taken from [9].

2.3 Fluorescence properties of SWCNTs

2.3.1 SWCNTs electronic energy bands

As previously described, SWCNT can be envisioned as a graphene sheet that has been rolled up to form a seamless cylinder capped at the ends with hemifullerens. Each carbon atom on this structure is covalently linked to its first neighbors by σ-bonds which lie along the cylinder wall forming the hexagonal network. The remaining p-electron of each atom, that are out of the cylindrical surface, forms with the other p-electron of the other sites an extended π-electron network system[9]. This π-network is responsible for the weak van der Waals interactions between different tubes and its properties have a severe effects on the SWCNT low-energy electronic properties and optical spectroscopy. The π-network available electronic states reflect the unusual band structure of graphene together with the constraint of an angular periodic condition for full rotation about the tube axis. The fact that this wavefunction boundary condition varies with the two integers (n_1, n_2), that characterize each SWCNT, implies that each physical structure has its own characteristic electronic struc-

[9]Carbon is in the IV group element with an electronic configuration $(1s)^2(2s)^2(2p)^2$. In some cases, as for the graphene, the two carbon electronic p-orbitals that are co-planar, namely p_x and p_y, combine with one s-orbital forming three sp^2 electronic orbitals, this phenomenon is called $sp^2 - hybridization$. In this fashion the planar assembly forming the characteristic angles of 120° between the σ-bond with neighbor atoms is obtained. The additional p_z-orbital is perpendicular to the sp^2-hybrid orbitals and forms a π-bond [10].

ture (*e.g.,* the quantity $n_1 - n_2$ is strictly related to the metallic, semi-metallic or semiconducting nature of the SWCNT). Furthermore, due to the fact that SWCNT electronic structure is governed by transverse conformation, tubes with the same pair of integers(n_1, n_2) but different lengths should manifest identical optical and electronic properties [66].

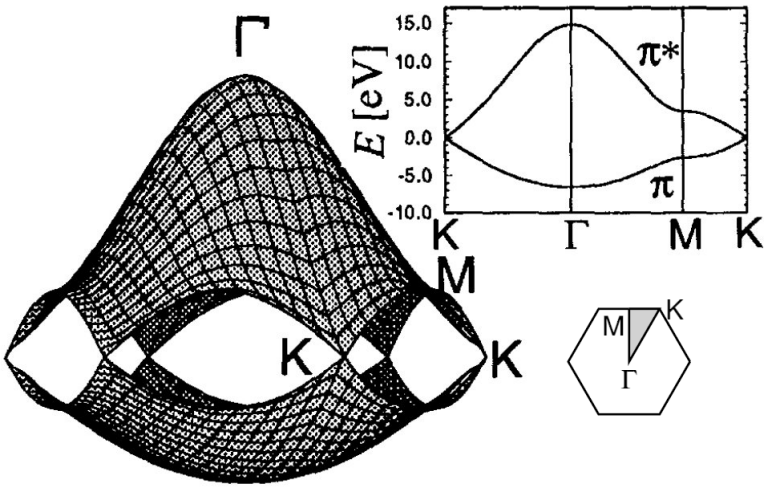

Figure 2.3.1: Energy dispersion relations for graphene shown throughout the whole region of the first Brillouin zone. The upper insert shows these energy dispersion relations along the high simmetry directions of the triangle ΓMK, which is shown in the image below. Taken from [10].

Theoretical research have found the SWCNT electronic energy bands by means of *tight-binding* and *zone-folding* calculations. There are two principal approaches to calculate the electronic energy bands of a material: one implies that the electrons are essentially free to move through the crystal lattice (free-electron approximation) while the other considers the electrons to be part of the atoms that constitute the solid (tight-binding approximation). In the latter case, since the inter-atomic distances are very small, the valence electrons in different atoms interact. As a consequence of this interactions, the electronic eigenstates evolve into the continuous bands of the solid [9]. Firstly, tight-binding approximation have been used to find energy dispersion relations for the electronic band structure of the graphene π-orbitals [9, 10]. Then it has been possible to obtain the electronic band structure of SWCNT π-orbitals exploiting the zone folding approximation. The idea behind this approximation is that the nanotube electronic band structure are given by the graphene electronic energies evaluated along the allowed k-lines that form the nanotube Brillouin zone. As seen in section 2.2, the allowed wave vectors, which form the nanotube Brillouin zone, are the q lines of length $2\pi/a$ and distance $2/d$ parallel to the direction of the tube axis, and are fully determined by the chiral indices (n_1, n_2). As

can be seen in figure 2.3.2, the SWCNT electronic energy bands are found by cutting the two dimensional band structure of graphene by means of these k lines. It must be emphasized that this method, however, neglects any effects of the cylinder geometry and curvature of the tube walls, therefore attention must be paid in those circumstances where these contribution can be crucial. An example of the results given by this method is the discrimination of the metallic or semiconducting character of a SWCNT [9].

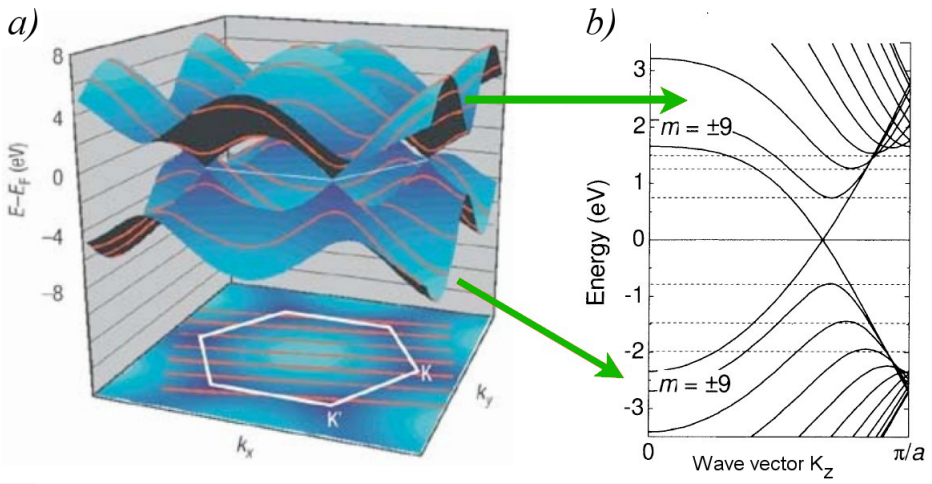

Figure 2.3.2: SWCNT energy bands. *a*) In the lower part of the image graphene and SWCNT first Brillouin zone are depicted. In the upper part is shown the graphene band structure, composed by the conduction band π^* and the valence band π (upper and lower surfaces respectively). The projection of the allowed k states (*i.e.,* the nanotube BZ , shown as orange lines in the k_x, k_y plane) on the graphene electronic band structure yields the SWCNT electronic energy sub-bands (orange lines on the surfaces). *b*) The green arrows shows how, from the graphene conduction π^*-band and valence π-band, SWCNT conduction and valence sub-band are formed. In particular in *b* are shown the energy sub-bands of a (10,10) nanotube, recalling the fact that m ranges in $[-q/2, q/2]$ and $q = 2n$ for an achiral tube, then $m \in [-9, 9]$. Image *a* taken from [65]and image *b* from [9].

2.3.2 Density of states

The density of states (DOS) $n(E)$ is a quantity that represent the number of available electrons for a given energy interval, and its behavior is strictly related to the system dimensionality. Its expression is given by $n(E) = dN/dE$, where N represent the number of occupied states and E is the energy. Figure 2.3.3 shows schematically the DOS dimensional dependence. In 3D systems the

DOS function rises as the square root of the energy, while lowering the system dimension to a 2D case, it manifests a step like function. In a one-dimensional system, as in the SWCNT case, it diverges as the inverse of the energy square root. Finally in zero-dimensional systems the DOS is a δ-function. The density of states is related with optical transitions because it determines at which energies photoluminescence can occur, furthermore a higher DOS determines a higher probability occurrence of a photoluminescence process.

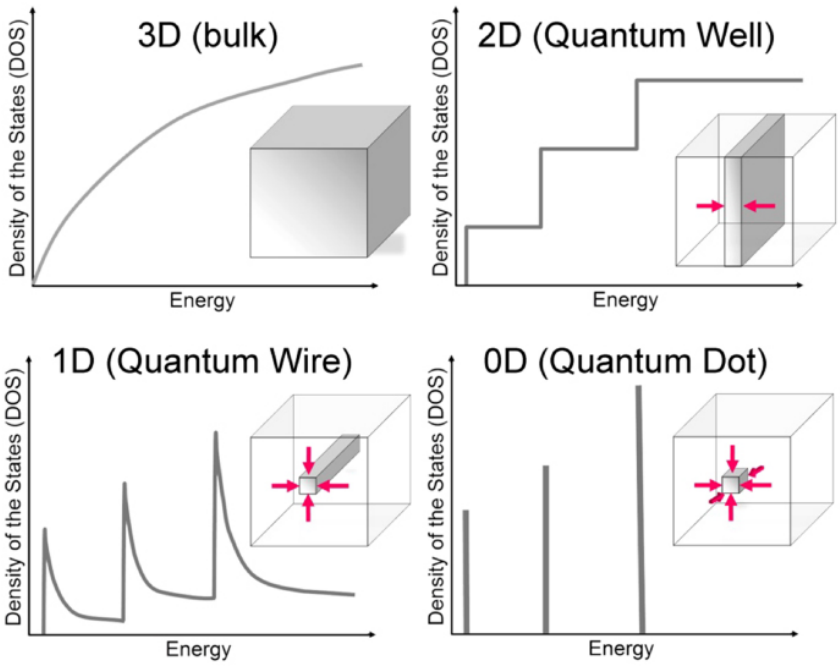

Figure 2.3.3: Schematic representation of the DOS dimensional dependence. Taken from [67].

The quasi-one-dimensionality of the SWCNTs introduce sharp spike into the DOS, which are called *van Hove singularities*. Each van Hove singularity belong to a different sub-band, which is labeled by the quasi-angular momentum m [66]. Dipole-allowed optical transitions, absorption and emission, are governed by symmetry selection rules of the carbon nanotubes [10]. Only vertical transition ($\Delta k \approx 0$) are allowed, and the symmetry selection rules depend on the relative polarization of the electric-field vector $\boldsymbol{E}$ with respect to the tube

[10] Any quasi-particle of the nanotube "feels" the nanotube symmetry. Therefore the wave-function of the quasi-particle transforms, under the symmetry operations, in the same way as the basis functions of the corresponding representation. The transition probability from state $|\alpha>$ to state $|\beta>$ via the dipole-operator X is non zero only if $|X|\alpha>$ and $<\beta|$ have some component of their symmetry in common. If their wave function are orthogonal and therefore do not share any irreducible component the matrix element $<\beta|X|\alpha>$ vanishes and the transition between those two states is not allowed [9].

axis (which is chosen as the z-axis). For light polarized along the z-axis ($\boldsymbol{E} \| \boldsymbol{z}$), the angular momentum quantum number m remains constant ($\Delta m = 0$). For this type of transitions is often used the notation E_{ij}, where i and j indicate the corresponding angular momentum m for the particular sub-band involved. Being $\Delta m = 0$, these longitudinal transitions are of the form E_{11}, and E_{22} (more generally E_{ii} , *i=1,2,3,..)* and they are shown in figure 2.3.4, picture *a*) . For light polarized perpendicularly respect to z ($\boldsymbol{E} \perp \boldsymbol{z}$), only the transitions where m changes by plus or minus one ($\Delta m = \pm 1$) are allowed. In practice the latter transitions are suppressed by polarization charges induced on the cylinder wall, this effect often is called *antenna effect.* In an infinitely long cylinder, an external electric field along the nanotube axis does not induce polarization and the total parallel electric field is equal to the external field. On the contrary, an external field directed perpendicularly respect to the tube axis induces polarization charges on the nanotube cylindrical walls, which reduce the electric field in the perpendicular direction. As a consequence the longitudinal optical electronic transitions (E_{ii}, i = 1, 2, 3,...) are dominant.

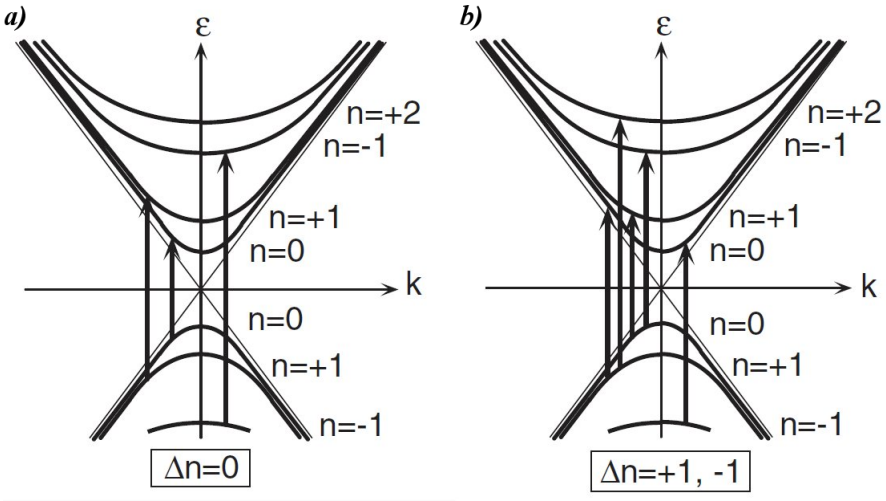

Figure 2.3.4: Representative scheme of semiconducting carbon nanotubes band structure. The allowed optical transitions for the parallel ($\Delta n = 0$) and perpendicular ($\Delta n = \pm 1$) polarization are denoted by arrows (here is used n instead of *m).* Taken from [68].

The term "photoluminescence" describes any process where a system is moved in an excited state by light absorption, and subsequently relaxes to the ground state by emission of light with a lower frequency. In nanotube optics the term fluorescence is more appropriated as it describes "allowed" photoluminescence processes having characteristic times as short as few nanoseconds or less [69]. As can be seen in the simplest physical model of fluorescence graphically sketch in left part of image 2.3.5, the absorption of a quantum of light occurs at E_{22}

(more in general at E_{ii} with *i=1,2,3)*, promoting an electron from the second valence sub-band v_2 (v_i), where a hole[11] is generated, in to the second conduction sub-band c_2 (c_i) . In this fashion electron–hole pairs are created. Electrons and holes relax through phonon emission to the first sub-band, where finally radiative electron-hole recombination across the semiconducting band gap take place with the emission of E_{11} near-infrared fluorescence photons.

The single-particle band structure shown in (a) of figure 2.3.5 is a consequence of the assumption that electron and hole formed by optical excitation are independent. Actually, the electron-hole pair formed by optical excitation are not independent, they can remain spatially associated, via mutual Coulomb interaction[12], forming a bound state called exciton[13]. The excitonic binding energy is the energy required to ionize an exciton in its lowest energy state, that is, the energy separation between the lowest bound excitonic state (bound electron-hole pair, labelled in (b) of 2.3.5 as 1s) and the unbound excitonic state (free electron-hole pair, indicated in (b) of figure 2.3.5 by ∞).

The binding energy of an exciton in a three-dimensional system is given by $E_b = \frac{m^* e^4}{2\hbar^2 \varepsilon^2} = \frac{m^*}{2\varepsilon^2} Ry$, where m^* is the reduced effective mass of the electron-hole pair, ε is the material dielectric constant and Ry is the ionization energy of an hydrogen atom ($1Ry = 13.6$eV). The exciton binding energy in crystal is very much smaller than that for a hydrogen atom, with typical excitonic binding energies of the order of $\approx 10 - 15$meV. This is essentially due to the smaller value of the reduced effective mass m^* of the electron- hole system and the screening of the Coulomb interaction between electron and hole by other particles [70]. However in one dimensional systems, as SWCNTs, the screening of the Coulomb interaction applies only along the nanotube axis, giving binding energy values near 0.4eV (for SWCNTs smaller diameter species). A direct consequence of the excitonic model, is that each optical transition (e.g., E_{11} or E_{22}) and its related bands in the single-particle excitation model generates a set of exciton bands, as is schematically reported in (b) of figure 2.3.5, with its own selection rules. From a mathematical point of view an exciton is equivalent to an hydrogen atom, where the hole replaces the proton. Similar to the hydrogen atom, excitons have an angular momentum which explain the labelling notation for the energy of the excitonic states in (b) of figure 2.3.5. The free-particle states (unbound excitonic states) still exist, but the oscillator strength[14] shifts from the free electron–hole pair to the optically allowed ground-state exciton

[11] In solid state physics, a hole is a positive charge created by the electron vacancy from the valence band that is treated as though it has all the properties of an electron, except for its positive charge.

[12] electron is attracted to the hole by the Coulomb potential energy $-e^2/\varepsilon r$ where r is the distance between them and ε the appropriate dielectric constant. ε determines the screening effect on the potential energy of the background, which consists of all the atoms and any free electrons present [70].

[13] An exciton is a quantum of electronic excitation energy (psuedoparticle) travelling in the periodic structure of a crystal; it is electrically neutral and hence its movement through the crystal gives rise to the transportation of energy but not charge [70].

[14] The oscillator strenght of a spectral line is defined as the probability transition between the ground state and the excited state involved [72]

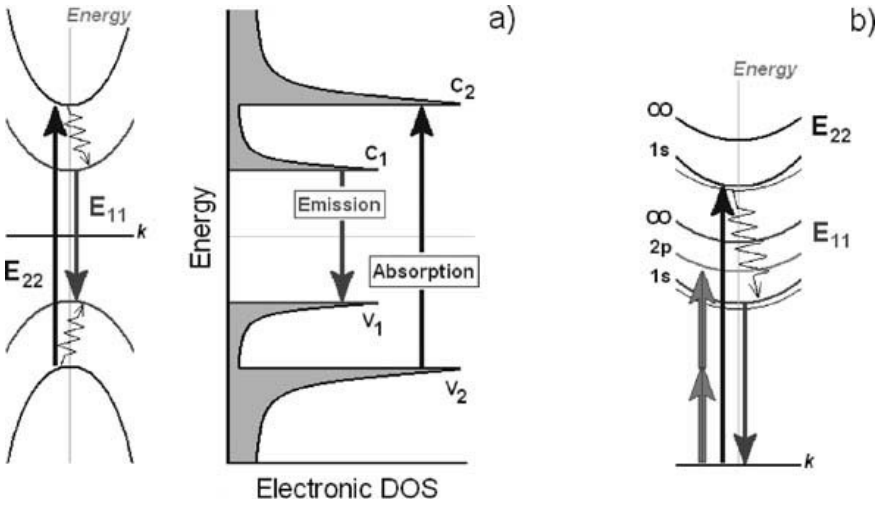

Figure 2.3.5: Optical processes in SWCNTs. a) The band structure and optical transitions in a simplified single-particle picture and its corresponding density of states. Upward-pointing arrows represent E_{22} light absorption, while downward-pointing arrow refer to E_{11} light emission. The thin jagged arrows illustrate non radiative relaxation from E_{22} to E_{11}. b) Simplified picture of the exciton band structure and optical transition. As in the other picture one-photon processes are shown, but in addition a two-photon process is represented with two gray upward-pointing arrows. The ground state represents a vacuum state, that is, with no excitons . Taken from [69].

[69].

Surprisingly one-electron band theory models, which neglect excitonic effects, have been fairly successful in describing overall trends and providing a comparative and even semi-quantitative picture of transition energies for a variety of single-walled carbon nanotubes. This success depends from the approximate cancellation of two large but opposing many-body effects: electronic self-energy and exciton binding energy. Moreover, the van Hove-dominated interband optical transitions expected from a band theory model, including excitonic effects, are transformed into a single dominant transition for each matching pair of sub-bands in a given nanotube species. Thus, the use of E_{ii} labels to classify optical transitions and the simple correspondences between species and transition wavelengths remain valid in excitonic treatments of nanotube spectroscopy [66].

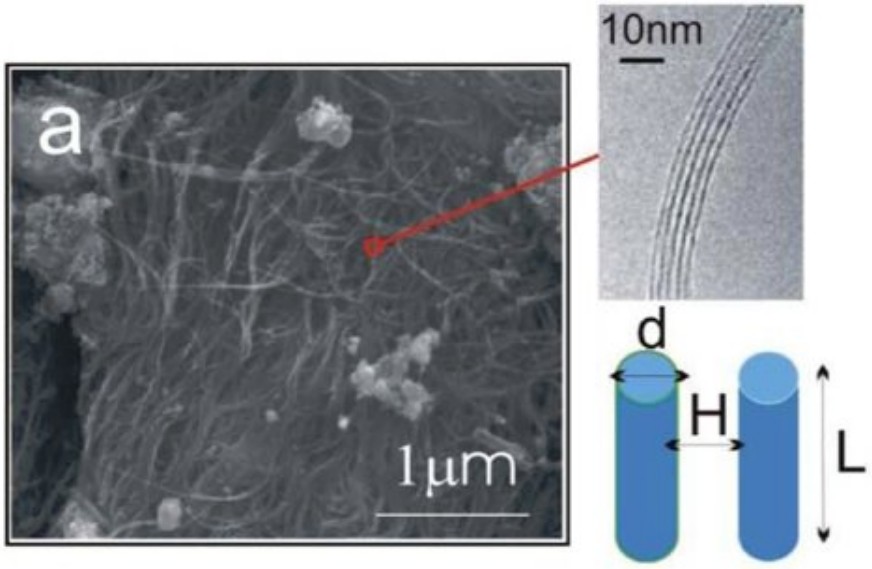

Figure 2.3.6: Scanning electron micrographs showing SWNTS, with inset showing a bundle of closely-packed single-walled nanotubes. Taken from[74]

2.3.3 SWCNTs absorption and emission spectra

A raw sample of nanotubes is characterized by an ensemble of tubes species, having different chiralities, which are aggregated into bundles held together by van der Waals forces. The CNTs optical properties are affected by the bundling of tubes because this bundling perturbs the electronic structure of the tube. An optical property that is greatly reduced by this effect is the luminescence efficiency, which results in a virtual absence of near-IR emission. It seems likely that this effect arises from rapid transfer processes from semiconducting to metallic tubes within the bundle. By statistical considerations, approximately one-third of the nanotubes in a raw sample are expected to be metallic. Consequently, there is a high probability that one or more metallic tubes will be included in randomly formed bundles containing at least several nanotubes. When a bundled semiconducting SWCNT absorbs light, electronic coupling with its neighbors causes rapid excitation energy transfer to species with smaller band gaps and eventually to a metallic nanotube, in which the excitation have to relax non-radiatively [66]. Nanotubes aggregation is particularly problematic because, even if detached from bundles by physical means, the highly polarizable, smooth-sided fullerene tubes will readily return to form parallel bundles or ropes via van der Waals interaction, therefore a procedure that applies a nonperturbing coating to prevent re-aggregation is needed.

A solution to this problem was firstly achieved with the preparation of isolated nanotubes where SWCNT raw sample were firstly debundled by means of ultrasonication and dispersion in aqueous sodium dodecyl sulfate (SDS) sur-

factant. In this fashion SWCNTs are coated by micelles in a non-perturbing way, preventing the re-bundling via repulsive Coulomb interaction[15]. Successively exploiting the different density and weight of single and bundled tubes to remove from the solution any remaining bundles, the sample was centrifugated and the upper 75-80% of supernatant decanted [45].

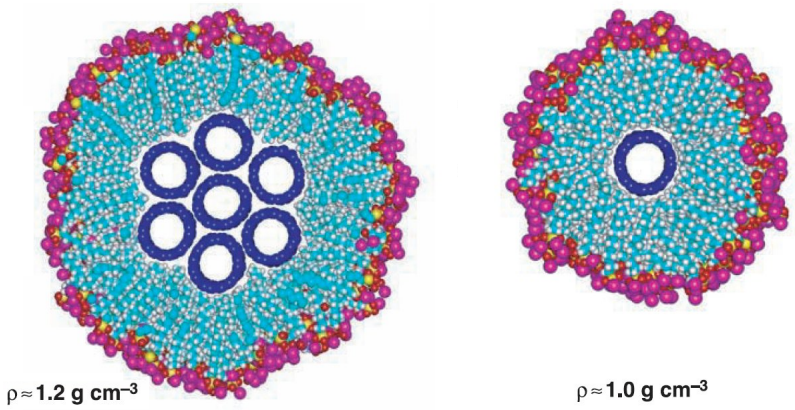

Figure 2.3.7: Cross-section model of an individual fullerene nanotube in a cylindrical SDS micelle and a seven-tube bundle of fullerene nanotubes coated by a layer of SDS. The approximate density of these species is 1.0 and 1.2 $g\,cm^{-3}$, respectively. Taken from [45].

In one electron model, whose predictions do not deviate too much from the exciton model, the absorption and emission spectra of a single (n_1, n_2) SWCNT species are expected to consist mainly of a series of sharp features at energies E_{ii}, where i takes the value $i = 1, 2, 3, \ldots$ according to sub-band, because these transitions are predicted to be most intense when the quanta of light matches the energy difference between corresponding van Hove singularities. Considering nanotubes having diameter near 1nm, the first three of these transition will appear in the near-infrared, visible and ultra-violet regions for semiconducting tubes. While metallic or semi-metallic SWCNTs of similar diameter their lowest energy optical transitions will have visible wavelengths, which falls between E_{22} and E_{33} semiconducting nanotubes peaks [66].

[15]Recalling that surfactant can be structurally described as formed by a hydrophilic head and an hidrophobic tail, opportunely chosen, surfactants contain electrically charged functional groups at their head (ionic surfactants), which render the micelles charged objects that repel each others.

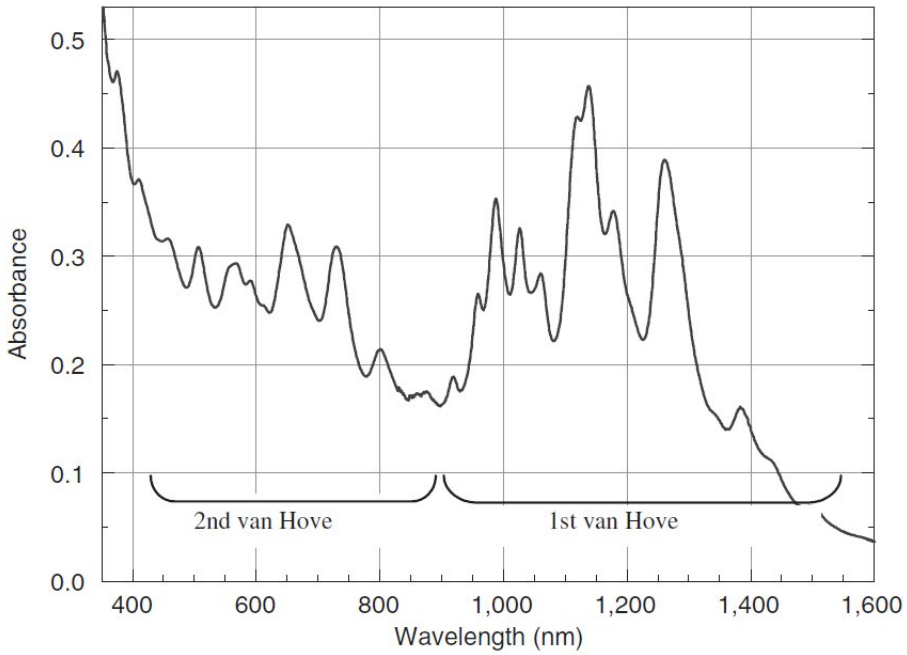

Figure 2.3.8: Optical absorption spectrum of a sample of SWCNT suspended in D_2O by SDS surfactant at 276 K. Taken from [66].

AS can be seen in figure 2.3.9, aqueous samples enriched in individual surfactant-suspended SWCNTs, whose preparation has been described previously, showed sharp fluorescence peaks in the near-infrared emitted only by semiconducting tubes. The data show that the sample contains an ensemble of different emitting species, each displaying one dominant transition in this spectral range and a very small stokes shift between its absorption and emission spectra as well as similar line widths. Therefore the same states are responsible for both processes and fluorescence involves transitions between band extrema in semiconductors (i.e., only from for E_{11}^S transitions and not for E_{22}^S or higher transitions, where "S" means "semiconducting") [69]. The many spectral features in this region correspond to different (n_1, n_2) species of semiconducting single-walled nanotubes in the structurally heterogeneous sample [66]. The micelle-encapsulated emission peaks are slightly red-shifted, which is explainable by a dielectric screening effect produced by the solution surrounding the nanotubes [69].

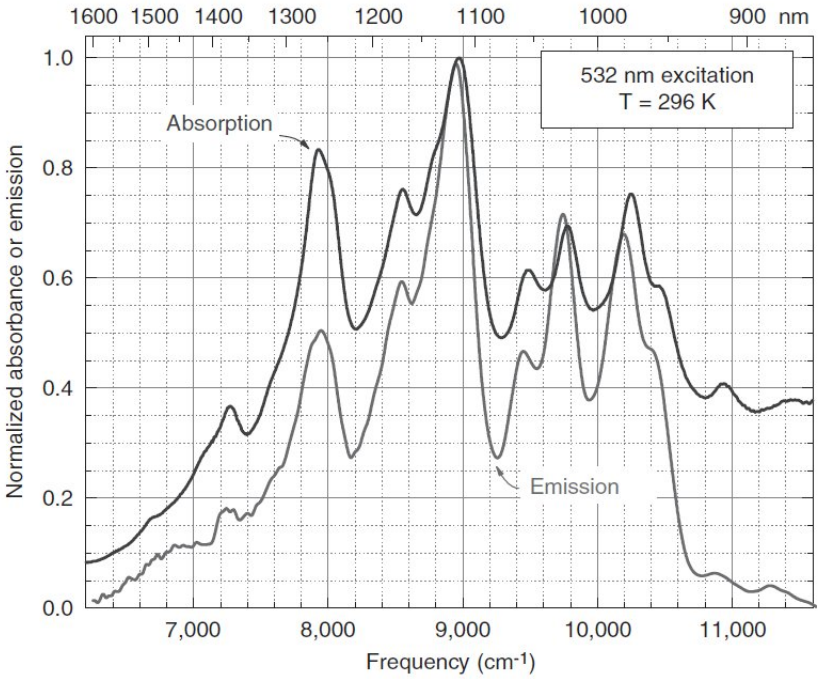

Figure 2.3.9: Absorption and emission spectrum in first van Hove band gap transitions region of individual nanotubes suspended in SDS micelles in D_2O excited by 8 ns, 532-nm laser pulses.

The observed structure near-infrared emission have been identified as fluorescent band gap transitions from a variety of semiconducting SWCNT species contained in bulk samples, but the problem is that from absorption and emission measurements alone it is not possible to assign which absorption peak corresponds to two transition of the same tube. The assignment to identify the nanotube species present in a sample has been obtained by measuring the fluorescence as a function of the energy of the excitation light, and goes under the name of photoluminescence excitation spectroscopy (PLE). Thanks to the fact that SWNTs have a peculiar, species-dependent (or equivalently, chiral-dependent) optical absorption spectrum, changing the excitation wavelength, a maximum in intensity is found whenever the excitation energy meets an absorption resonance from which relaxation to a fluorescence-emitting transition occurs. In this fashion a three-dimensional "map" showing photoluminescence intensity vs. emission and excitation wavelengths have been obtained. An example of a PLE map is shown in figure 2.3.10 , where the emission intensity is plotted on a grey scale, with the excitation wavelength along the x-axis and the emission wavelength along the y-axis.

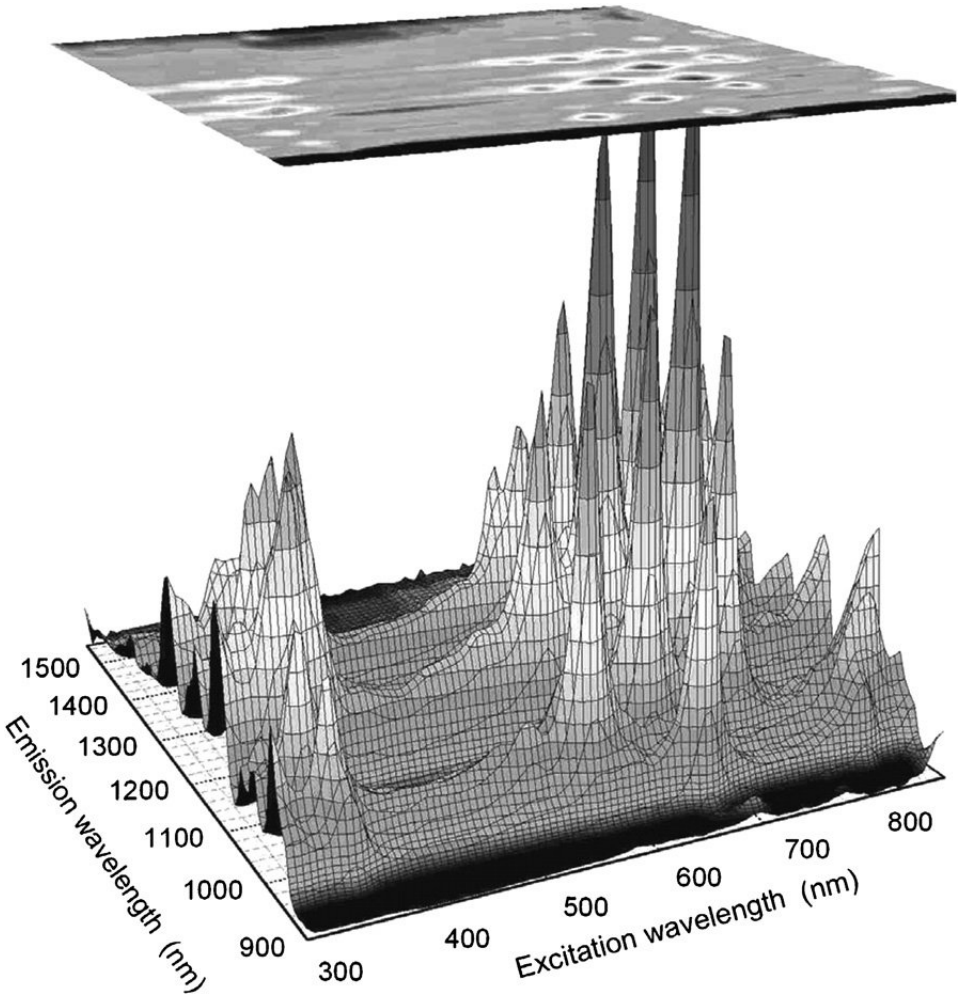

Figure 2.3.10: Surface plot showing the emission intensity, as a function of the excitation and emission wavelengths, from a sample of SWCNT in SDS/D_20. Each distinct peak arises from a specific(n_1, n_2) species of semiconducting nanotube. Taken from [66].

The so-called "fingerprint region" is visible in the right part of the plot, where Each distinct peak arises from resonant absorption into E_{22}^S with emission at E_{11}^S, for a specific (n_1, n_2) species of semiconducting nanotube [9, 66, 69].

2.3.4 Fluorescence fading in aqueous SWCNTs suspension

Previous studies conducted by the researchers of the Laboratory for Radiopharmaceutical and Molecular Imaging (LARIM) in National LAboratories of Legnaro (LNL), have demonstrated a strange fading behavour of the near-infrared

fluorescence emitted by SWCNTs, excited NIR laser light.

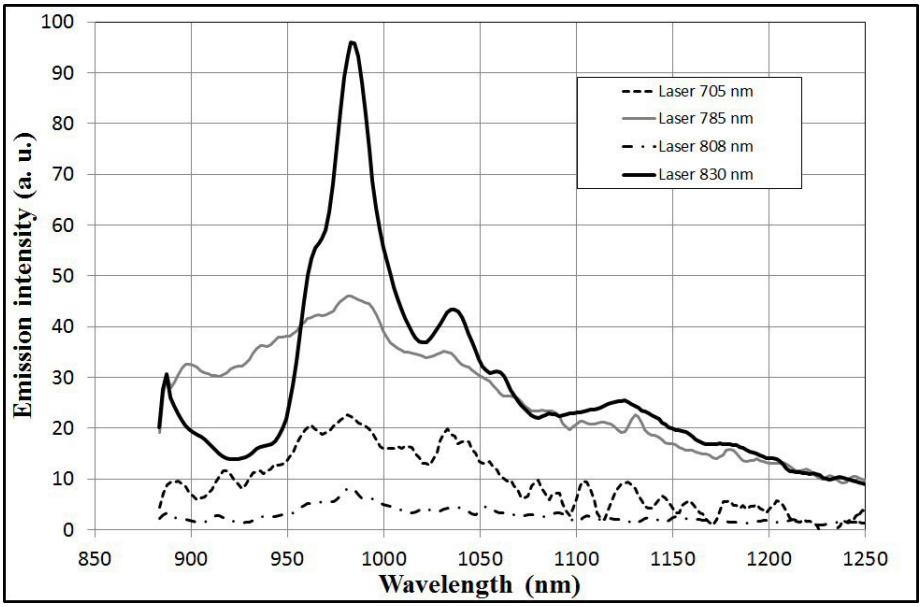

Figure 2.3.11: Photoluminescence emission of SWCNTs in a sodium cholate aqueous solution for four different wavelengths: 705 nm; 785 nm; 808 nm; 830nm. Taken from [73]

Sodium cholate aqueous Comocat SWCNTs were firstly used to study the photoluminescence emission respect to the excitation wavelength. NIR spectra of the observed photoluminescence from the surface layer of the solution are shown in figure 2.3.11. The laser beam with a wavelength of 830 nm revealed highest photoluminescence yield with well pronounced peaks at 983 nm (chiral vector (6,5)) and 1033 nm (7,5) and a weaker one at 964 nm (8,3).

A study of the aqueous sodium cholate SWCNTs ablility to maintain certain photoluminescence intensity as function of the storage time had been conducted in a period of time up to 8 hours, with an excitation wavelength of 830nm. Between the measurements the cuvette with the solution was kept in a dark storage at a temperature of 20 °C. The measured total photoluminescence intensity with respect to the storage time is shown in figure 2.3.12.

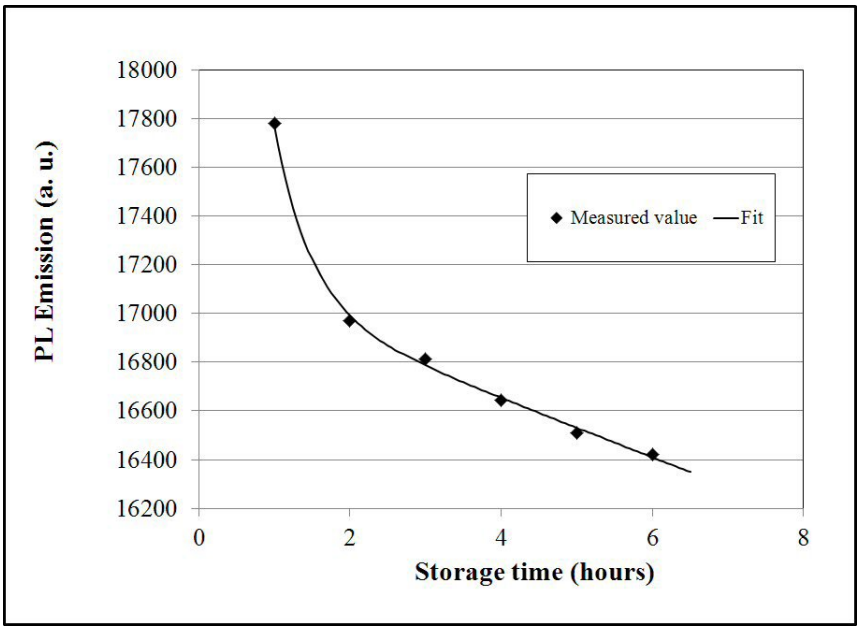

Figure 2.3.12: Photoluminescence emission of SWCNTs in a sodium cholate aqueous solution versus the storage time. taken from [73].

The fading of the photoluminescence observed in figure was most probably due to some processes of re-aggregation of the SWCNTs in the solution [74] . A simple model was applied to the experimental data demonstrating that it can be considered as two-component process (the fitted curve in figure 2.3.12) with halftimes of 20 minutes and 94 hours. The change in the photoluminescence however is relatively low and would not exceed 20% from the initial value for a measuring period of 24 hours. Fluorescence appears to be the optical property of nanotubes that is most sensitive to sample condition, such as environment chemical and physical conditions [66, 69]. By these considerations, in the LARIM reaserch group has been designed and realized a long-time temperature-controlled storage system for micelle-suspended SWCNT solutions for the study of the fluorescence fading as function of the storage temperature and time. In the following chapter will be presented the experimental apparatus, while presentation and the discussion of the results obtained will be discussed in chapter 4.

Chapter 3

Experimental setup

3.1 General description

To characterize the SWCNT fluorescence fading, it was necessary the implementation of a system able to maintain the sample in a condition of constant temperature (thermostatic chamber) for all the period of measure (two weeks), which at the same time was able to register and monitor the environmental conditions such as humidity and laboratory room temperature in order to guarantee no condense formation on the cuvette side walls . The principal system components are:

- an excitation NIR laser light source (laser diode THORLABS M9-830-0150), with maximum output power of 150 mW,
- a NIR spectrometer for the measure of SWCNT fluorescence spectra (Hamamatsu mini-spectrometer TG series C9406GC) and relative optical fiber light input (type n. A9763-01),
- a power meter for the measure of the laser beam intensity (THORLABS PM100USB with photodiode power sensor S142C),
- a long-term constant-temperature conditioning system for a thermostatic chamber,
- a computer for the data recording and software management.

The system has been installed directly on a optical bench, keeping all the elements as close as possible in order to realize a relative compact acquisition system. A single computer operates several of these elements and the data acquisition. For this purpose, the NIR spectrometer and power meter management software have been installed on a computer with windows xp as operating system. Furthermore a single software was implemented for the running of the thermostatic chamber and the acquisition of the humidity and room temperature data. For the laser source power supply and diode laser temperature control

their relative modules have been used (THORLABS LDC 205C POWER SUPPLY and THORLABS TED220C respectively). The whole system has been designed to be easily modified, and eventually integrated with new components, in order to respond to all necessities that can arise during the research. The whole system is schematically reported in figure 3.1.1.

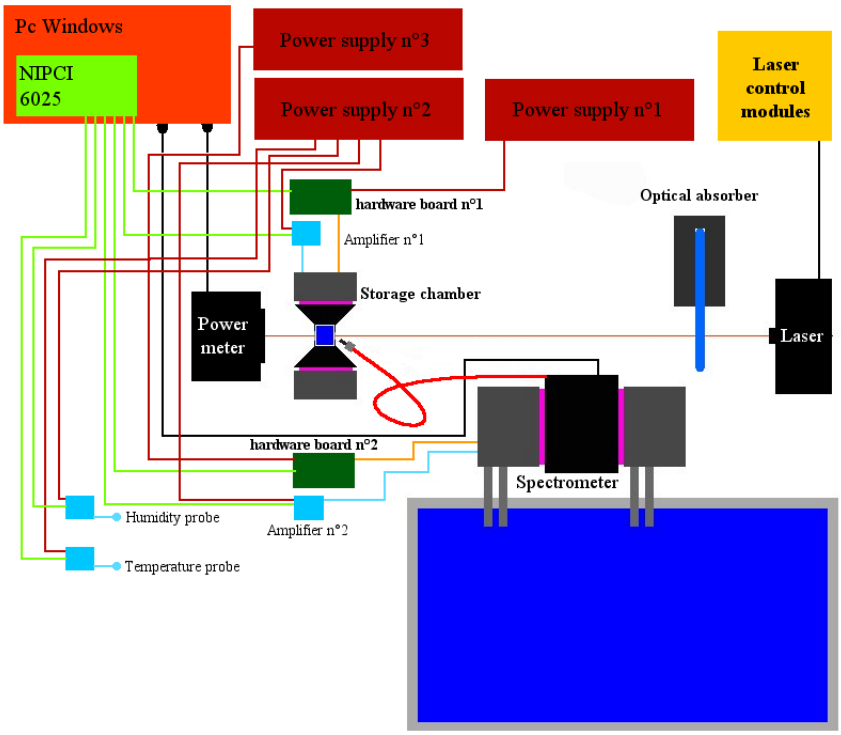

Figure 3.1.1: Scheme of the last version apparatus component displacement: In the upper part are shown the computer, the three power supply for the electronic elements that characterize the conditioning temperature system, the LDC and TED modules for the laser source. All these components haven't been positioned on the optical bank, as well as the water container (visible in the lower right part of the figure) used for the spectrometer cooling system. All the other optic and electronic elements have been mounted on the optical bank to keep the system as compact as possible.

3.2 NIR spectrometric tract

As can be seen in the figure 3.1.1, the trajectory of the laser beam goes trough an optical filter (Newport circular variable metallic ND filter 50G02AV, mounted on Newport ND filter rotator model 946) to reduce the beam optical power to

Table 3.1: Laser diode M9-830-0150 specifications, taken from the laser diode data sheet available on reference [75].

Specification	Symbol	Min	Typ	Max
Wawelength, nm	λ_p	825	830	835
Spectrum, nm FWHM		-	0.5	2
Output Power, mW	P_o	-	150	-
Operation Current, mA	I_{op}	-	170	220
Operating Voltage, V	V_{op}	-	1.9	2.2
Vertical Far Field, FWHM	deg	13	18	23
Parallel Far Field, FWHM	deg	-	8	10
Slope Efficiency, mW/mA	η	0.9	1.0	-

a desired value. After the optical attenuator disk, the beam cross the storage chamber where the cuvette containing the sample solution is located during the measurements. Finally the beam reach the power meter, which constitutes the stopping point of the beam line and it is functional for the laser beam optical power calibration that has to be made before every measure. In front of the input hole of the sample storage chamber there is the optical fiber input connector (in figure 3.1.1 the optical fiber is schematically drawn as the red cable connected with the spectrometer) whose orientation direction forms an angle of about 30° respect to the laser beam line. The optical fiber connector has been placed sufficiently close to the input hole of the storage chamber in order to satisfy the conditions requested by the constructor about the optimal setup for the NA (numerical aperture).

3.2.1 Laser beam characterization

To characterize the fluorescence emission of SWCNTs it is necessary to implement a system capable of generating a laser light with the correct wavelength using a laser diode. In the setup a THORLABS laser diode M9-830-0150 emitting at 830nm has been implemented, its specifications are reported in Table 3.1.

The so called *"knife edge" technique* has been applied in order to obtain an estimation of the parameters that characterize the laser beam, such as the *beam waist* W_m , the *Rayleigh range* z_m and the *angular divergence* $2\theta_m$. This method consists in recording the beam total power while an opaque knife is gradually translated across the laser beam. The knife has to be initially positioned in a way that guarantee that all the beam can reach the power meter. Successively it is moved across the beam, step by step using a calibrated translation stage, causing a partial beam screening effect. The knife is moved up to the moment when all the beam is stopped. In figure 3.2.1 are shown the data obtained for one of these measures.

All the measures collected in this fashion are used to evaluate the beam radius $W(z)$ at the position z at which the knife is located respect to the laser

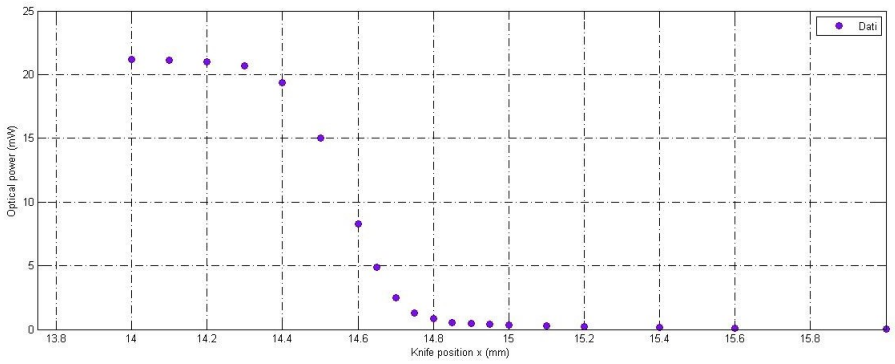

Figure 3.2.1: Example of knife edge measure data: Data obtained at the position $z = 28$ cm, where z express the distance of the knife from the laser.

source. By convention z is the direction of propagation of the laser beam, while the orthogonal direction along the optical bank is indicated by x. The relationships that permit to obtain the beam radius at each z position are:

$$\frac{dI}{dx} = \frac{I(x_{i+1}) - I(x_i)}{x_{i+1} - x_i}, \tag{3.2.1}$$

where I is the optical power and dI/dx is a Gaussian function:

$$\frac{dI}{dx} = \frac{P_{tot}}{W(z)\sqrt{\pi}} e^{\left(-(x-x_0)^2/W^2(z)\right)}. \tag{3.2.2}$$

This method has been used for the evaluation of $W(z)$ at four different z positions, the results are reported in Table 3.2 .

Table 3.2: $W(z)$ values obtained at four different z positions (σ_z and σ_W are the uncertainties of z and W respectively).

z (cm)	σ_z (cm)	$W(z)$ (mm)	σ_W (mm)
23.60	0.05	0.17	0.01
28.00	0.05	0.14	0.01
32.20	0.05	0.23	0.01
36.60	0.05	0.35	0.03

Once obtained these values for the beam radius, another fit has been conducted to obtain the laser beam parameters, using the relation

$$W(z) = W_m \sqrt{1 + \left(\frac{z - \widetilde{z}}{z_m}\right)^2}, \tag{3.2.3}$$

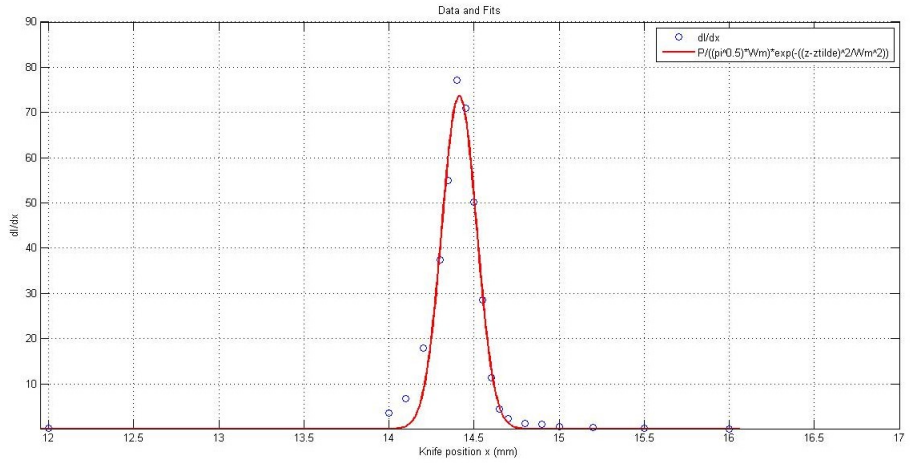

Figure 3.2.2: Waist radius evaluation: Data obtained applying the equation 3.2.1 and the fit based on equation 3.2.2.

where W_m is the beam waist, z_m[1] is the Rayleigh range and $\widetilde{z}$ is the position at which $W(\widetilde{z}) = W_m$.

The values of the parameters of the fit made with equation 3.2.3 are listed in Table 3.3.

Table 3.3: Laser beam characteristic parameters

W_m (mm)	σ_{W_m} (mm)	z_m (cm)	σ_{z_m} (cm)	$\widetilde{z}$ (cm)	$\sigma_{\widetilde{z}}$ (cm)
0.14	0.01	4.2	0.1	26.6	0.3

Exploiting these results it has been possible to calculate the $M^2 - factor$, that yields a measure of the optical beam quality by giving the deviation of its profile from Gaussian form, where the Gaussian beam represent the ideal case. The $M^2 - factor$ can be evaluated using the relation

$$M^2 = \frac{2W_m 2\theta_m}{4\lambda/\pi}, \tag{3.2.4}$$

where $2W_m$ is the beam diameter, $2\theta_m$ is the angular divergence and $4\lambda/\pi$ is the result of the product of these two terms in the ideal case (λ is the laser wavelength). It is possible to calculate the angular deviation of the beam from

$$\theta_m = \frac{W_m}{z_m}, \tag{3.2.5}$$

[1] By definition $\widetilde{z} \pm z_m$ are the z values at which the beam radius is increased by a factor $\sqrt{2}$, therefore $W(z \pm z_m) = \sqrt{2}W_m$ [76].

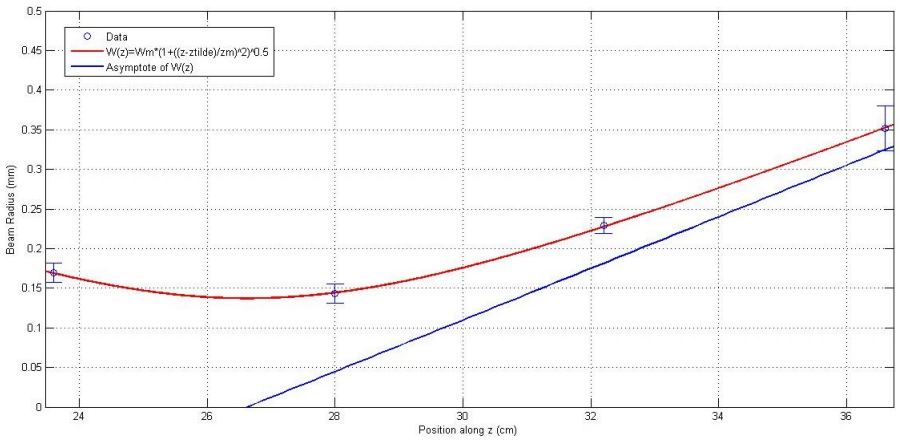

Figure 3.2.3: Fit of the beam radius function *W(z)*: Blue circles with relative error bars refer to the beam radius obtained at each z. The red line is the fit performed on custom equation based on relation 3.2.3. The blue line is the asymptote of $W(\Delta z)$, which goes as $W(\Delta z) \approx \theta_m \Delta z$ where $\Delta z = z - \widetilde{z}$, and θ_m is the angular semi-divergence of the beam.

Table 3.4: Optical characteristics of Hamamatsu mini-spectrometer TG series C9406GC, taken from [77].

Parameter	Specification	Unit
Spectral response ranges	900 to 1700	nm
Spectral resolution (FWHM)[2]	7 max.	nm
Wavelength reproducibility[3]	-0.2 to +0.2	nm
Wavelength temperature dependence	-0.04 to +0.04	nm/°C
Spectral stray light[4]	-33 max.	dB

where the beam angular semi-divergence θ_m is the slope of the line that describes the asymptotic behavior of the waist radius, as can be seen in figure 3.2.3. It has been obtained $\theta_m = (3.3 \pm 0.2)$ mrad. Inserting the found results in equation 3.2.4 with a laser wavelength $\lambda = 830$ nm, one obtains $M^2 = 1.7 \pm 0.1$. The value of M^2 obtained is in accord with the typical values obtainable with collimated TEM_{00} laser-diode beams ($M^2 \approx 1.1 - 1.7$) [76].

3.2.2 Spectrometer

Measurements of the fluorescence spectrum of the SWCNT are carried out very close to the cuvette surface using Hamamatsu mini-spectrometer C9406GC. In Table3.4 are reported some specification of the mini-spectrometer.

SWCNT fluorescence emission light to be measured is collected and guided

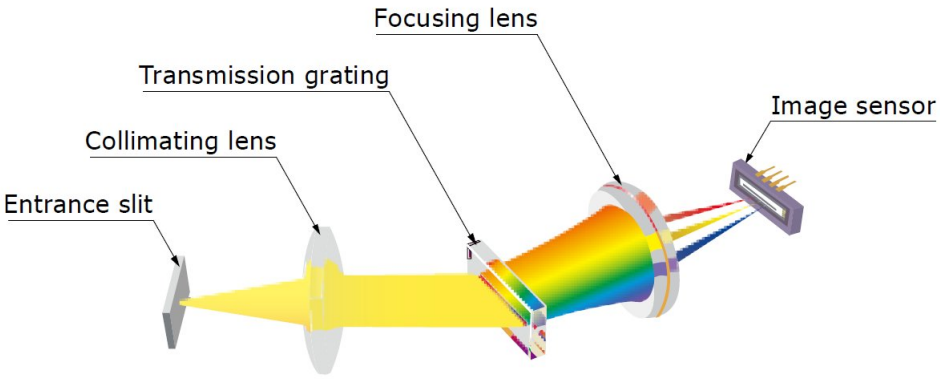

Figure 3.2.4: Optical component layout of the Hamamatsu mini-spectrometer TG series C9406GC. Taken from [77].

Table 3.5: InGaAs image linear sensor G9204-512D. Taken from [79].

Parameter	Specification	Units
Cooling	Non-cooled	-
Image size	12.8 x 0.5	mm
Number of total pixels	512	pixels
Number of effective pixels	512	pixels
Pixel Size (H x V)	25 x 500	μm
Pixel pitch	25	μm
Window material	Borosilicate glass with anti-reflective coating	-

through an optical fiber (type no. A9763-01) into the entrance slit of the mini-spectrometer. In figure 3.2.4, the mini-spectrometer optical layout is graphically shown. Since light passing through the *entrance slit* spreads at a certain angle, a *collimating lens* (*or mirror*) collimates this slit-transmitted light and guides it onto a *transmission grating*. The grating separates the incident light into different wavelengths and lets the light at each wavelength pass through (or reflect away) at a different diffraction angle. The *focusing lens* (or *mirror*) forms an image of the diffracted light onto the linearly arranged pixels of the *image sensor* (InGaAs image linear sensor G9204-512D) according to wavelength [77, 78].

The image sensor converts the optical signals into electrical signals and then outputs them from the USB port to a PC for data acquisition. Table 3.5 reports some specification of the InGaAs image linear sensor G9204-512D, while in figure 3.2.5 is shown its spectral response.

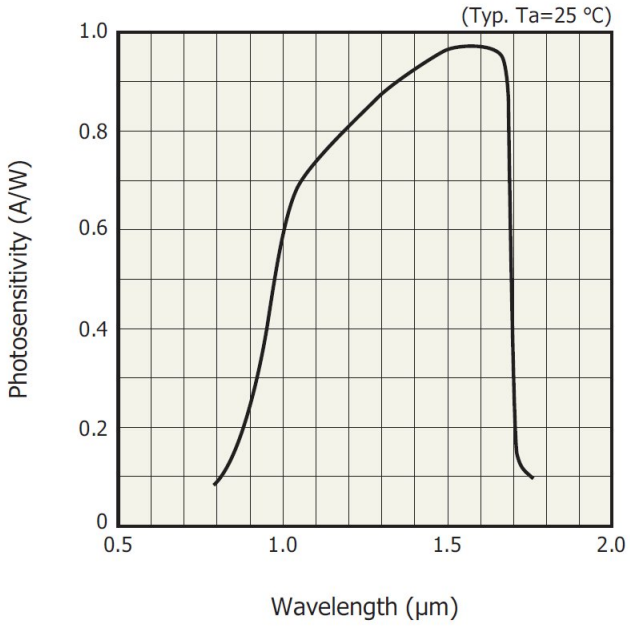

Figure 3.2.5: Spectral response of InGaAs image linear sensor G9204-512D. Taken from [79].

3.3 Setup for long-time constant-temperature sample storage

The long-term constant-temperature storage compartment for solutions with NIR emitting nanoparticle has been gradually designed, constructed and tested in the Laboratory for Radiopharmaceutical and Molecular Imaging (LARIM) in the National Laboratories of Legnaro (LNL). In this section a short presentation of the main system components and the system evolution is presented.

In its first version, a control system capable of manage the storage chamber temperature from the room temperature down to 5°C has been realized. Through an opportune electronics, a PID algorithm implemented via software manages the current of two Peltier cells installed on the external surface of the thermostatic storage chamber.

3.3.1 Systems controlled by PID algorithm

A *control system* is every physical system which establish a relation of correspondence, under a certain law , between an input quantity , called *target* or *set*, and an output quantity , which is the one that is under control.

It is possible to distinguish, from a structural point of view, two principal types of systems: *open-loop* systems and *closed-loop* (or feedback) system. In

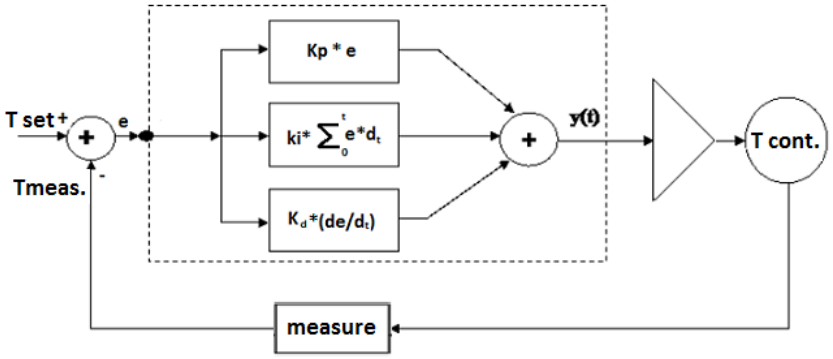

Figure 3.3.1: Example of block diagram scheme of a PID algorithm for temperature control

open-loop systems the control is given only by means of an external action which is not able to correct any disturb or possible variation of the output quantity. On the contrary in feedback systems the control is given, besides the external action, even from an internal action (feedback) which is based automatically on the measure of the output quantity.

The PID (Proportional Integral Derivative) algorithm is part of the feedback systems. It is based on the elaboration of the error given by the difference of the reference value (set value) from the output value (controlled value). To implement this algorithm is sufficient to calculate three contributions (Proportional, Integral and Derivative) and sum them together in order to obtain the value of the variable to send at the control which will act on the output quantity.

Figure 3.3.1 illustrated an example of block diagram scheme for a PID algorithm. The k_p, k_i and k_d are respectively the proportional, integrative and derivative constants which characterize the amplification factor (or weight) of each contribution. T_{set} is the target temperature, T_{cont} represent the controlled temperature (output), T_{meas} is the measured temperature, e the error and y(t) is the variable which acts on the control at the output. The integral is considered for all the time of the control process. Usually in a PID implemented with digital systems (discrete systems), minimum and maximum limits are imposed both for the output values that comes out from the three elaborations and for the total sum y(t). This choice is taken in order to not fall in particular conditions in which the variables assumes values either out of the permitted limits of the digital variable itself or out of the range permitted by the output controller. In this fashion all the cases where it would be impossible to predict the system behavior are prevented.

Taking in consideration a digital PID, a complete elaboration cycle [5] have

[5] With a complete elaboration cycle is meant the execution of all the operation that allows

to be done in a sufficient short time and with a constant frequency. For what concern the temperature control case, the time cycle can be relatively slow because the variation of the variable that are controlled are themselves quite slow, while the elaboration frequency has to be precise anyway.

The system that has been used for the measurements presented in this thesis has an elaboration time cycle of 100ms, short enough to guarantee a quick response to the temperature variation. In the LabVIEW control software a complete PID algorithm has been implemented, however it has been decided to control the temperature only exploiting the proportional and integral parts, excluding the derivative one, setting $k_d = 0$. This choice is justified because the derivative part is usually used when fast variables are present, but as said before, here all the variable of interest are quite slow. The constants k_p and k_i have been set empirically after that some appropriated tests have been made by varying the constants one by one. As an example, subsequently it is reported the practical procedure that has been followed to find the PID coefficients value in the cooling modality of the system. In practice, a set temperature equal to 10% of the maximum range has been set[6], $T_{set\,cooling} = 23°C$. Then the $k_{p,cooling}$ coefficient has been set equal to 1, keeping the $k_{i,cooling}$ and $k_{d,cooling}$ equal to zero. With this PID parameters setting the cooling system has been tested in order to see if it were able to reach the $T_{set\,cooling}$ temperature after a period of time of ten minutes. With this choice the difference between the desired and the instant temperature (*i.e.,* the error e) was considerable, therefore the $k_{p,cooling}$ coefficient has been incremented by steps of 0.2, executing, for every $k_{p,cooling}$ value, a run test to verify the system behavior. This procedure has been repeated up to the moment when consistent phenomena of instability (oscillations respect to the set point) were visible in the initial phase of the instant temperature trend in its approaching of the set temperature value, as it can be seen in figure3.3.2 for the light-blue dashed line. For our system these instability phenomena started for $k_{p,cooling} = 2.2$. the final value was obtained by decrementing the previous value by a 10%, giving $k_{p,cooling} = 2.0$.

In an analogous fashion, keeping fixed $k_{p,cooling} = 2.0$ and $k_{d,cooling} = 0$, the $k_{i,cooling}$ has been calibrated by means of the same procedure starting from an initial value of 0.5. But the instability was already present since the first test, suggesting that $k_{i,cooling}$ should be decremented instead. Proceeding with values

---

the calculation of the output response: the measure of the controlled variable, the error calculation, the elaboration of the three component (proportional, integral and derivative) and the generation of the output response.

[6]The system always starts from the room temperature which represent the zero of the system. Therefore the maximum (or minimum) temperature that the system can reach is always referred to this starting point. To set up the T_{set} for the calibration of the PID parameters the following practical procedure has been used. Firstly the system maximum range was fixed, where a minimum temperature of 5°C was chosen. Therefore the system maximum rage was $r_{max} = |T_{room} - T_{min}| = 20°C$ with a $T_{room} = 25°C$. Then the set temperature used for the calibration of the PID coefficients was obtained by subtracting from the starting point a value equal to the 10% of the r_{max}. $T_{set\,cooling} = (25 - 0.1 \cdot r_{max})°C = 23°C$. Analogously it has been made for the calibration of the PID parameters in the heating mode, in this case the maximum range was $r_{max} = |T_{room} - T_{max}| = 20°C$ with a maximum temperature of 45°C. Therefore a $T_{set\,heating} = (25 + 0.1 \cdot r_{max})°C = 27°C$ was obtained.

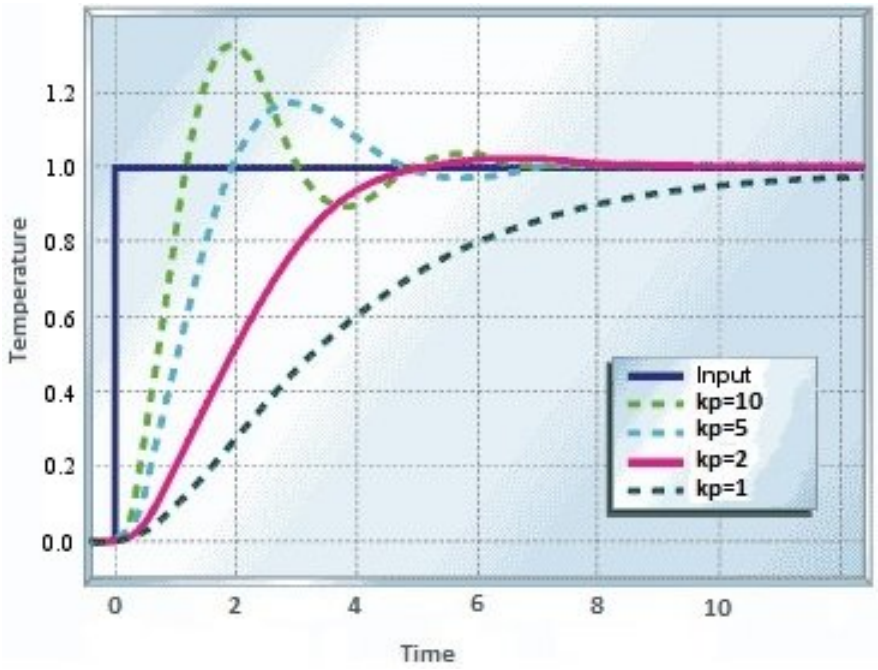

Figure 3.3.2: Graphically representation of the variable T_{meas} as a function of the time. The T_{set} is shown with the violet continuous line, while trend of T_{meas} as a time function is displayed for several values of the k_p coefficient. For values of k_p greater than 2 the instability behavior can been noted.

every time smaller, a very lightly instability was found at $k_{i,cooling} = 0.0022$. From this value, the final coefficient was obtained by keeping a 10% smaller value from the previous one, giving $k_{i,cooling} = 0.002$.

This procedure has been made a first time for the cooling modality, and then another time for the heating modality, which has been inserted successively (see final part of Appendix B). At the end of the calibration procedure, the PID coefficients found for the cooling modality were $k_{p,cooling} = 2$ and $k_{i,cooling} = 0.002$, while for the heating $k_{p,heating} = 0.5$ and $k_{i,heating} = 0.0001$ have been obtained. As previously described k_d is equal to zero in both cases.

3.3.2 Description of the system constituent element

The system was initially composed by the following elements:

- A computer on which runs a software written in LabVIEW environment (version LabVIEW 8.2 by National Instrument).
- A PCI6025E board by National Instruments, mounted on the pc, which communicates with the hardware board and the temperature sensor.

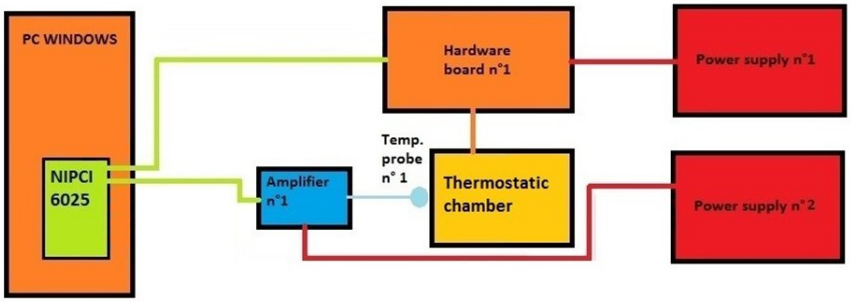

Figure 3.3.3: Functional block diagram scheme of the system in its initial version. The red lines represent the power supply wires. The azure line is the probe signal. The light green lines are amplified signals, one for the hardware board control and another for temperature sensor. The orange wire linking the hardware board with the thermostatic chamber represents the current signals for the Peltier cells.

- A hardware board, constructed in the LARIM laboratory, assembled on a single copper hole veroboard. The hardware board is composed by a microcontroller PIC16F876A by Microchip (inside of which there is a PWM module, see Appendix A), a MOSFET IRLI3705N by International Ior Rectifier capable of switching the current into Peltier cells and a driver TC4469 by Microchip.
- A temperature sensor LM35 by TEXAS INSTRUMENT with related signal amplifier.
- Two power supplies TTi EL302RT, which are used to power the hardware board and the temperature probe amplifier.
- A thermostatic chamber realized in aluminum , insulated with a polystyrene case 1cm thick, and provided with two Peltier cells (ET-127-14-15 by Global Component Sourcing) together with their relative heat sinks and fans.

With this version of the system several preventive measurements have been conducted to control the thermostatic system. For example several tests have been made to verify its ability and rapidity in reaching the goal temperature, as well as to monitor its stability and to quantify an eventual discrepancy between the temperature of the storage chamber and the solution sample. In this last case on the system was integrated another temperature probe (LM35) with a electronics identical to the other temperature probe, but with the sensor inserted into a small thin copper cylinder used to insert the probe in a aqueous solution sample.

Reaching temperature as low as 5°C, some times has been observed the formation of condensed water on the cuvette walls. In order to prevent the risque of condense formation, the system was further modified inserting a humidity sensor and keeping the humidity inside the lab as low as possible by means of dehumidifier. In this configuration the system had two sensors monitoring the lab environment (humidity and temperature). Combining these two informations and exploiting the psychrometric chart, it was possible to operate in a range of temperature without condensation problems.

With this system configuration, fluorescence emission measurements of aqueous solutions enriched in individual surfactant-suspended SWCNTs have been conducted at three different temperatures (10°C, 15°C and 20°C). For each temperature two different types of SWCNT solutions have been prepared: one having tubes with chirality (6.5) (SG65 by Sigma-Aldrich) and another with chirality (7.6) (SG76 by Sigma-Aldrich). For all the solution preparations, Sodium cholate hydrate (Sigma_Aldrich C6445-10G) has been employed as surfactant to produce aqueous SWCNT-micelle suspended. The details of the nanotube preparation procedure will be described in the successive chapter.

The subsequent data analysis has shown a strange and unexpected behavior, severely different from that observed in previous LARIM group research [73]. This behavior was imputed to a room temperature dependence of the fluorescence emission data. Successive investigations have suggested that a possible explanation could be found in the spectrometer response, because the spectrometer model employed was not temperature controlled. Following this hypotheses, a thermostatic system similar to that of the storage chamber has been constructed and implemented. In the successive measurements the results were more stable than previous one, but there were still some data strangely departed from their expected behavior, implying that not all the issues were solved. Finally a general review of the system evidenced a problem with the setting of the TED laser module, which was not fully operative during the entire period of data acquisition, leaving the diode temperature essentially equal to the room temperature and therefore free to fluctuate with it. The TED module was finally set providing a full time control of the diode laser temperature, which was selected equal to 25°C. Three final set of measurements were finally obtained with the system in its last configuration, showing a good data behavior if compared with the previous results conducted by the LARIM research team. Figure 3.3.4 shows the full functional block diagram system employed for the final measurements conducted, whose results will be discussed in the successive chapter.

3.3.3 The control software

All the system is controlled by a software written in LAbVIEW 8.2, which allows to read the humidity and the three temperature sensors by a 12 bit ADC (present inside the NIPCI6025 board), drive the hardware circuits by 12 bit DAC output channels, operate two PID temperature controllers, save the temperature and humidity data acquired as function of the time in excel format and graph

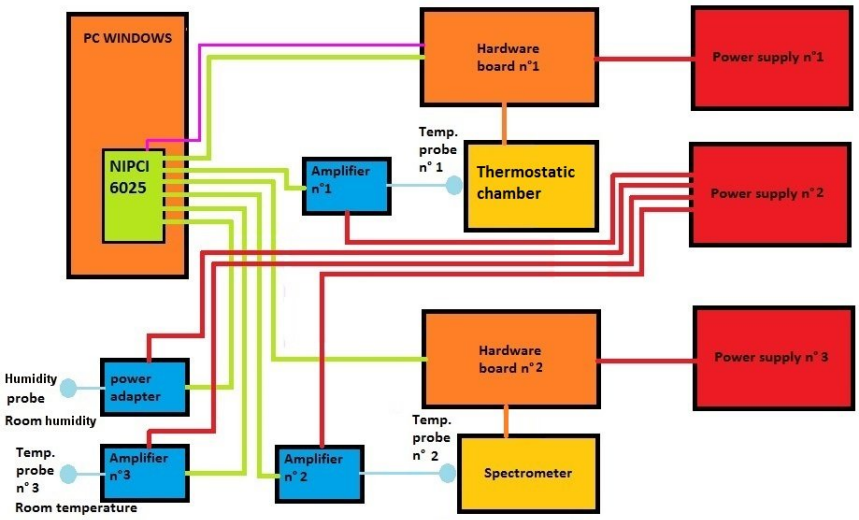

Figure 3.3.4: Functional block diagram of the system. The red links represent the power supply lines, the light blue ones indicate the signal of each probe, the green lines refer to amplified signals from the temperature sensors and also to the control signals for the two hardware board, the violet one is the digital signal that control the inversion of the current in the Peltier cells and finally the orange lines are used to indicate the current signals for the Peltier cells.

the data trends in run-time. The program is composed by a continuous loop executed every 100 milliseconds, a time more than enough to correctly control the slow temperature variations. Before executing the loop, the program sets up the initial conditions of the variables used in the program, the analog channels, the data file name and its path. Inside the loop the temperature and humidity reading values are registered, the variables of the two PID controllers (storage chamber and spectrometer) are calculated and the relative output are updated, the data are saved on a file and finally the graphs are visualized in front panel. After the loop, which can be closed only from the front panel, settings of the analog channels are closed, as well as the data file. A second parallel loop manages the reading of a button dedicated to the thermostatic chamber control. Its value orders the cooling or the heating in relation of the temperature set as goal. These two modalities are actuated by means of a relè which invert the current into the Peltier cells.

A detailed explanation of the program is presented in Appendix B.

3.3.4 National NI PCI 6025E board description

As previously said, this board, through the computer's PCI bus, allows to interface the external analog and digital signals with the LabVIEW software.

The board can operates with several signals: up to eight differential analog 12 bit input, two analog 12 bit output, thirty two digital input/output and two 24 bit counter/timers. It uses only one ADC with max sample/rate of 200kS/s and a DAC with max sampling/rate of 10kS/s.

For this application four differential analog input (temperature and humidity sensors), two analog output (hardware board control) and one digital output (relè inversion current control) have been used.

3.3.5 Temperature control hardware board

As previously explained, a first hardware board has been constructed in the laboratory to adequately pilot the current into the thermostatic chamber Peltier cells. Successively another board, analogous to the previous one, has been assembled in order to thermostat the NIR spectrometer. The construction of these boards was needed both to drive, at hardware level, the current into the cells in Pulse Width Modulation (PWM, see Appendix A), avoiding thermal dissipation problems in the power element (MOS-FET), and to not directly generate the PWM signal by LabVIEW software, already employed in several other elaborations.

Each hardware board is constituted by three principal blocks: a micro-controller PIC16F876A, an integrated driver Tc4469 and a MOS-FET IRLI3705N. The micro-controller receives the analog signals from the National NI6025 board, the input is transformed in a PWM signal and sent to the integrated driver. The Tc4469 amplifies (current amplification) a first time the input and sends the output to the MOS-FET gate.With another current amplification, the MOS-FET can drive the Peltier cells.

An extended description of the full circuit is available in Appendix C.

3.3.6 Temperature probes amplifier and power supply humidity circuit

As already indicated, the complete system exploits three integrated temperature sensors LM35 by Texas Instruments. These devices offer an accuracy of ± 0.4°C for all the functional temperature range which goes from -55°C to 150°C, but within the range chosen for the present work, from 5 to 50°C, the typical error is reduced to a maximal one of ± 0.1°C, more than enough for the purposes of this elaboration. These probes generate an output of 10mV/°C. Because there was the necessity to be able to make measurements with storage temperature as low as few Celsius degrees, which have very low output voltage, the output probe signals had to be amplified by a factor of 10. The amplification has been made using an amplifier INA128 (by Burr Brown), having a CMR of 120 db, a low offset and a drift offset of 0.5μV/°C.

For the humidity sensor, Honeywell HIH-5030, an application circuit suggested by the constructor has been used. It was decided to power the sensor with 3.3V, because this voltage is the typical value used in the humidity sensor data-sheet for the realization of the major part of the sensor characteristic curves. The 3.3V has been obtained from a LM317 by National Semiconductor, a regulator able to supply stabilized tensions ranging from 1.2V up to 40V. The humidity sensor output is elaborated, inside the LabVIEW program, by means of an equation that takes count of the output behavior in relation to the voltage supply. The *relative humidity* is obtained by the equation

$$HR = V_{supply}\,(0.00636 \cdot V_{out,sensor} + 0.1515)$$

. This circuit permits to measure the relative humidity in a range that goes from 11% up to 89% with a maximum accuracy of $\pm 3\%$.

A detailed description of the temperature probes amplifier and the humidity sensor power supply circuit are reported in Appendix D.

3.3.7 Thermostatic chamber performance

The long-time constant-temperature maintenance (up to twenty days) of a cuvette filled with solution of SWCNTs was tested for several temperatures beginning with 5°C to 35°C with a step of 5°C. The humidity of the measuring hall was also controlled and always maintained low enough to prevent water condensation of the cuvette. Thus measurements of the fluorescence emissions were also possible to be carried out. Figure 3.3.5 shows time plots of four temperatures of the thermostatic chamber: 5°C, 10°C, 30°C and 35°C. The temperature of the environment is also shown in the figure to give an idea about the conditions of the measuring hall. One can clearly see the rapid temperature change of the thermostatic chamber in the beginning of each plot, and its smooth horizontal-line part after the setup temperature is achieved.

Table 3.6 demonstrates the results from the measurements of the temperature in the thermostatic chamber with the cuvette holder. The storage time for each of the temperatures maintained in the chamber exceeded 10 days. The temperature measurements were made in intervals of 6 seconds and were registered by the computer. Thus the values shown in Table 3.6 are averaged values from a large number of temperature measurements.

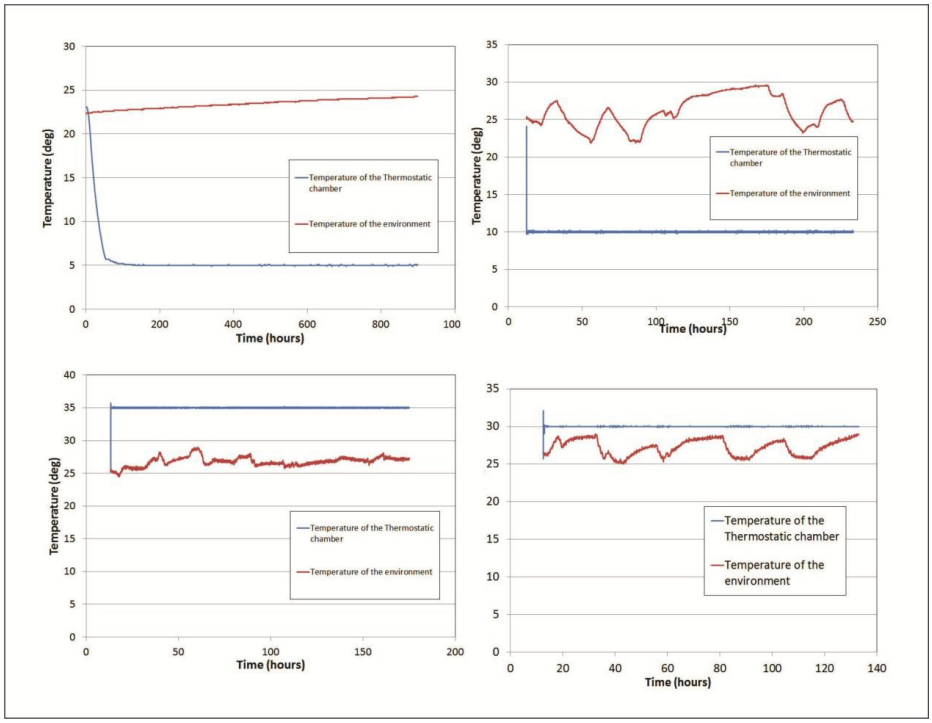

Figure 3.3.5: Temperature of the thermostatic chamber as a function of the storage time for 4 different storage temperatures (blue lines). The temperature of the air in the laboratory is shown in red. Taken from [80]

Table 3.6: Measurements of the average temperature in the thermostatic chamber with the cuvette holder for several storage-time temperatures. Taken from [80]

Storage temperature set (°C)	Average temperature (°C)	Standard deviation (°C)	Minimum temperature measured (°C)	Maximum temperature measured (°C)
5	5.0088	0.035	4.9	5.1
10	10.0009	0.057	9.7	10.2
15	14.9996	0.0155	14.9	15.1
20	19.9997	0.0237	18.8	21.1
25	25.0552	0.3765	24.8	26.7
30	30.0013	0.0620	29	32.1
35	35.001	0.0391	34.4	35.7

Chapter 4

Measurements of the NIR light emission of SWCNTs

4.1 SWCNTs preparation procedure

As explained in chapter 2, besides the methodology used to produce it, e.g. laser ablation [81], chemical vapor deposition [82], arc-discharge [83], etc., is always characterized by an ensemble of tubes species, having different chiralities, which are aggregated into bundles held together by van der Waals (vdW) forces [66]. Recalling the fact that CNTs optical properties are affected by the bundling of tubes [1], a procedure that applies a non-perturbing coating to prevent re-aggregation is needed. There are a large number of methodologies, including covalent and non-covalent stabilization of SWCNTs, that can be adopted to prepare a stable and homogeneous dispersion of SWCNTs. The non-covalent approaches have gained a particular interest because they leave intact the surface structure and properties of the nanotubes. Another important aspect that must be taken into account is the dissolution in water of the SWCNTs, which are naturally a highly water insoluble material. Aqueous solutions of carbon nanotubes are essential for their potential biomedical applications (*e.g.,* chemical and biological sensors in aqueous environments such as living cells) and biophysical processing schemes [86].

Surfactants are widely used in the standard procedures to prepare aqueous dispersions of *SWCNTs*. In a typical surfactant-aided dispersion procedure, sonication is exploited as an external energy input to overcome the strong vdW attractions, leading to the debundling or exfoliation of the carbon nanotubes bundled ends, as shown in (ii) of figure 4.1.1. Subsequently, the separated bundled ends provide new adsorption sites for the surfactant molecules which cover[2] the SWCNT free surface, as can be seen in the magnification circle of (iii). Therefore, the energy repulsive potential resulting from the adsorbed surfactant

[1] the net effect results in a virtual absence of near-IR emission

[2] by means of hydrophobic or π-π interactions

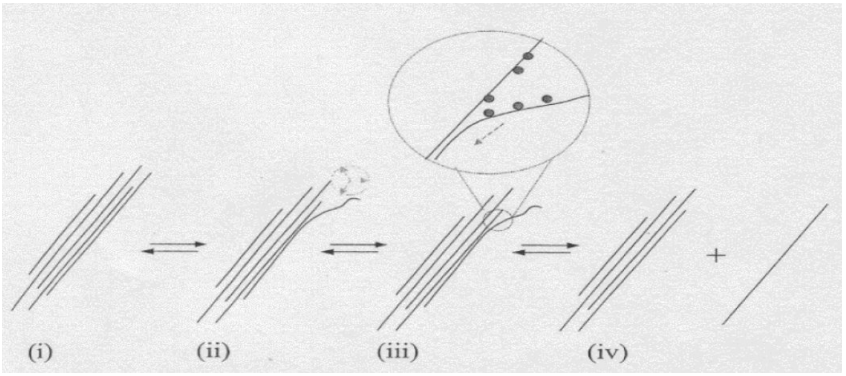

Figure 4.1.1: Proposed mechanism of nanotube isolation from bundles. (i) Ultrasonic processing "frays" the bundle end. (ii) The bundle end becomes a site for additional surfactant adsorption. (iii) Process continues in an "unzippering" fashion. (iv) Process terminates with the release of an isolated, surfactant-coated nanotube in solution. Taken from [88].

molecules[3] further enhances this separation process. In this "unzippering" fashion, isolated surfactant-coated SWCNTs are eventually released to the aqueous solution, as shown in (iv) of figure. Since an individual nanotube covered by surfactant molecules has a density similar to water, centrifugation for long periods of time is needed to separate carbonaceous impurities and large SWCNT bundles from isolated SWCNTs [45]. With a second sonication step, a further increase in the fraction of individual tubes in the suspension may be reached by separation of the small-size bundles that are still present in the aqueous solution [84].

Among the large number of surfactants employed, bile salts (biological detergents) have been shown to solubilize individual SWCNTs in aqueous solutions with high weight fractions [85]. The chemical structure of the bile salts is different from that of the usual linear surfactant, which are characterized by a hydrofphilic head and a hydrophobic tail. They are rigid facial amphiphiles, possessing a quasiplanar, slightly bent but rigid steroid ring, with a hydrophilic face and a hydrophobic face residing back-to-back. As a result of their unique chemical structure, bile salts act as very effective dispersants of biological molecules in living cells, including fat-soluble vitamins, bilirubin, and cholesterol. The most common bile salt is the sodium cholate (SC),its chemical structure is shown in figure 4.1.2, where it can be seen that the hydrophobic face is constituted by the hydroxyl groups and the charged carboxylate group, while the methyl groups and the tetracyclic carbon backbone constitute the hydrophilic face [86].

The slightly bent but rigid steroid ring owned by the bile salts, seems to be very effective in the accommodation of the molecules onto the SWCNT curve surface and, as a result, they can better enhance the dispersion stability of

[3]electrostatic for ionic surfactants and steric for nonionic surfactants

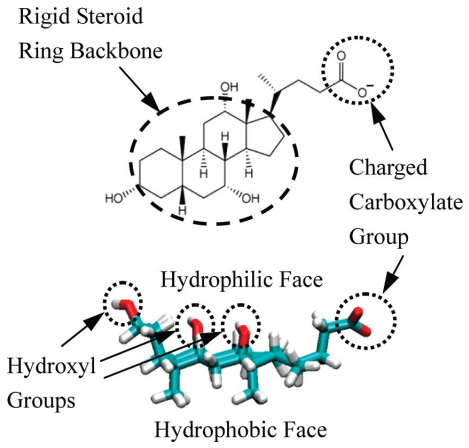

Figure 4.1.2: Schematic (top) and spatial (bottom) chemical structures of sodium cholate, a common bile salt surfactant, showing the rigid steroid ring backbone, the hydrophobic and hydrophilic faces of the molecule, the hydroxyl groups (OH), and the charged carboxylate group (COO-). In the spatial chemical structure red indicate oxygen, light green for carbons and white for hydrogens. Taken from [86].

SWNTs in aqueous solutions [86]. Figure 4.1.3 shows a computer simulation where cholate ions wrap around the SWCNT like a ring with the hydrophobic faces pointing inward and the hydrophilic faces pointing outward.

In this thesis, sodium cholate hydrate[4] (Sigma-Aldrich, product C6445-10G, $C_{24}H_{39}NaO_5 \, x \, H_2O$) has been used to prepare two types of SWCNT aqueous solution samples: a first batch have been made using CoMaCAT[5] SWCNT with chirality (6,5) (Sigma-Aldrich product 704148-250MG, carbon $> 90\%$, carbon as SWNT $\geq 77\%$, 0.7-0.9nm tubes diameter) and a second batch made with CoMaCAT SWCNT with chirality (7,6) (Sigma-Aldrich product 704121-250MG, carbon $> 90\%$, carbon as SWNT $\geq 77\%$, 0.7-1.1nm tubes diameter).

Preparation procedure

To prepare the nanotube suspensions, a quantity of 46.5mg of sodium cholate hydrate (C6445-10G) was added in a 50ml test tube and gently shaken with 25ml of milliQ water. Then 8.2mg of CoMoCAT SWCNT have been added to the solution and softly shaken. The resulting dispersion has undergone two treatments

[4] the therm *hydrate* means that water molecules are contained in the sodium cholate cristals

[5] CoMoCAT (CO disproportionation on bimetallic Co-Mo catalysts supported on silica). It is a catalytic Chemical Vapor Deposition (CVD) process, where SWNT are grown by CO disproportionation (decomposition into C and CO_2) at 700-950 ^{o}C in flow of pure CO at a total pressure that typically ranges from 1 to 10 atm in the presence of a Co-Mo catalyst supported on silica. SWNT produced with this method are characterized by very narrow diameter and chirality distributions. Depending on the specific reaction conditions (temperature, pressure), the CoMoCAT material can be composed of a very small number of nanotubes, with one of them dominating[84, 89].

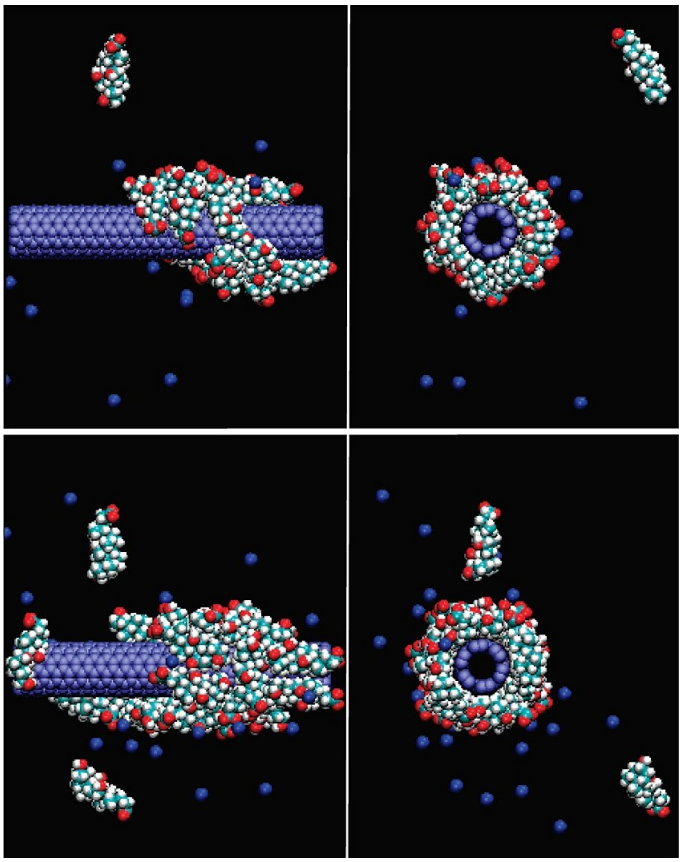

Figure 4.1.3: Postequilibrium simulation snapshots of SWCNTs covered with SC ions at two different total SC concentrations (lateral and front view). Color code: red – oxygen, light blue – carbon, white – hydrogen, dark blue – nitrogen, and purple – carbon in the SWCNT. Taken from [86].

of ultrasonication, in a water bath cooled with ice, by means of a horn sonicator (QSONICA Q125) running at 90% of its amplitude in order to ensure a power of at least 1W/ml. The sonicator settings were chosen in a way that ultrasonication cycles of 3 seconds were alternated with rests cycles of 3 seconds; in practice each sonication treatment had a total time duration of 60 minutes, with 30 minutes of effective ultrasonication. About the 70-80% of the sonicated dispersion was decanted in 14 eppendorf tubes. The eppendorf tubes have been inserted in a microcentrifuge (HERMLE refrigerated Z233MK-2) and centrifuged at 15000 rpm ($21380 \times g$) at 22°C for 40 minutes for two times. Only the upper part of the resulting supernatant contained in each eppendorf tube ($\sim$ the upper 20% of the solution) was taken and poured in a cuvette (VETROTECNICA Cod. 03.4600.17) for the fluorescence measurements (see figure 4.1.4).

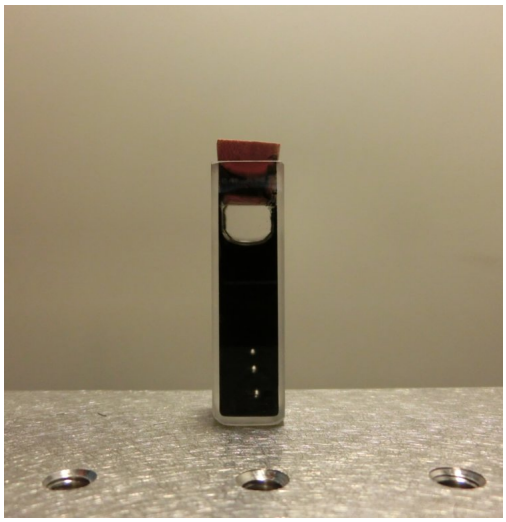

Figure 4.1.4: Image of the cuvette containing the SWCNT aqueous dispersion employed in the fluorescence emission measurements.

4.2 Data acquisition procedure

While the SWCNTs were undergoing the final centrifugation treatment, two preliminary operations had to be made: the calibration of the laser source and the start of the storage system. Before starting each set of measurements, *i.e.*, before the insertion of the cuvette in the storage chamber, the calibration of the optical power output was made by keeping active the laser source in continous mode[6] and rotating the optical attenuator disk up to read, on the powermeter dedicated computer window, an optical power of 25 mW, value kept constant for all the sets of measurements collected. The long time storage system had to be set at the desired storage temperature and started, approximately 15 minutes before the finish of the centrifugation, ensuring that the storage chamber had already reached the goal temperature at the moment of the cuvette insertion. Before starting the data acquisition, a "sample acclimatization time" of 1 hour was waited to let the solution reaching the same temperature of the storage chamber.

The data acquisition procedure was composed by two consecutive measurements, executed periodically along the duration of the data collection. A first measure of the background spectrum made without the excitation source (dark mode) followed by a second made with the laser source activated (laser mode)[7]. For every measure the spectrometer registered 100 acquisitions, each having an integration time of 100 ms, therefore each measure (in dark mode or in laser mode) had a duration of 10 s. These couple of measurements were repeated

[6] laser operational mode characterized by a beam output power constant over time.
[7] All the data were acquired using the laser in continuous mode

every 30 minutes along the first day of data collection, and then every hour for all the remaining days of acquisition. A set of measurements, gathered in 11-12 days, was characterized by two distinct factors: the chirality of the nanotubes employed in the sample solution and the storage temperature set.

4.3 Data elaboration procedure

As explained, each set of measurements was performed with a specific chirality sample kept under a specific storage temperature for two week. Each measure consisted in a pair of acquisitions, one made in dark mode and the other in laser mode. The spectrum used in the data elaboration was obtained by summing the 100 acquisitions made by the spectrometer for each modality, which gave a laser modality cumulative spectrum and a dark modality cumulative spectrum (*i.e,* background), and subtracting the latter from the former. To plot the data as function of the wavelength, the following calibration curve has been used:

$$wavelength = a_0 + a_1 \cdot pixel + a_2 \cdot pixel^2 + a_3 \cdot pixel^3 + a_4 \cdot pixel^4 + a_5 \cdot pixel^5,$$

where the coefficients $a_0, a_1, a_2, a_3, a_4, a_5$ were given directly by the spectrometer itself, and *pixel* goes from 1 to 512. Figures 4.3.1 and 4.3.2 report some spectra obtained at different times with this procedure for the batches (6,5) and (7,6) respectively, kept under a storage temperature of 35°C and 30°C.

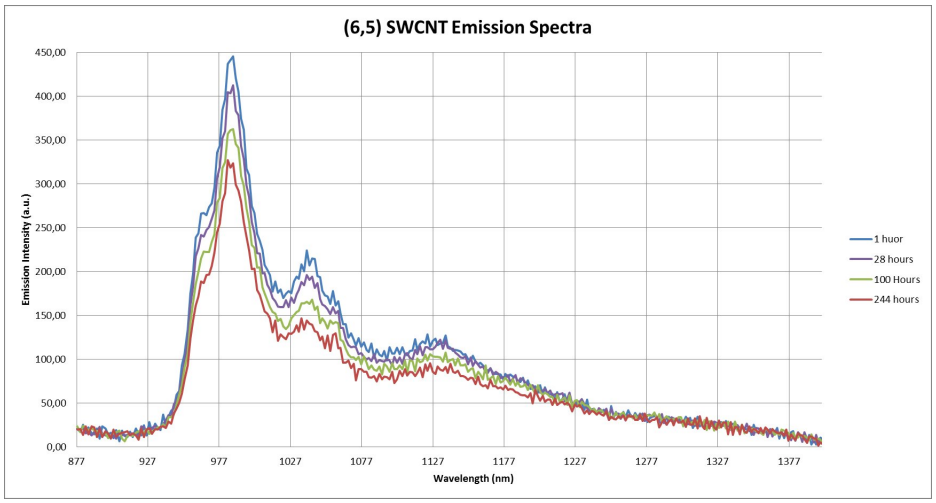

Figure 4.3.1: Examples of spectra collected after 1 hour (blu line), 28 hours (violet line),100 hours (green line) and 244 hours (red line) from the insertion of the sample in the storage system for a batch of (6,5) SWCNTs at 35°C.

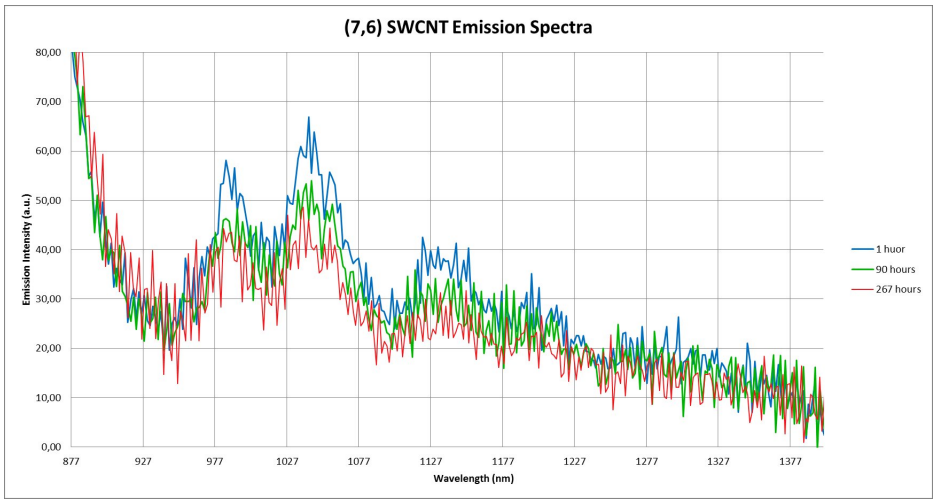

Figure 4.3.2: Examples of spectra collected after 1 hour (blu line), 90 hours (green line), and 267 hours (red line) from the insertion of the sample in the storage system for a batch of (7,6) SWCNTs at 30°C.

As reported in chapter 2 the spectrum is characterized by the presence of several peaks produced by the fluorescence emission of different (n,m) species of SWCNTs which inevitably are present in the sample. To better understand which SWCNT species were involved in the origin of each emission peak, the spectrum obtained for each of the two samples have been fitted with Lorentzian profiles, where each profile was associated to a specific semiconducting nanotube (n, m). The fit was made by approximating the spectrum data with ten Lorentzian profiles (*i.e.,* ten SWCNT), and successively associating each position peak (λ_k) to the closest transition wavelengths available in the literature data for the E_{11}^S transitions [8] [91]. Moreover, from the transition wavelengths reported by the literature, only those related to tubes having diameters between 0.7 nm and 0.9 nm contribute to the (6,5) sample spectrum, because these are the only tubes contained in the sample as declared by the producer. The same goes for the (7,6) sample, where only tubes having diameters between 0.7 to 1.1 nm have to be used. Figure 4.3.3 shows the (7,6) sample spectrum fitted with ten nanotubes.

[8] The spectral region between 900 and 1600 nm is characterize only by $E^S{}_{11}$ transitions

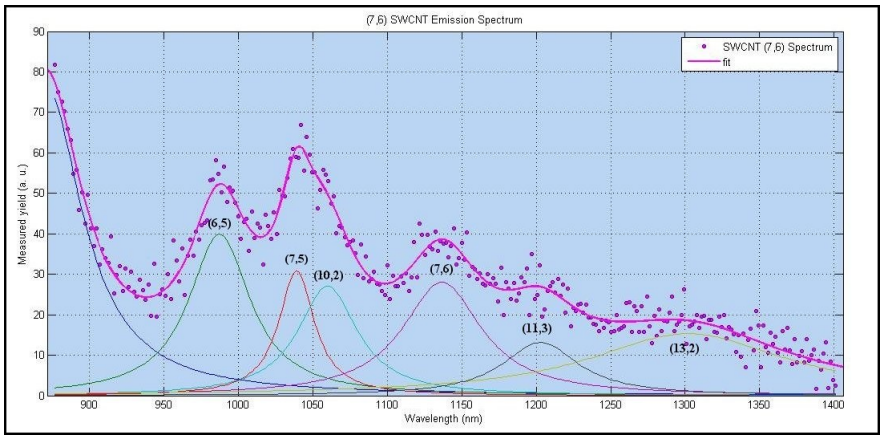

Figure 4.3.3: Example of deconvolution of the (7,6) sample spectrum by means of ten Lorentzian profiles. The nanotubes that mainly contribute to the formation of the emission peaks have been reported over the relative peaks.

However, since each electronic state has associated vibronic states[9], environmental and excitonic effects on the nanotube create intermediate electronic states, which are responsible of minor states that accompany the major electronic transition, causing a broadening in the absorption and emission line shape. For this reason, a Voigt profile is more accurate rather than a Lorentzian, since it represents a combination of natural line broadening due to uncertainty in particle lifetimes (Lorentzian contribution) and Doppler broadening due to a distribution of particle velocities (Gaussian contribution). This happens because the Voigt profile is a convolution of Gaussian and Lorentzian line shapes [90, 92]. The Voigt line shapes centered in wavelength $\lambda_{(n,m)}$, represent the spectral contribution of the (n, m) nanotubes in the spectrum. Figure 4.3.4 shows the Voigt deconvolution made with ten Voigt profiles for the spectrum of the (6,5) sample.

[9] Franck-Condon principle

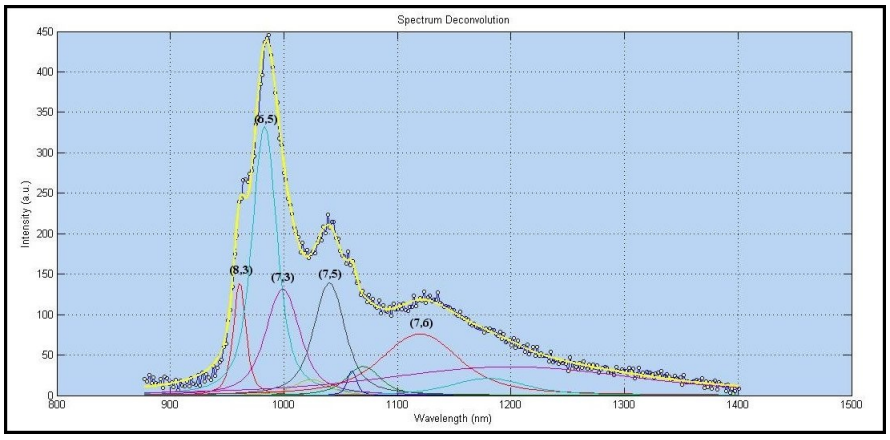

Figure 4.3.4: Example of deconvolution of the (6,5) sample spectrum by means of ten Voigt profiles. The nanotubes that mainly contribute to the formation of the emission peaks have been reported over the relative Voigt profile.

4.4 Emission of SWCNTs as a function of the storage time

In order to make some quality consideration about the stability of the fluorescence emission, the spectrum has been divided in three different spectral regions, each characterized mainly by an emission peak. The emission fluorescence yield has been obtained by taking for each of these regions the area subtended the spectrum profile, *i.e.* summing the measured intensity counts between the wavelength characterizing the peak region borders. It must be underlined that these regions were kept identical for all the set of measurements obtained for a specific chirality sample. In figures 4.4.1 and 4.4.2 are shown the spectra related to each batch showing the chosen regions.

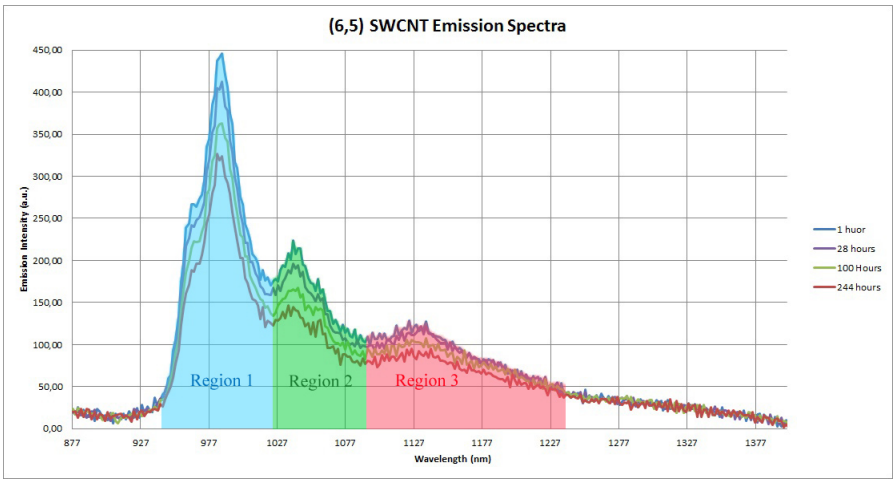

Figure 4.4.1: Regions chosen in the (6,5) sample spectrum for the evaluation of the fluorescence emission.

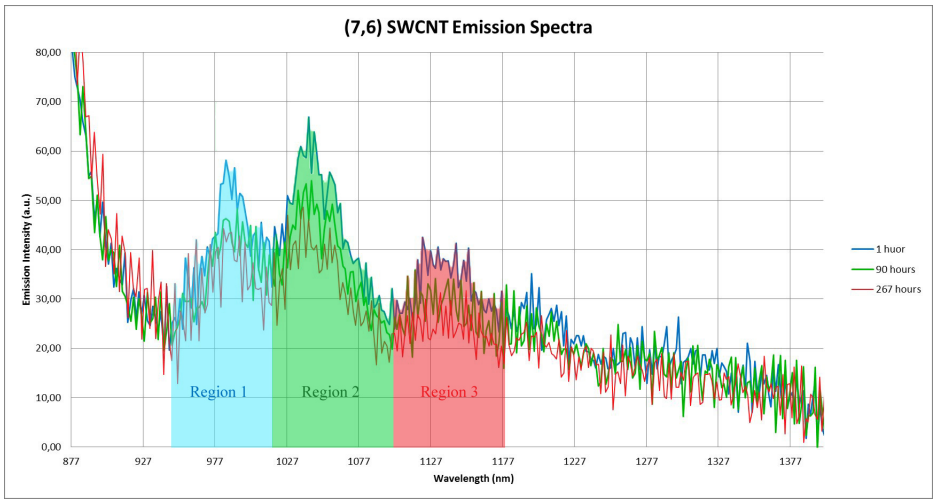

Figure 4.4.2: Regions chosen in the (7,6) sample spectrum for the evaluation of the fluorescence emission.

The fluorescence measured yield has been plotted as a function of the storage time, showing a similar fading behavior of that observed in reference [73]. In order to characterize the fluorescence emission fading, the data have been fitted using the MATLAB software using as fit function:

$$y(t) = A \cdot e^{-a \cdot t} + B \cdot e^{-b \cdot t},$$

where $y(t)$ is the fluorescence yield, t is the storage time and A,B,a,b are the free parameters of the fit. The first exponential describes the initial part of the data, where the fading is more pronounced, while the latter has a major contribution in describing the long term behavior of the data trend. All the parameter estimates were computed setting to 95% the confidence intervals.

In figure 4.4.3, figure 4.4.4 and figure 4.4.5 are shown the fluorescence yield data as a function of the storage time, with the relative fits for the SWCNT (6,5) sample at 35°C and 30°C and SWCNT (7,6) at 35°C respectively.

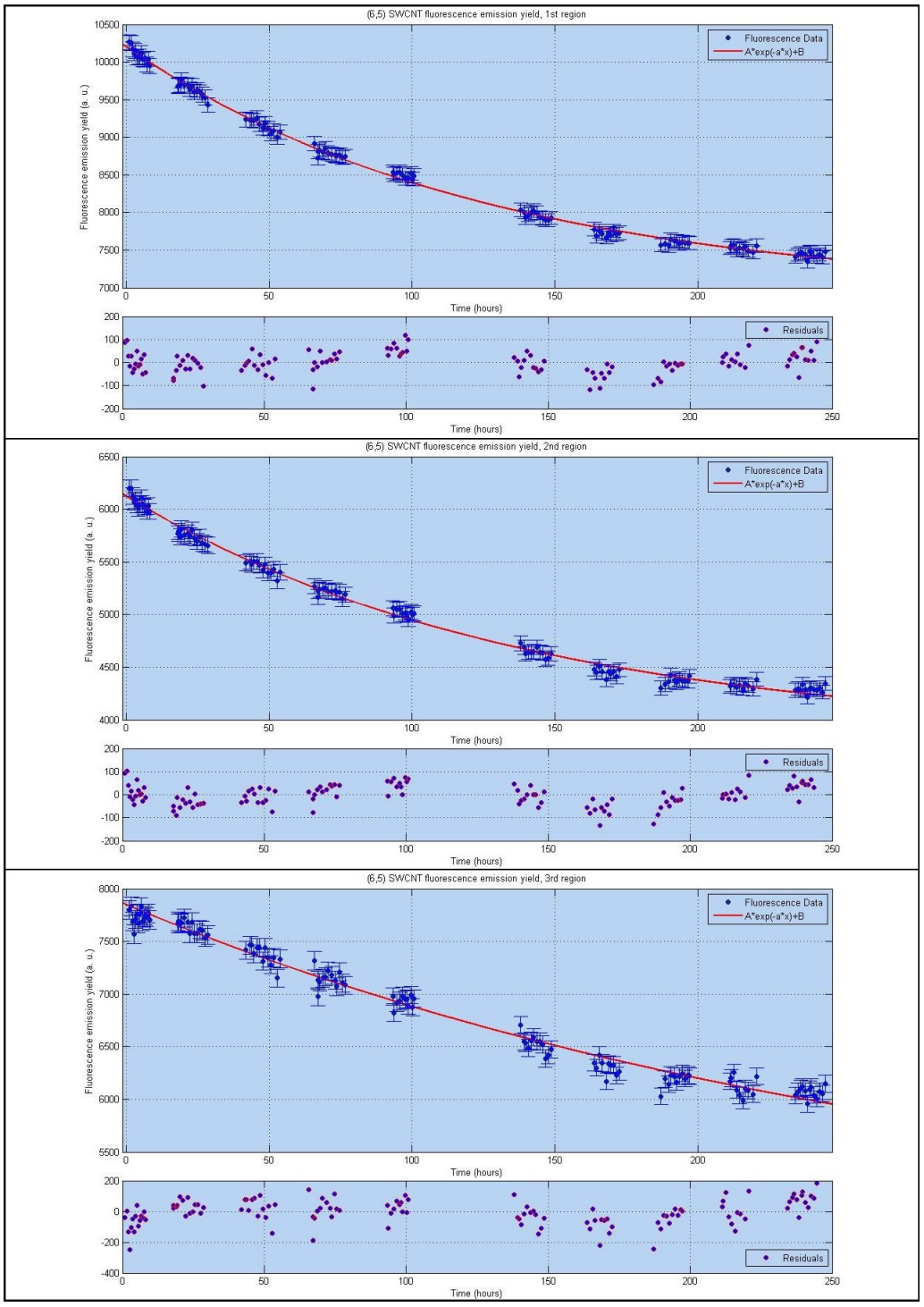

Figure 4.4.3: SWCNT (6,5) sample fluorescence emission fits for all the spectrum regions at the storage temperature $T_{storage} = 35°C$. From the top to the bottom: fluorescence yield data, fits and residuals for region1, region 2 and region 3.

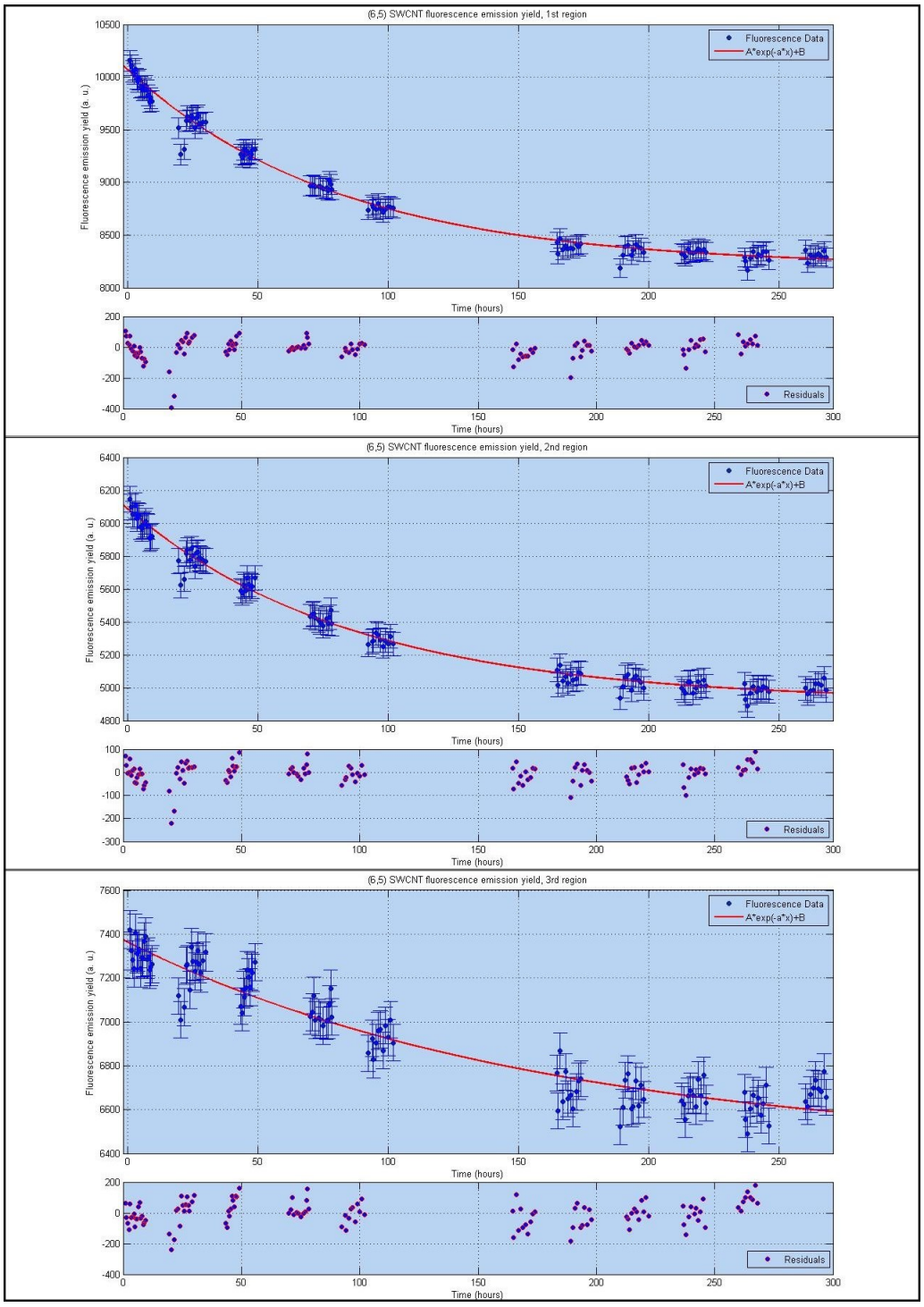

Figure 4.4.4: SWCNT (6,5) sample fluorescence emission fits for all the spectrum regions at the storage temperature $T_{storage} = 30°C$. From the top to the bottom: fluorescence yield data, fits and residuals for region1, region 2 and region 3.

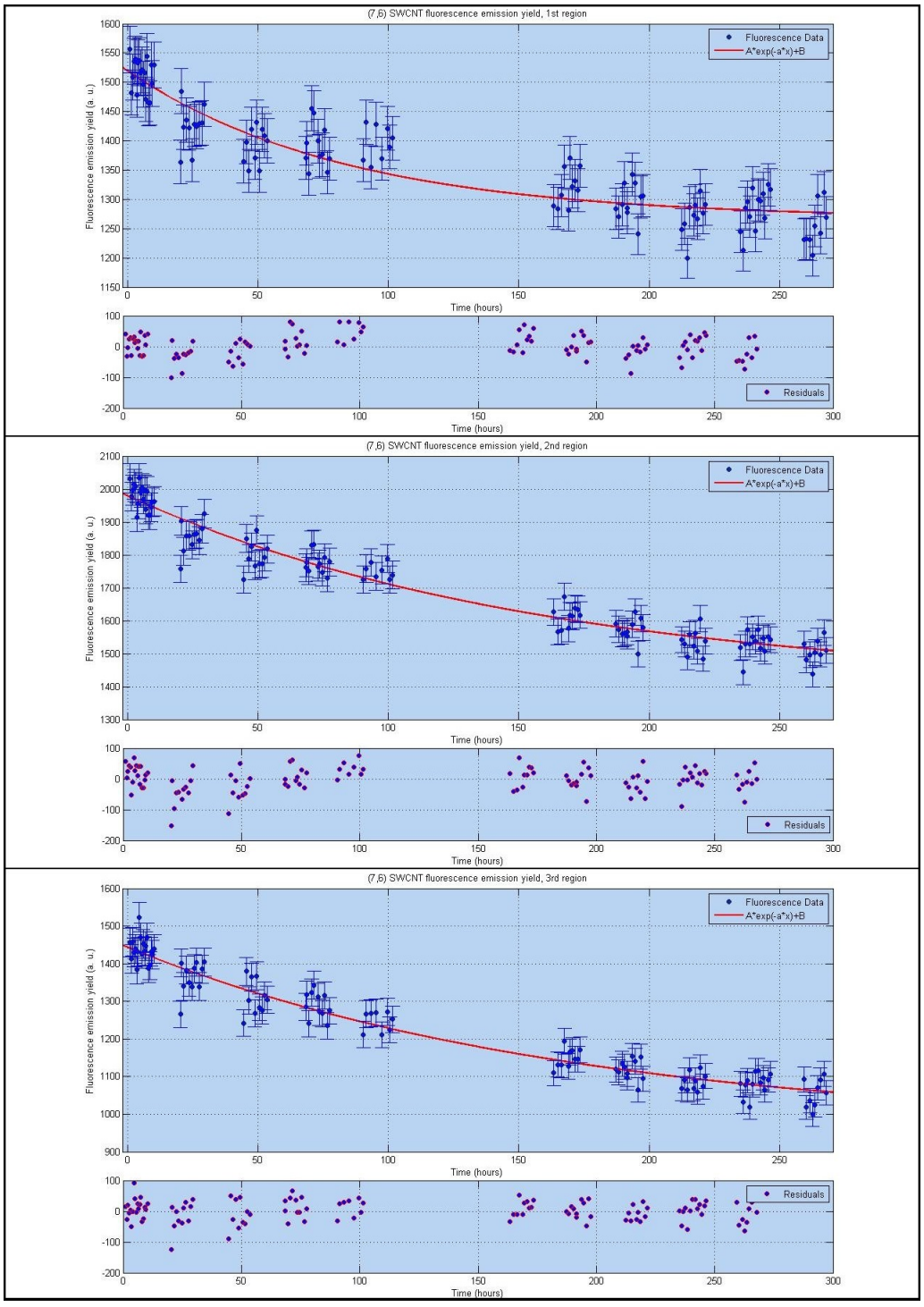

Figure 4.4.5: SWCNT (7,6) sample fluorescence emission fits for all the spectrum regions at the storage temperature $T_{storage} = 30$°C. From the top to the bottom: fluorescence yield data, fits and residuals for region1, region 2 and region 3.

While performing these fits with the double exponential model function, the parameter b was always fixed at bound ($\sim 10^{-11}$) by the software, suggesting that the data would have been better described by a function of the type:

$$y(t) = A \cdot e^{-a \cdot t} + B.$$

All the fits for the SWCNT (6,5) sample have shown this behavior, while some of the (7,6) sample allowed also a solution with a double exponential behavior. However, in this last cases, the uncertainties of the fading parameters of the first exponential were greater than 50%. For this reason the fits made with one exponential and a constant have been preferred even for the (7,6) sample. Table 4.1, table 4.2 and table 4.3 report the fit parameters obtained for the two samples at the different temperatures..

Table 4.1: Fit parameters evaluated for the (6,5) sample with $T_{storage} = 35°$C.

	A (a.u.)	a ($hours^{-1}$)	B (a.u.)
Region 1	3272 ± 52	$(8.0 \pm 0.3) \cdot 10^{-3}$	6930 ± 59
Region 2	2275 ± 60	$(7.3 \pm 0.5) \cdot 10^{-3}$	3848 ± 68
Region 3	3267 ± 399	$(3.5 \pm 0.7) \cdot 10^{-3}$	4583 ± 415

Table 4.2: Fit parameters evaluated for the (6,5) sample with $T_{storage} = 30°C$.

	A (a.u.)	a ($hours^{-1}$)	B (a.u.)
Region 1	1870 ± 26	$(12.3 \pm 0.5) \cdot 10^{-3}$	8203 ± 25
Region 2	1173 ± 21	$(11.5 \pm 0.6) \cdot 10^{-3}$	4915 ± 21
Region 3	947 ± 115	$(6.3 \pm 1.8) \cdot 10^{-3}$	6417 ± 130

Table 4.3: Fit parameters evaluated for the (7,6) sample with $T_{storage} = 30°$C.

	A (a.u.)	a ($hours^{-1}$)	B (a.u.)
Region 1	253 ± 19	$(11.9 \pm 8.9) \cdot 10^{-3}$	1267 ± 19
Region 2	577 ± 57	$(6.3 \pm 1.4) \cdot 10^{-3}$	1403 ± 64
Region 3	485 ± 52	$(5.9 \pm 1.4) \cdot 10^{-3}$	959 ± 58

From the estimates obtained for the fading factor in the exponential term of the fluorescence emission yield fits , it was possible to calculate the half-time coefficients associated to each region, SWCNT sample and storage temperature. These values are reported in table 4.4.

Table 4.4: Half-time coefficients

	$\tau_{1/2}$ (hours)		
Region 1	(86.5 ± 3.5)	(56.3 ± 2.5)	(58.0 ± 15.0)
Region 2	(95.1 ± 5.9)	(60.1 ± 3.4)	(110.7 ± 25.3)
Region 3	(197.1 ± 37.2)	(110.6 ± 31.4)	(117.7 ± 28.4)
	(6,5) sample $T_{storage} = 35$°C	(6,5) sample $T_{storage} = 30$°C	(7,6) sample $T_{storage} = 35$°C

Unfortunately, only three set of measurements have been presented in this thesis, several of them have been made for all the temperatures ranging from 10°C to 35°C by step of 5°C for both (6,5) and (7,6) chirality samples. These measurements have been progressively used as feedback for the storage/acquisition system settings optimization. In fact, as explained in chapter 3, the system has been modified and rearranged several times in order to overcome different problems arisen during the optimization process and guarantee the best evidence for the SWCNTs fluorescence emission fading behavior. For these motives, it has been decided to not include the sets of measurements that were made before reaching the final system setting that has been employed to obtain the data presented in this chapter.

Conclusions

A long-term constant-temperature storage compartment for the solution with NIR emitting nanoparticles has been designed, constructed, tested and incorporated in the setup for NIR studies. The fluorescence emission of SWCNTs suspended in sodium cholate aqueous solutions possessing two different types of chirality has been collected for periods of about 250 hours and studied as a function of the storage time and storage temperature. The spectra corresponding to the two chirality solution samples have been divided in three regions, each associated to a main emission peak. It was found out that the emission yield of each spectral region for both SWCNTs chirality samples has a fading storage-time dependent behavior, which confirms the previous research made by the LARIM research team. The fading behavior shown by the data can be described by a storage-time dependent exponential function summed with a constant term. The analysis of the exponential coefficients have been made for each spectral region for different storage temperatures. We have found that the three emission regions in which the NIR spectrum have been subdivided undergoes the same fading behavior but with different half time coefficients for the exponential part. The variation of the total fluorescence emission yield in a time scale of 24 hours varies from 6% to 4% for the spectral regions 1 and 2 and between 4% to 2% for the region 3 of the three data sample. Extending the time scale to 10 days the fluorescence emission yield varies between 27% and 16% for the first region, from 31% to 18% for the second and from 24% to 10% for the third region. The fact that this variation is little when compared to the half time coefficients of the exponential fit is explained essentially by the presence of the constant term B in the fits, which, in fact, represents the main contribution to the total fluorescence emission yield. Probably the long time scale necessary to observe an appreciable variation in the SWCNTs fluorescence emission is the reason why the SWCNTs fluorescence emission has been up to now considered stable. The fading behavior, is most probably due to some processes of re-aggregation of the SWCNTs in the solution [74, 86]. The temperature-dependence of the fading behavior suggests the need to perform further measurements to evaluate and explain the origin of this phenomenon. The results of this experiment suggest the possibility to apply sufficiently good corrections to the observed emission of SWCNTs, knowing the time passed after the nano-tubes preparation and the coefficients in the exponential term. These corrections can be very important in the development of SWCNT sensors with long lifetimes.

Appendix A

PWM (Pulse-Width Modulation)

PWM (Pulse-Width Modulation) it is a type of digital modulation which allows to obtain a average voltage in the period dependent from the *duty-cycle (dc),* which is the fraction of signal period T in which a signal (or system) is active [99]. Referring to figure A.0.1, the duty-cycle can be defined as

$$dc = ton/(ton + toff),$$

where *ton* is the time duration in which the signal is on and *toff* is the time duration in which the signal is off. The period T is the time it takes for a signal to complete an on-and-off cycle, therefore

$$\mathrm{T} = ton + toff.$$

If one consider a pulse waveform $V(t)$, with period T, low value $V_{\min}$, a high value $V_{\max}$ and a duty cycle dc , the average value of the waveform $\overline{V}$ is given by:

$$\overline{V} = \frac{1}{\mathrm{T}} \int_0^{\mathrm{T}} V(t)\, dt$$

.

As $V(t)$ is a pulse wave, its value is $V_{\max}$ for $0 < t < dc \cdot \mathrm{T}$ and $V_{\min}$ for $dc \cdot T < t < T$. The above expression then becomes:

$$\overline{V} = \frac{1}{\mathrm{T}} \int_0^{\mathrm{T}} V(t)\, dt = \frac{1}{\mathrm{T}} \left(\int_0^{\mathrm{dc}\cdot\mathrm{T}} V_{max}\, dt + \int_{\mathrm{dc}\cdot\mathrm{T}}^{\mathrm{T}} V_{min}\, dt \right) = dc \cdot V_{max} + (1 - dc) \cdot V_{min}.$$

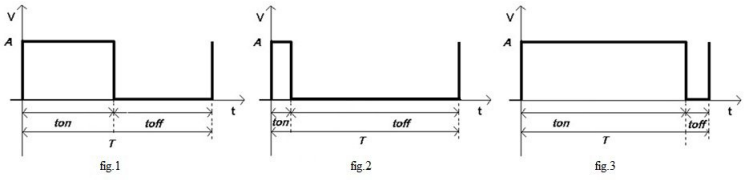

Figure A.0.1: Duty cycle examples for rectangular pulses. fig.1 dc=50%, fig.2 dc=10%, fig.3 dc=90%.

If one consider, as in figureA.0.1, $V_{\min} = 0$ and $V_{max} = A$, the previous expression can be simplified as $\bar{V} = dc \cdot A$, where it can be easily see the direct dependence of the average value of the signal $\overline{V}$ from the duty cycle dc.

If the duty-cycle is $dc = 50\%$, as in fig.1 of figureA.0.1, one will have an output mean voltage of $\bar{V} = A/2$; if $dc = 10\%$, as in fig.2, the output mean voltage will be $\bar{V} = A/10$; if $dc = 90\%$, as in fig.3, the output mean voltage will be $\bar{V} = \frac{9}{10}A$ [97, 98].

Appendix B

LabVIEW program for temperature and humidity control

B.1 Description of the LabVIEW environment

In contrast with the principal standard programming languages that are based on text editor and key words for the code generation, LabVIEW (Laboratory Virtual Instrument Workbench) uses the G language, abbreviation for Graphic Language, denominated VI (Virtual Instrument) given its natural predisposition for data acquisition system. A Virtual Instrument is formed essentially by two elements called *front panel* and *block diagram*.

The *front panel* is the user interface of the program and it is the program application which is viewed by the user while the program is running. Inside the user interface there are buttons, graphs, indicators and all what the user needs to manage the program in run-time.

The *block diagram* is considered the " program source code", and is represented by scheme of functional blocks that are interconnected with colored lines. Each line represents a type of data, and in this fashion every block input or output is strictly associated to a precise type of data. Within a block diagram it is possible to insert breakpoints, probe, execution condition, etc. , and debug the program as well as in any other development environment.

As can be seen in figure B.1.1 the program is formed by a time loop that is executed every 100ms (complete cycle of elaboration). Outside the loop, in the left side of the block diagram, there are all the initial settings which regard the calculation variables and the input and output channels characterizations. These settings are executed at the start of the program in order to set the correct initial conditions. All the instructions that are within the time loop will be executed cyclically, updating the variables at each interaction, acquiring the

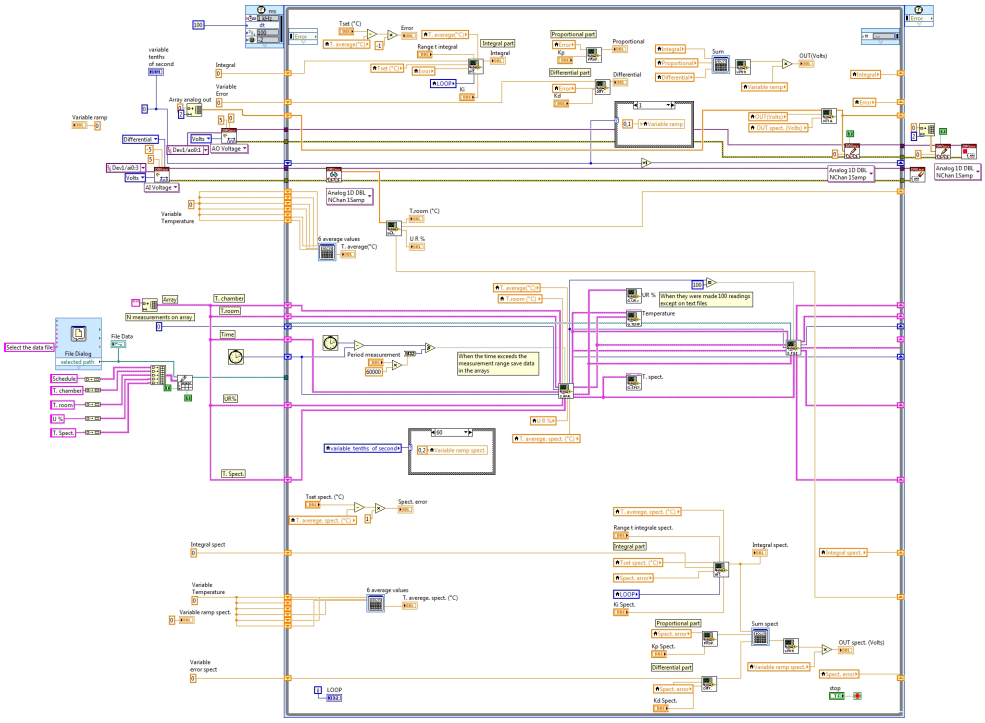

Figure B.1.1: Block diagram of the main program.

input signals and yielding the output signals. In the upper left corner there are the parameters that characterize the frequency of the loop: as it can be seen, an initial frequency of 1kHz is multiplied by a constant value of 100 in order to obtain a loop time of 100ms.

In the upper part of the block diagram it can be seen the PID elaboration with the three input constant k_p, k_i and k_d, as well as the *set temperature* variable (Tset, the target temperature of the chamber), that are all settable from the front panel by the user.

In the left side there is the initialization of the *Integral* and *Error* variables, that are useful to register the values between a precedent and a future loop. Below there are the array settings for the analogue output, for the analogue input and output channels and for the time type variable *tenths of seconds* that will be used to generate a "smooth ignition" of the Peltier cells, and finally the *Temperature* variable dedicated to the thermostatic chamber.

Inside the time loop, firstly the instant temperature of the storage chamber is acquired by the channel Ai0, which is linked with the chamber temperature probe, an average of six of these measure is made and then the *error* between the average and the set temperature is calculated. Exploiting the value of the *error* the three PID component are calculated and consequently summed

together. The program controls if the result falls between a max (4.9V) and a min (0V) thresholds, this is done for prevent the sending to the DAC of values that are out of its functional range, in order to not enter in condition not allowed by the system. The value obtained after this check is then multiplied by a variable called *ramp,* which permit to release gradually current to the Peltier cells avoiding too elevated and dangerous initial current. At the end the result is converted by the DAC in an analogue value and sends to the output channel Ao0 of the NIPCI6025E board. This analogue signal will control the PWM of the hardware board, which will drive the current of the Peltier cells mounted on the thermostatic chamber.

Another parameter involved in the PID elaboration and settable by the user is the *Range t integral*. This parameter specifies an interval range around the Tset temperature, inside which the integral part is taken into account. For major clarity in figure B.1.2, figureB.1.3, figureB.1.4, and figure B.1.5 are reported some details of the PID scheme.

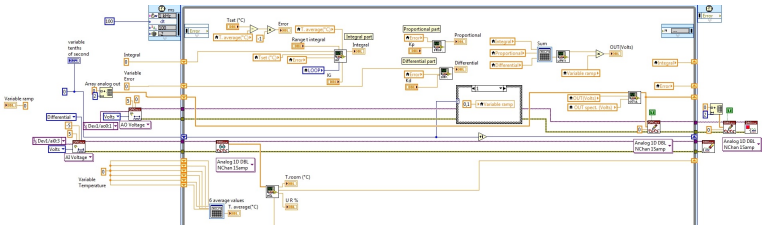

Figure B.1.2:

Figure B.1.3: Details of PID scheme

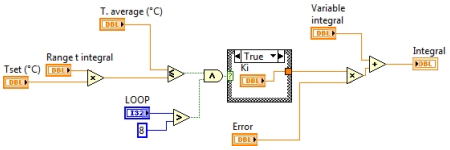

Figure B.1.4: Details of PID scheme

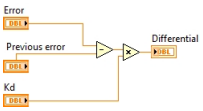

Figure B.1.5: Details of PID scheme

The central part of the loop manages all the data of temperature and time, inserting them into arrays and then periodically saving them onto a data file, in figure B.1.6 is shown a detail of the time loop containing this part. In the left part there are as always the initial settings that, for this part, regards the arrays of thermostatic chamber temperature, room temperature, spectrometer temperature, time and humidity. Moreover in this part are further created the text file for the data saving and the variable *Time* and *N measurements on array*, which are useful for the periodical saving of the data on file.

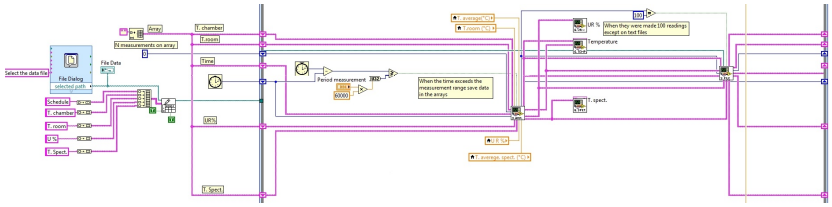

Figure B.1.6: Part of the program that operates the saving data onto array and file

Inside the loop, the variable *Period measurement* , settable from the user interface, indicates the time expressed in minutes between a measure of temperature and the successive, therefor in order to compare it with a measure of the time in milliseconds it is multiplied by an opportune constant. The result is then compared with the time passed from the starting of the system. This operation produces a logic trigger every time that a period of time equal to the value of *Period measurement* has elapsed.

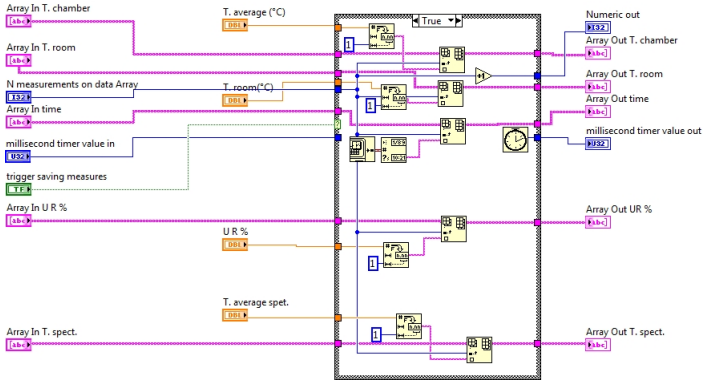

Figure B.1.7: Data saving onto array block diagram

In figure B.1.7 is shown a detail of the block diagram for the part concerning the data saving onto array. At each cycle these arrays will be visualized on instant graphs present in the front panel in order to allow the user to monitor the behavior of each variable. As an example in figure is shown the program

part relative to the visualization of the relative humidity (indicated as UR% in the panel).

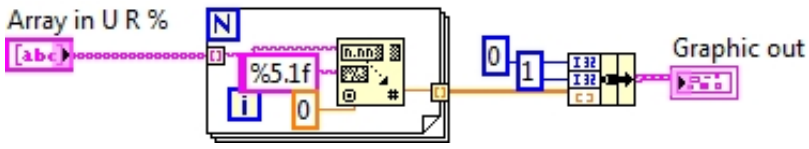

Figure B.1.8: Visualization UR% graph block diagram

For this central part of the program, as last operation the software moves all the data in the arrays onto the file excel, this operation is made every 100 mesurement and the event is controlled by the variable *N measurements on array*. In figure is reported the part of the program that save the data on file.

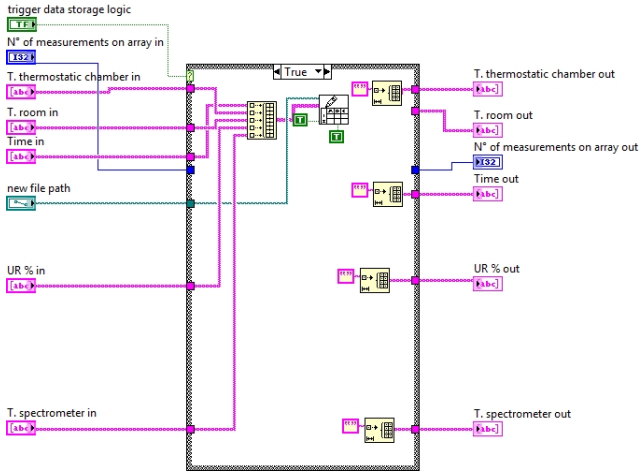

Figure B.1.9: Data saving on file block diagram

The lower part of the principal block diagram essentially is a copy of the PID program already described for the thermostatic chamber, with the only difference that this part is dedicated to the control of the spectrometer temperature. The variables and the constants have the same functions and the same goes for the input and output signals of the National board. This program section has been added because the NIR spectrometer (Hamamatsu mini-spectrometer TG series C9406GC) is not endowed with an inner system of temperature control. Therefore in order to avoid undesired effects due to eventual spectrometer inner temperature drifts, a cooler system was designed as well.

Finally a separated loop manages the reading of the push-button that impose the system the cooling or the heating of the thermostatic chamber depending on the goal temperature set. In practice the push button controls a logic signal

generated by the National board. By mean of a dedicated relè circuit presents on the hardware board, this logic signal inverts the cooling/heating function of the Peltier cells by the inversion of the current that flows through them.

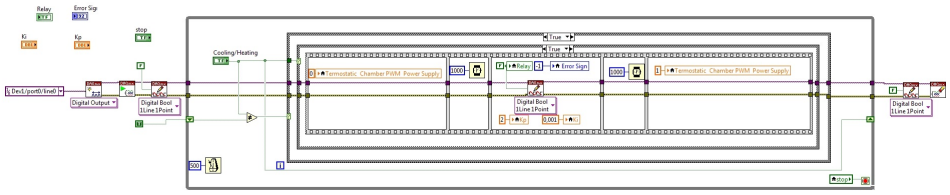

Figure B.1.10: Inversion current control block diagram.

Looking at the block diagram in figure B.1.10, in the left part of the loop, as usual, one can see the digital channel initial condition settings. Inside the loop, the push-button state is compared with its value at the precedent time loop cycle. Only if the comparison is negative (false) then the cooling/heating function is inverted. This operation is exploited with particular care: initially the PWM is switched off before the Peltier cells, then, after one second, the current is inverted by the relè, and only after another second of waiting the PWM is turned on again. This procedure is done both to spare some time to the relè for the commutation process and to prevent that the MOS-FET is still flown by current during the commutation, which could cause dangerous short circuits that could break the device. Moreover it must be precised that after the switching of the cooling/heating function the constants k_i and k_p are changed because the heating yield is higher than the cooling one and as a consequence the parameters have to be changed to equalize the two returns.

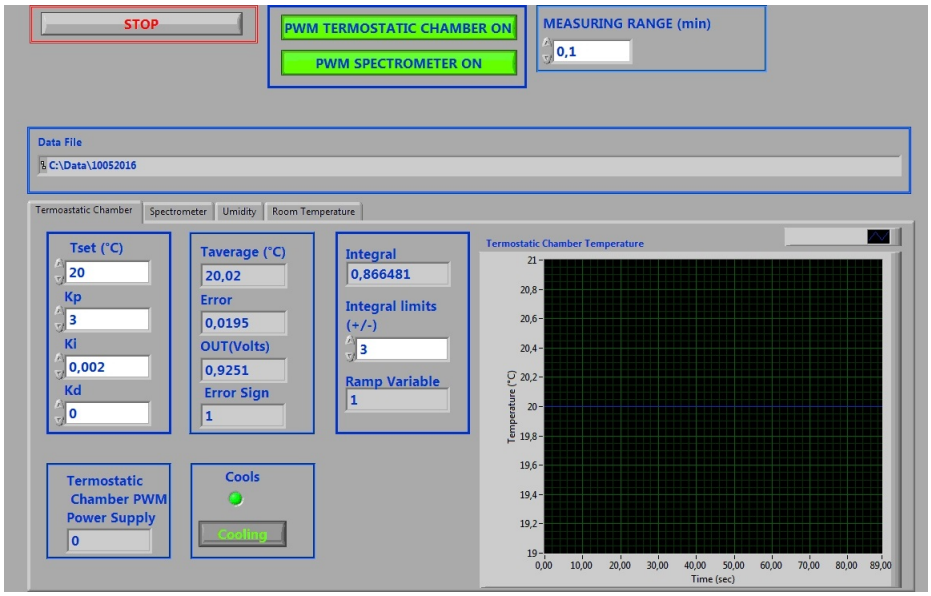

Figure B.1.11: Front Panel

Just a brief comment about the organization of the front panel. As it can be seen in figure B.1.11, the user interface is divided in two principal parts: the upper part is dedicated to the commands and visualization of the information mainly used during the run-time. While the lower part is subdivided in four selectable panel which contain information and settings about the two temperature control system (storage sample chamber and spectrometer) and the two measured variables (humidity and room temperature).

Appendix C

Temperature Hardware Board

Two identical hardware board have been realized for adequate control of the Peltier cells current. This solution was necessary both to use a PWM control to reduce dissipation problems in the MOS-FET and to not generate the PWM signal by the LAbVIEW software, already employed in several other elaborations. In figure is shown the wiring diagram of the temperature hardware board.

In the upper left part of the diagram it can be seen the 17V power supply generated by one of the TTi EL302RT power supply used in the system. This voltage is then reduced to 5V by a integrated stabilizer LM7805 which, in turn, supplies the microcontroller PIC16F876A and the integrated driver Tc4469. The microcontroller has a clock frequency of 4 MHz, produced by a quartz oscillator and filtered by the ceramic capacitors C6 and C7. At pin 2there is the analog voltage input produced by the PIC6025 after the PID elaboration, this voltage, as previously said in B.1, has to remain within the range 0 to 4.9V. The program of the PIC16F876A reads this voltage and proportionally transforms it in a PWM 1kHz signal. This one is generated by a microcontroller internal hardware module, and then sends to the pin output 11. To this pin is linked a low pass filter, formed by the resistor R3 and the capacitor C9, with a cutoff frequency of about 1MHz that helps to eliminate from the signal the highest frequencies(the R4 is a pull-down resistance which serves as mass reference for the TE4469). In this fashion the "cleaned signal" is read by the pin 1 of the TE4469, integrated driver able to drive MOS-FET with really fast voltage fronts and related power currents. At pin 14 the signal comes out from the driver and passes through the R7 resistor to arrive at the gate of the MOS-FET IRLI3705N, a HEXFET able to drive currents up to 52A with a static static drain-to-source on-resistance about 0.01Ω. The R7 resistor of 150Ω has been inserted to prevent too fast rising edges which could produce electromagnetic interference both to the circuit itself and to other eventual electronic devices present nearby. The R8 is a power resistor of 3W and is used as a shunt to control the current which goes through the Peltirer cells. Having a value of 1Ω, R8 yield 1V for each Ampere of current that flows through. This resistor is linked with the microcontroller pin 3 through a low pass filter, having a cutoff frequency of few Hz, which transform the voltage peaks

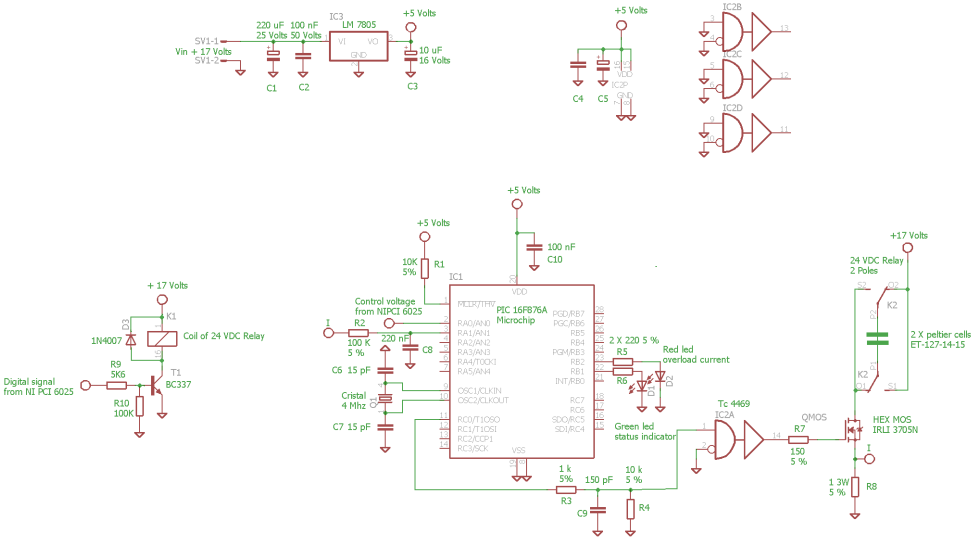

Figure C.0.1: Wiring diagram temperature hardware board

in a continuous value. The PIC16F876A program is able to read this value and to obtain the relative current, in order to monitor eventual over-current. If the current exceeds 2.5A for a period of time longer than two seconds, then the microcontroller stops the current flow to the cells and changes its state from normal to overload, switching on the red LED D2. D1 is a status LED that under normal operating conditions flashes with a frequency of 5Hz. The Peltier cells have a max power of 55.6W with a max voltage of 15.7V and a max current of 6A. For practicality it has been decided to drive them in series in order to use only one MOS-FET. The max voltage which each cell undergoes is about 8V, while the max current can reach 2.5A . As a consequence in any situation the system will always be below the maximum power limit. As it can be seen from the wiring diagram, the Peltier cells are linked to the 17V power supply and to the MOS-FET drain by mean of a two contact relay. Activating the relay the contacts are switched and the current through the cells changes its verse flow, inverting the system cooling/heating cycle. The relay activation is provided by a digital TTL signal coming from NI 6025. When this signal is high it s voltage value is about 3,5V, the transistor base-emitter junction is then directly polarized and through the R9 resistor flows a base current of about 500μA. The T1 (BC337) has a hfe_{min} of 100, as a consequence the collector current will be about 50mA, more than enough for excite the relay coil. The D3 diode, mounted antiparallel to the coil, is useful to discharge the energy accumulated by the inductance at the moment of its de-excitation. The 100kΩ resistor R10 assure the transistor switch off when the TTL signal is down. In the wiring diagram is presented the relay de-excited condition, at which the Peltier cells are in the cooling operational mode (positive current). On the contrary, in

excited relay condition a negative current flows through the cells, which will be in heating operational mode.

Appendix D

Temperature & Humidity Probes

The system exploits three integrated temperature sensors LM35 by Texas Instruments. These devices offer an accuracy of ± 0.4°C for all the functional range which goes from -55 to 150°C, but within the range of temperature chosen for the present work, from 5 to 50°C, the typical error is reduced to a maximal one of ± 0.1°C, more than enough for the purposes of this elaboration.

An output of 10mV/°C is produced by these probes, so in relation to the temperature range given above the relative interval of tension, from 50mV to 500mV, is obtained. At low temperature the voltage values are quite low and they can be altered by noise or electromagnetic interference. To prevent these problems an instrumentation amplifier has been used to multiply per ten times the probe output signal. The chosen amplifier is a INA128 by Burr Brown, which has a high CMRR (common-mode rejection ratio) of 120dB,and also a low offset and a drift offset of 0.5μV/°C, therefore it doesn't introduce temperature variation errors. Furthermore at the amplifier output a low-pass filter has been implemented with a cutoff frequency of 0.5Hz, in order to cut interference eventually produced by the 50Hz supply network.

As shown in figure D.0.1, at the pin 3 of the INA128 the output of the temperature robe comes in (10mV/°C) and at the pin 6 cames out amplified (100mV/°C), the resistance of R1 has been calculated by mean of the formula given by the constructor $A = 1 + (\frac{50k\Omega}{R1})$ to obtain the desired amplification. The R2 resistor together with the capacitor C5 is a low pass filter already described. It can be seen the double power supply($\pm$10V) typical for an instrumentation amplifier and the single one (+10V) for the temperature sensor.

For the humidity sensor, Honeywell HIH-5030, a circuit suggested by the constructor has been used as shown in the right part of the wiring diagram shown in figure D.0.2. The sensor is supplied with 3.3V, which is the typical operating voltage adopted by the constructor to realize the main number of characteristic curves inserted in the technical data-sheet. A voltage

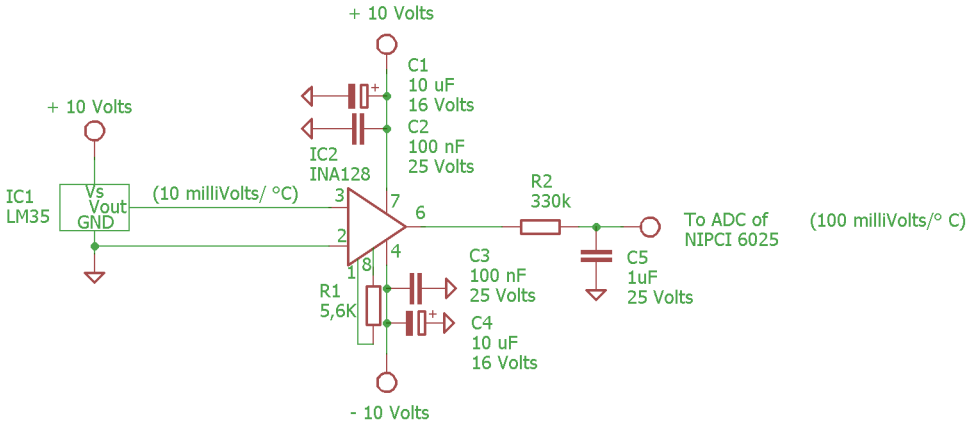

Figure D.0.1: Probe temperature amplifier wiring diagram.

regulator LM317 by National Semiconductor able to regulate stabilized voltage from 1.2V up to 40V, has been used to produce the 3.3V. The resistors R1, R2 and R3 have been calculated by means of the constructor's formula $V_{out} = V_{ref}\left(1 + \frac{R2+R3}{R1}\right) + I_{adj}\,(R2 + R3)$, where $V_{ref} = 1.25V$ and I_{adj} is the output current form the adj pin which value is $50\mu A$. R4 has been chosen in order to give a minimal stability at the sensor output signal.

The sensor voltage output is then corrected by an equation which take into account its behavior as a function of the power supply. the relative humidity is obtained by the equation $HR = V_{supply}\,(0.00636 \cdot V_{out,sensor} + 0.1515)$. This circuit allows to measure the relative humidity in a range from 11% up to 89% with a max accuracy of $\pm 3\%$.

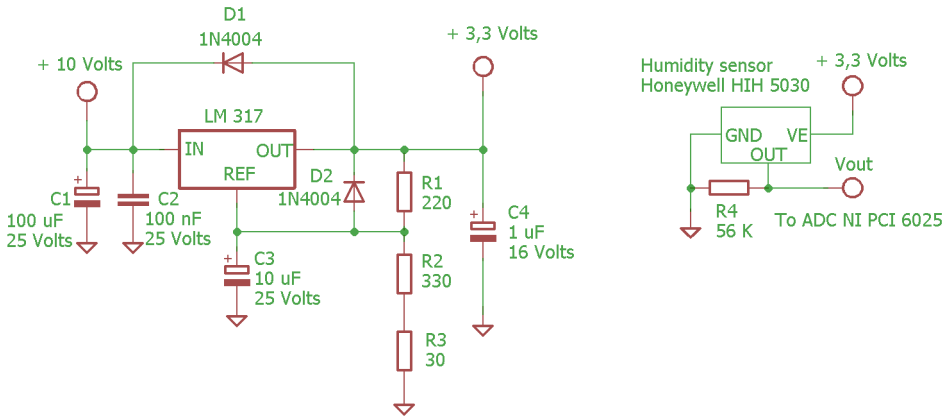

Figure D.0.2: Probe humidity wiring diagram.

Appendix E

Symmetry of single-walled carbon nanotubes

Symmetry Group Basic Concept

In solids, according to one-electron Hamiltonian for electron energy band, the Schrödinger's equation can be written as

$$\mathcal{H}\psi(\boldsymbol{r}) = \left[-\frac{\hbar}{2m}\nabla^2 + V(\boldsymbol{r})\right]\psi(\boldsymbol{r}) = E\psi(\boldsymbol{r}) \tag{E.0.1}$$

where $V(\boldsymbol{r})$ is a *periodic potential*. The symmetry group that leave invariant the one-electron Hamiltonian and the periodic potential in equation E.0.1 , or equivalently which carry the crystal into itself, is the *space group of the crystal lattice*, which consist of both *translational* and *point group symmetry operations*[1]. Both these symmetry operations leave $\mathcal{H}$ invariant, and consequently all the operators related to these symmetry operations will commute with $\mathcal{H}$, providing quantum numbers for label energy eigenvalues and eigenfunctions.

Space group operators are usually denoted by mean of the common notation$(R_\alpha|\boldsymbol{\tau})$, where R_α denotes point group operations such as rotation, reflection, improper rotation and inversion, while $\boldsymbol{\tau}$ denotes translation operations. In particular $(I|\mathbf{0})$identify the identity element, $(R_\alpha|\mathbf{0})$ refers to a pure point group operation and $(I|\boldsymbol{\tau})$ represent a pure translation. The operator $(R_\alpha|\boldsymbol{\tau})$ act on a general vector $\boldsymbol{r}$ as

$(R_\alpha|\boldsymbol{\tau})\,\boldsymbol{r} = R_\alpha\boldsymbol{r} + \boldsymbol{\tau} = \boldsymbol{r}'$, the composition low between to element is $(R_\beta|\boldsymbol{\tau}')\,(R_\alpha|\boldsymbol{\tau})\,\boldsymbol{r} = (R_\beta|\boldsymbol{\tau}')\,(R_\alpha\boldsymbol{r}+\boldsymbol{\tau}) = R_\beta R_\alpha\boldsymbol{r}+R_\beta\boldsymbol{\tau}+\boldsymbol{\tau}' = (R_\alpha R_\beta|R_\beta\boldsymbol{\tau}+\boldsymbol{\tau}')\,\boldsymbol{r}$ and the inverse element is $(R_\alpha|\boldsymbol{\tau})^{-1} = \left(R_\alpha^{-1}|-R_\alpha^{-1}\boldsymbol{\tau}\right)$. Pure point group operation and pure translation are only special cases of space group operations, in general there are compound symmetry operation that combine these two types

[1] Point groups are groups of geometric symmetries that exhibit a point that never moves under the application of all their symmetry operators, in contrast to the space group [95].

of operations. In particular there are two types of compound symmetry operations which are called *glide planes* and *screw axis.* A *glide plane* consist of a translation parallel to a given plane, followed by a reflection in that plane. A *screw axis* is a translation along an axis about which a rotation is simultaneously occurring. A n-fold screw axis has a translation of $\frac{p\boldsymbol{\tau}_0}{n}$ where $\boldsymbol{\tau}_0$is a unit cell translation of the translation group, p is an integer $p = 1, 2, ..., n$ and the rotation is $\frac{2\pi p}{n}$.

All the elements of the form $(I|\boldsymbol{\tau})$constitute the translation group $\mathbf{T}$, which is an invariant subgroup of the space group. Symmetry elements of $\mathbf{T}$ are defined by the translation vectors $\boldsymbol{R}_n$which leaves the Bravais lattice invariant $\boldsymbol{R}_n = \sum_i n_i \boldsymbol{a}_i$, and $\boldsymbol{a}_i$ is the primitive vector of the Bravais lattice, *i.e.,* $\mathbf{T}$ defines the Bravais lattice [95].

Schoenflies and Hermann–Mauguin Symmetry Notation

There are two point group notations that are used for the symmetry operations in books and journals, one is the *Schoenflies symmetry notation* and the other is the *Hermann–Mauguin notation* that is used by the crystallography community. For the Schoenflies the following notation is commonly used:

- E (or I) is the identity
- C_n is a rotation through $2\pi/n$. For example C_2 is a rotation of 180°, C_3 is a rotation of 120°, while C_6^2 represents a rotation of 60° followed by another rotation of 60° about the same axis so that $C_6^2 = C_3$. It can be shown that in a Bravais lattice n in C_n can only assume values of n = 1, 2, 3, 4, and 6.
- σ is a reflection in a plane.
- σ_h is a reflection in a "horizontal" plane. The reflection plane here is perpendicular to the axis of highest rotational symmetry.
- σ_v is reflection in a "vertical" plane. The reflection plane here contains the axis of highest rotational symmetry.
- σ_d is the reflection in a diagonal plane. The reflection plane here is a vertical plane which bisects the angle between the twofold axes $\perp$ to the principal symmetry axis. σ_d is also called a dihedral plane.
- i (or $\mathcal{I}$) is the inversion which takes $\begin{cases} x \to & -x \\ y \to & -y \\ z \to & -z \end{cases}$.
- S_n is the improper rotation through $2\pi/n$, which consists of a rotation by $2\pi/n$ followed by a reflection in a horizontal plane. Alternatively, we can define S_n as a rotation by $4\pi/n$ followed by the inversion.

- iC_n compound rotation–inversion, which consists of a rotation followed by an inversion[95].

An important distinction has to be made about *elements* and *symmetry operations*, because although strictly linked[2], they are conceptually different. The *symmetry operation* is a transformation that maps a configuration of an object in a equivalent one, indistinguishable from the original, but not necessarily identical, or in the same way one can say that the symmetry operation is a movement of an abject such that, after the movement has been carried out, every point of the body is coincident with an another equivalent point, or the same point, of the object in its original orientation. A *symmetry element* is a geometric entity, *i.e.,* planes, axes, points, within the object, respect to which one or more symmetry operation can be performed [96]. But in literature it is customary to denote both symmetry operation and symmetry element by using the same symbol. For example, C_n is used to refer both to the axis of a n-fold rotation and to the symmetry operation C_n itself. In the same way a σ plane is the plane about which is performed a reflection σ.

There are 32 common point groups for crystallographic systems (n = 1, 2, 3, 4, 6), and the character tables for these 32 point groups are given in many standard group theory texts. Groups $\boldsymbol{C}_1$, $\boldsymbol{C}_2$, . . ., $\boldsymbol{C}_6$ are cyclic groups that have only n-fold rotations about a simple symmetry axis C_n. In addition to the n-fold axes, $\boldsymbol{C}_{nv}$ groups have a vertical reflection planes σ_v. Groups $\boldsymbol{C}_{nh}$ have the n-fold axes, a horizontal reflection planes σ_h and include each operation C_n together with the compound operations $C_n\sigma_h$. Groups $\boldsymbol{S}_2$, $\boldsymbol{S}_4$, and $\boldsymbol{S}_6$ are mainly constituted by compound operations. The dihedral groups $\boldsymbol{D}_n$ have non-equivalent symmetry axes in perpendicular planes . When $n = 4$, $\boldsymbol{D}_n$is the group of the operations of a square, *i.e.,* $\boldsymbol{D}_4$, which has in addition to the principal fourfold axes, two sets of non-equivalent twofold axes. Sometimes is used the notation C_2' to indicate that these twofold axes are in a different plane. Groups like $\boldsymbol{D}_{2h}$,$\boldsymbol{D}_{3h}$, etc. are obtained when non-equivalent axes are combined with mirror planes. There are five cubic groups T , O, T_d, T_h, and O_h. These groups have no principal axis but instead have four threefold axes [95].

The second notation for symmetry operations and groups is known as the Hermann–Mauguin (H-M) or international notation, and is usually adopted in crystallography textbooks and various materials science journals. A correspondence between the Schoenflies and H-M notations is shown in table E.1 for rotations and mirror planes. The symbol $\bar{n}$ in the H-M notation refers to iC_n, which is equivalent to a rotation of $2\pi/n$ followed by or preceded by an inversion. The symmetry axes parallel to and the symmetry planes perpendicular to each of the "principal" directions in the crystal are named in order. So when a string is written in this notation, the first symbol denotes the principal axis or plane. The second symbol denotes an axis, or plane, perpendicular to this axis

[2]Symmetry element and operation are so closely interrelated because the latter can be defined only respect to the former and at the same time the fact that the element exists can be only demonstrated by showing the existence of the appropriate symmetry operation [96].

Table E.1: Correspondance between Schoenflies and Hermann-Mauguin notations. Taken from [95].

	Schoenflies	Hermann-Mauguin
rotation	C_n	n
rotation–inversion	iC_n	$\bar{n}$
mirror plane	σ	m
horizontal reflection plane $\perp$ to n-fold axes	σ_h	n/m
n-fold axes in vertical reflection plane	σ_v	nm
two non-equivalent vertical reflection planes	$\sigma_{v'}$	nmm

Table E.2: Comparison of notation for proper and improper rotations in the Schoenflies and International systems. Taken from [95].

proper rotations		improper rotations	
Hermann-Mauguin	Schoenflies	Hermann-Mauguin	Schoenflies
1	C_1	$\bar{1}$	S_2
2	C_2	$\bar{2} = m$	σ
3	C_3	$\bar{3}$	S_6^{-1}
3_2	$C_3^2 = C_3^{-1}$	$\bar{3}_2$	S_6
4	C_4	$\bar{4}$	S_4^{-1}
4_3	$C_4^3 = C_4^{-1}$	$\bar{4}_3$	S_4
5	C_5	$\bar{5}$	S_{10}^{-1}
5_4	$C_5^4 = C_5^{-1}$	$\bar{5}_4$	S_{10}
6	C_1	$\bar{6}$	S_3^{-1}
6_5	$C_6^5 = C_6^{-1}$	$\bar{6}_5$	S_3

[3]. The third symbol denotes an axis, or plane, that is $\perp$ to the first axis and at an angle of π/n with respect to the second axis. For example the string 422 means that there is a fourfold major symmetry axis,*i.e.,* aC_4 axis, and perpendicular to this axis there are two inequivalent sets of twofold axes C_2' and C_2''. When there is both an axis parallel to a given direction and a plane normal to the same direction, these are indicated as a fraction. Therefore $6/m$ refers to a sixfold rotation axis standing perpendicular to a plane of symmetry. If there are several inequivalent horizontal mirror planes like $2/m$, $2/m$, $2/m$, an abbreviated notation mmm is sometimes used. The notation $4mm$ denotes a C_4 axis and two sets of vertical mirror planes, one, indicated as $2\sigma_v$, set through the axes C_4 and the other, denoted by the dihedral vertical mirror planes $2\sigma_d$, set through the bisectors of the $2\sigma_v$ planes. Table E.2 can be used to relate the two notations for rotations and improper rotations.

[3]The cubic groups is an exception, in this particular case the second symbol refers to a <111> axis

Line Group

Line group describes the symmetry of a system exhibiting translational periodicity in one dimension, with periodicity being not restricted to the translational one. Introducing the nanotubes structure, the large longitudinal-lateral aspect ratio has been underlined, this outlines the direction along which basic constituents, *monomers*, are repeated regularly. Therefore there are two different ways by which their symmetries, being defined as the geometrical transformations leaving the compound unchanged, arise: as periodicity of the regular arrangement of monomers and as an intrinsic symmetry of a single monomer. However, the *symmetries of the total compound* are combined from the symmetries of the arrangement and the intrinsic symmetries of monomers only if the latter (intrinsic symmetries) leave simultaneously all the monomers unchanged, i.e., if they are compatible with the periodical arrangement.

Line group generally involve a *generalized translational group* $\boldsymbol{Z}$, where by "generalized" is meant that $\boldsymbol{Z}$ denotes an infinite cyclic group composed of general translational operation along the line axis (denoted as z-axis by convention) that may include screw axis and glide plane, and *axial point group* $\boldsymbol{P}$ giving the internal symmetry [94].

A general element of $\boldsymbol{Z}$ can be written as $Z = (X|\boldsymbol{f})$, where $\boldsymbol{f}$ indicate a translation by $\boldsymbol{f} = f\boldsymbol{e}_z$ along the z-axis, while X is the orthogonal part of the generator Z that leave z-axis invariant. Otherwise, after applying Z the system would not be directed along z-axis, and Z could not be a symmetry. Therefore X can be either a rotation around z-axis or a reflection in the vertical mirror plane (composition of these two is a mirror plane), i.e., the possibilities are $X = C_Q$ (rotation for $\varphi = 2\pi/Q$ around z-axis) and $X = \sigma_v$ (vertical mirror plane). The arrangement generated by the above defined $Z = (X|\boldsymbol{f})$ is *commensurate*, i.e., has translational periodicity , if $\boldsymbol{Z}$ has a cyclic subgroup $\boldsymbol{T}$ generated by $(I|\boldsymbol{A})$ of the pure translations, where the *translational period* $\boldsymbol{A}$ is the minimal among the pure translations in $\boldsymbol{Z}$. For commensurate systems is possible to introduce the so called *elementary cell*, which generates the system by mean of the *only translations*. Being $(I|\boldsymbol{A})$ an element of $\boldsymbol{Z}$, this minimal translation is obtained as a successive application of Z, i.e., there is a natural number q such that $(X|\boldsymbol{f})^q = (X^q|q\boldsymbol{f}) = (I|\boldsymbol{A})$. This gives the condition $X^q = I$. For glide planes this is always automatically satisfied for $q = 2\,(\sigma^2 v = I)$. As for the screw-axes, the condition becomes $Q = q/r$, where r is a natural and not greater than q (as $Q \geq 1$). So, translational periodicity appears only when Q is rational, i.e., when $\varphi = 2\pi r/q$ is rational multiple of 2π . For convenience r and q are assumed co-primes, $GCD(q, r) = 1$. In particular, if $q = 1\,(i.e., \varphi = 0)$ screw-axis is pure translational group, formally taking $\varphi = 2\pi$, with $Q = q = r = 1$. The obtained period[4] $\boldsymbol{A}$ is multiple of the fractional translation of the generator, $\boldsymbol{A} = q\boldsymbol{f}$, meaning that the elementary cell contains q monomers. Thus the helical generator in this case is $(C_q^r|\boldsymbol{A}/q)$ [94].

There are two different types of generalized translation group:

[4]Capital $\boldsymbol{A}$ denotes the translational period of the commensurate helical group, only. The period of the total group is denoted as $\boldsymbol{a}$.

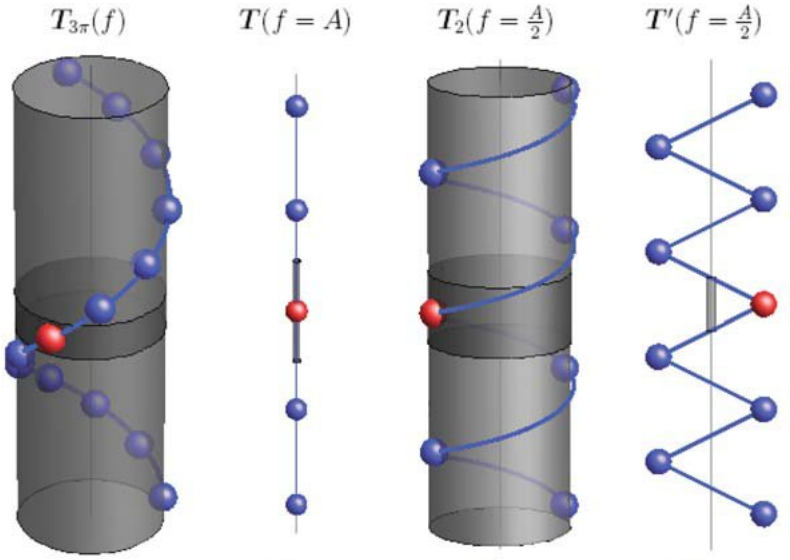

Figure E.0.1: Generalized translational groups (from left to right): incommensurate (and chiral) helical axis, translational group, zigzag group, glide plane; fractional translations are shown by dark gray cylinders on which the initial (red) atoms sit. Taken from [94].

1. *screw-axis group*, $\boldsymbol{T}_Q(f)$ generated by $(C_Q|\boldsymbol{f})$. In the special cases when $Q = q/r$, with positive co-prime integers $r \leq q$, screw-axis $\boldsymbol{T}^r_q(\boldsymbol{A}/q)$ generated by $(C^r_q|\boldsymbol{A}/q)$ is commensurate, with index q subgroup of pure translations with period $\boldsymbol{A} = q\boldsymbol{f}$; particularly, for $q = 1$ and $q = 2$, screw-axis degenerates to the translational and zigzag group, respectively.

2. *glide plane group*, $\boldsymbol{T'}(\boldsymbol{A}/2)$, generated by $(\sigma_v|\boldsymbol{f})$, which has a halving subgroup[5] of pure translations with period $A = 2f$ [94].

The minimal part of the system sufficient to completely generate it only by the action of generalized translations Z is called *monomer,* which in turn possesses its own symmetry . Knowing $\boldsymbol{Z}$ and applying Z successively t times on an initial monomer denoted by M_0 , i.e., acting by Z^t on each atom in M_0 , another monomer is obtained, which is naturally labeled by M_t . This fact shows that complete information on the entire system is given by the group of generalized translations and chemical and geometrical structure of a single monomer. In other words, physical properties of the system are determined by properties of a single monomer and symmetry of the arrangement.

The monomer symmetry transformations do not include translations, so their form are of the type $X = (X|0)$. Such transformations are gathered into *point*

[5]A halving group of a group G is a subgroup H of index two. H is always a normal subgroup of G, if g is an element of G that is not contained in H; the decomposition in right and left coset of G yield $G = H + gH = H + Hg$

Table E.3: For each axial point group $\boldsymbol{P}_n$ (n = 1, 2, . . .) in each row are reported the order of the group $|\boldsymbol{P}_n|$, the factorization F , generators g, positive subgroup $\boldsymbol{P}_n^+$ (for positive groups $\boldsymbol{P}_n^+ = \boldsymbol{P}_n$), and the coset representative(s) $p_i^{(F)}$ of $\boldsymbol{C}_n$ are given. In the last two rows the extension $\boldsymbol{P}_n^{\mathcal{I}} = \boldsymbol{P}_n + \mathcal{I}\boldsymbol{P}_n$ of $\boldsymbol{P}_n$ by spatial inversion $\mathcal{I}$ is given for n odd and even. Take from[94].

$\boldsymbol{P}_n$	$\boldsymbol{C}_n$	$\boldsymbol{S}_{2n}$	$\boldsymbol{C}_{nh}$	$\boldsymbol{D}_n$	$\boldsymbol{C}_{nv}$	$\boldsymbol{D}_{nd}$	$\boldsymbol{D}_{nh}$
$\lvert\boldsymbol{P}_n\rvert$	n	$2n$	$2n$	$2n$	$2n$	$4n$	$4n$
F	$\boldsymbol{C}_n$	$\boldsymbol{S}_{2n}$	$\boldsymbol{C}_n\boldsymbol{C}_{1h}$	$\boldsymbol{C}_n\boldsymbol{D}_1$	$\boldsymbol{C}_n\boldsymbol{C}_{1v}$	$\boldsymbol{S}_{2n}\boldsymbol{C}_{1v}$	$\boldsymbol{D}_n\boldsymbol{C}_{1v}$
g	C_n	$C_{2n}\sigma_h$	C_n , σ_h	C_n , U	C_n , σ_v	$C_{2n}\sigma_h$, U_d	C_n, U , σ_v
$\boldsymbol{P}_n^+$	$\boldsymbol{C}_n$	$\boldsymbol{C}_n$	$\boldsymbol{C}_n$	$\boldsymbol{C}_n$	$\boldsymbol{C}_{nv}$	$\boldsymbol{C}_{nv}$	$\boldsymbol{C}_{nv}$
$p_i^{(F)}$		$C_{2n}\sigma_h$	σ_h	U	σ_v	σ_v, $C_{2n}\sigma_h$, U_d	σ_v, σ_h , U
$\boldsymbol{P}_{n=2i+1}^{\mathcal{I}}$	$\boldsymbol{S}_{2n}$	$\boldsymbol{S}_{2n}$	$\boldsymbol{C}_{2nh}$	$\boldsymbol{D}_{nd}$	$\boldsymbol{D}_{nd}$	$\boldsymbol{D}_{nd}$	$\boldsymbol{D}_{2nh}$
$\boldsymbol{P}_{n=2i}^{\mathcal{I}}$	$\boldsymbol{C}_{nh}$	$\boldsymbol{C}_{2nh}$	$\boldsymbol{C}_{nh}$	$\boldsymbol{D}_{nh}$	$\boldsymbol{D}_{nh}$	$\boldsymbol{D}_{2nh}$	$\boldsymbol{D}_{nh}$

groups. Let $\boldsymbol{P}_M$ be the symmetry group of an arbitrary monomer M_0. Any transformation P from $\boldsymbol{P}_M$ leaves M_0 invariant. However, to be a symmetry of the whole system, this transformation in addition has to map any monomer M_t into itself or into another monomer $M_{t'}$. Generally, this cannot be fulfilled unless P leaves z-axis invariant. Hence, only the maximal subgroup $\boldsymbol{P}$ of $\boldsymbol{P}_M$ leaving z-axis invariant may contribute to the symmetry of the system. The maximal orthogonal group which preserves the z-axis is the $\boldsymbol{D}_{\infty h}$, so the point group $\boldsymbol{P} = \boldsymbol{P}_M \bigcap \boldsymbol{D}_{\infty h}$ is the maximal subgroup of the monomer symmetry group relevant for the system.

The orthogonal transformations leaving z-axis invariant are:

- rotations C_n^s for angle $\varphi = 2\pi s/n$ around z-axis,
- rotations U for π around an axis perpendicular onto z-axis,
- horizontal and vertical mirror planes (σ_h and σ_v, and their combinations, such as roto-reflectional plane $S_{2n} = C_{2n}\sigma_h$).

With such operations it is possible to construct seven infinite families of the axial point groups : $\boldsymbol{C}_n$, $\boldsymbol{S}_{2n}$, $\boldsymbol{C}_{nh}$, $\boldsymbol{D}_n$,$\boldsymbol{C}_{nv}$, $\boldsymbol{D}_{nd}$ and $\boldsymbol{D}_{nh}$. The groups within a family differ by the order $n = 1, 2, ...$ of the principal axis. In fact, each axial point group has a subgroup $\boldsymbol{C}_n$ of index $n_F = |\boldsymbol{P}_n|/n$ ($\boldsymbol{P}_n$ is the axial line group and $|\boldsymbol{P}_n|$ is its order), with $n_F = 1$ for family 1, $n_F = 2$ for families 2, 3, 4, and 5, and $n_F = 4$ for families 6 and 7 .

The decomposition onto cosets is given by the relation: $\boldsymbol{P}_n = \sum_{i=1}^{n_F} p_i^{(F)}\boldsymbol{C}_n$ with $p_{i=1}^{(F)} = e$, and the remaining coset representatives is listed in E.3.

The direction of z-axis may be reversed by the transformations of these groups, for this motive such elements are called *negative* in contraposition to the *positive* elements which preserve the axis direction. The product of negative elements gives a positive one, therefore set of positive elements is either the whole group (positive group $\boldsymbol{P}_n^+$) or a halving subgroup (which is also axial

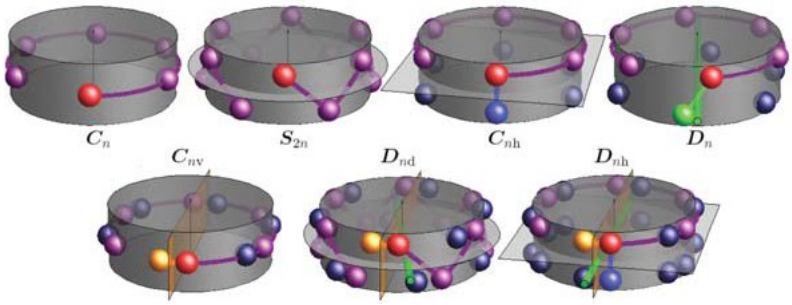

Figure E.0.2: Axial point groups: onethe groups with $n = 6$ from all the families are presented by the points obtained from the initial one (red). Those obtained by the successive actionone of the generators (according to E.3) are in special colors and connected by the lines: purple, blue, green, and orange correspond to C_n^s or $(C_{2n}\sigma_h)^s$, σ_h , U and σ_v ; accordingly, vertical mirror plane and U-axis are orange and green. Gray square and circle are horizontal mirror and roto-reflectional planes. Taken from [94]

point group as $\boldsymbol{C}_n$ is positive) when the group is called negative $P_n^- = P_n^+ + p^- P_n^+$.

The first three families, $\boldsymbol{C}_n$, $\boldsymbol{S}_{2n}$, and $\boldsymbol{C}_{nh}$, are the abelian groups, and in particular the first two are cyclic groups. All other families are factorized into products of cyclic groups [94].

Finally the line group $\boldsymbol{L}$ is formed by taking all pairs $\boldsymbol{P}$ and$\boldsymbol{Z}$ giving a group $\boldsymbol{L} = \boldsymbol{ZP}$, because all the element of $\boldsymbol{Z}$ have non zero translational part (except for the identity), while no point group element on $\boldsymbol{P}$ have translations. The elements of $\boldsymbol{L}$ are the products $l = Z^t P$ of the generalized translations Z^t from $\boldsymbol{Z}$ (all elements of $\boldsymbol{Z}$ are powers of the generator Z) and intrinsic symmetries P from $\boldsymbol{P}$. In the construction of the line groups is fundamental to examine the compatibility of the intrinsic monomer symmetry (axial point group) and of the symmetry of the arrangement (group of generalized translations). To do so one must check if the set of the elements $l = Z^t P$ has a group structure; then $\boldsymbol{P}$ and$\boldsymbol{Z}$ are subgroups of this group (for fixed $t = 0$ and $P = I$, respectively). The product of two subgroups is a group if and only if these subgroups commute[6], i.e., $\boldsymbol{L} = \boldsymbol{ZP}$ is group if and only if $\boldsymbol{PZ} = \boldsymbol{ZP}$. As the intersection $\boldsymbol{P} \cap \boldsymbol{Z}$ contains only the identity element (point operations are without translational part, and the identity Z^0 is the only such element in $\boldsymbol{Z}$), the product is a *weak direct* [7] one . In some cases one or both subgroups are invariant, and this

[6]This does not mean that the elements of $\boldsymbol{P}$ and$\boldsymbol{Z}$ commute, but only that for each P and t there is a choice of P' and t' such that $PZ^t = Z^{t'}P'$.

[7]A group G is said to be the weak direct product of its subgroups H and K when (i) the identity is the only element in the intersection of H and K (ii) each element af G is the product of one element of h with one element of K. Semi-direct and direct products are special cases of the weak-direct product. When H and K are invariant subgroups, the result is a direct product. When only H is an invariant subgroup, the result is a semidirect product [95].

product becomes semi-direct ($\wedge$, with the first factor invariant) and direct ($\otimes$), respectively.

All helical operations commute with pure rotations around z-axis, therefore any group $\boldsymbol{C}_n$ is compatible with any $\boldsymbol{T}_Q(f)$. Their products $\boldsymbol{T}_Q(f)\boldsymbol{C}_n$ comprise the first family line groups, the simplest line groups which are subgroups of all the other line groups. Quite analogously, all $\boldsymbol{T}_Q(f)$ are compatible with the groups $\boldsymbol{D}_n$. Others axial point groups are compatible only with special helical groups $\boldsymbol{T}(f = a)$ and $\boldsymbol{T}^1_{2n}(f = a/2)$, where n is the order of the principle axis of the point group.

On the other hand, glide plane group is compatible with all the axial point groups. The only requirement when the point group contains mirror planes or U-axes is that glide plane either coincides with them or bisects them, and different groups are obtained in these two cases. As glide plane is commensurate, as well are all the resulting groups.

In this way all the products of the point factor $\boldsymbol{P}$ and generalized translation group $\boldsymbol{Z}$ are obtained. Although with different factors, some of these products are equal, giving different factorization of the same line group. Thirteen infinite families of the line groups in the factorized form are obtained, each one includes all groups (with various parameters Q, f , n) with fixed type of $\boldsymbol{Z}$ and $\boldsymbol{P}$. The incommensurate line groups are either from the first or from the fifth family (commensurate ones from these families are singled out by the condition $Q = q/r$), while in all other families generalized translational group is either glide plane, pure translational group $\boldsymbol{T}$, or zigzag group $\boldsymbol{T}^1_{2n}$. Among (infinitely many) line groups there are 75 *rod groups, i.e.,* line groups from all families satisfying crystallographic conditions, with the order q of the principle axis of rotation of the isogonal group taking crystallographic values $q = 1$, 2, 3, 4,6 or $q = 1$, 2, 3 for the line groups with roto-reflections (i.e., for the families 2, 9, and 10).

Along this introduction of space and line groups, different types of descriptors, that use only a portion of the whole system and a peculiar symmetry group, have been introduced. The monomer denote the minimal part of the system sufficient to generate the whole system by the action of generalized translations $\boldsymbol{Z}$ only. The elementary cell generates the system by the translations only for commensurate systems. Finally another one has to be introduced yet, the *symcell* or *symmetry cell,* which is a part of the monomer that generate the system by mean of the full symmetry . None of these parts of the system is uniquely defined, but the number of atoms it contains is. Further, as in commensurate case translational group is a subgroup of $\boldsymbol{Z}$, elementary cell contains $|\boldsymbol{Z}|/|\boldsymbol{T}|$ monomers[94].

SWCNTs Symmetry Operation

As seen in subsection 2.1 in chapter 2, the standard approach for obtaining the descriptors that characterize the tubes is to start from the ones of the graphene lattice; in the same way in order to find the symmetry groups of carbon nanotubes a suitable way is to consider the symmetry operations of graphene that are preserved even though the graphene sheet is rolled up into a

cylinder [9].

The translations by multiples of a of the graphene sheet parallel to the unit cell nanotube vector $\boldsymbol{a}$ form a subgroup $\boldsymbol{T}$ containing the *pure traslations parallel to the nanotube z-axis*. Translations parallel to the circumferential vector $\boldsymbol{c}$ become pure rotation of the nanotube around its axis. Recalling that $n = GCD(n_1, n_2)$ lattice points fall on the chiral vector $\boldsymbol{c}$, the nanotube can be rotated by multiples of $2\pi/n$. Thus the n *rotations around the z-axis*, labeled by C_n^s (with $s = 0, 1, 2, ..., n-1$, and $C_n^n \equiv I$), are symmetry elements that form a subgroup $\boldsymbol{C}_n$ of the full symmetry group.

Combinations of translations in the $\boldsymbol{a}$ and $\boldsymbol{c}$ direction form the translations of the graphene sheet along any other direction. Thus, when the graphene sheet is rolled up, they result in translation combined with rotations about the nanotube axis, which goes under the name of *screw axis operations*. The order of these symmetry operations is equal to the number q of graphene lattice points in the nanotube unit cell. They are denoted by $(C_q^w|an/q)^t$with the parameter

$$w = \frac{q}{n}\mathrm{Fr}\left[\frac{n}{q\mathcal{R}}(3 - 2\frac{n_1 - n_2}{n_1}) + \frac{n}{n_1}(\frac{n_1 - n_2}{n})^{\varphi(n_1/n)-1}\right] \tag{E.0.2}$$

where Fr$[x]$ is the fractional part of the rational number x, and $\varphi(n)$ is the Euler function. On the plain graphene sheet, the screw axis operation corresponds to the primitive translation $\frac{w}{q}\boldsymbol{c} + \frac{n}{q}\boldsymbol{a}$. As can be seen from equation 2.1.6, $q \geq 2n$, so the screw axis operation is always present in the nanotube line group. In achiral nanotubes, $q = 2n$ an $w = 1$; thus the screw axis operation consist of a rotation by π/n followed by a translation by $a/2$.

Beside the translations, there are other symmetries for the honeycomb lattice: perpendicular rotational axis through the centers of the hexagons (of order six), through the carbon atoms (of order 3) and through the centers of the edges of the hexagons (of order 2);six vertical mirror planes through the centers of the hexagons (or through the atoms); and two types of glide planes-connecting the midpoints of two adjacent edges, and the midpoints of the next to the nearest-neighboring edges of the hexagons.

Among the six-fold rotations, only those for π remains a symmetry operation of the carbon nanotubes, because they leave invariant the axis of $\boldsymbol{a}$, *i.e.* the axis of the nanotube, on the contrary any other rotation will tilt the z axis and therefore are not symmetry of the tube. These two type of horizontal second order axes, perpendicular to the z axis, are present in both chiral and achiral tubes: With U is denoted the one passing through the center of the deformed nanotube hexagons, and with U' that passing through the midpoints of adjacent atoms.

In order to transform the nanotube to itslef, mirror planes perpendicular to the graphene sheet must either contain the tube axis, vertical mirror plane σ_v, or be perpendicular to it, horizontal mirror plane σ_h. Only in the achiral nanotubes the vertical and horizontal mirror planes, σ_h and σ_v , are present, they contain the centers of the graphene hexagons. In achiral tubes, as can be seen in figure E.0.3, the orizontal and vertical planes through the midpoint

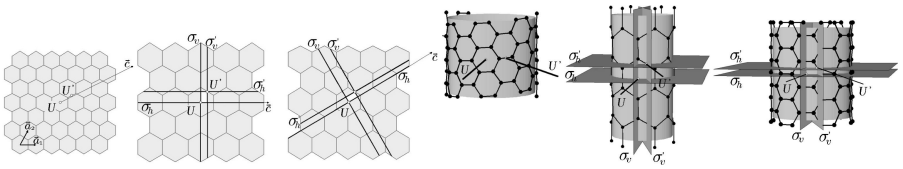

Figure E.0.3: (Left) Symmetries of the honeycomb lattice for the chiral (8,6), zigzag (6,0), and armchair (6,6) tubes. The chiral vectors $\boldsymbol{c}$ ($\bar{c}$ in the picture) are depicted by the arrows. The U and U' axes pass through the circles (perpendicular to the honeycomb). In the zigzag and armchair cases, the bold lines σ_v and σ'_v represent the vertical mirror and glide planes, respectively, of the lattice, orthogonal to $\boldsymbol{c}$; the planes parallel to $\boldsymbol{c}$ are denoted as σ_h and σ'_h ; U is the intersection of the mirror planes, and U' that of the glide planes. (Right) Symmetries of the single-wall nanotubes: (8,6), (6,0), and (6,6). The horizontal rotational axes U and U' are symmetries of all the tubes, while the mirror planes (σ_v and σ_h), the glide plane σ'_v , and the rotoreflectional plane σ'_h are symmetries of the zigzag and armchair tubes only. The line groups are $\boldsymbol{T}^{21}_{148}\boldsymbol{D}_2$ for (8,6), and $\boldsymbol{T}^{1}_{12}\boldsymbol{D}_{6h}$ for the other two tubes. Taken from [94].

between two adjacent atoms form vertical glide planes ($\sigma_{v'}$) and horizontal rotoreflection planes ($\sigma_{h'}$).

In general an element of any carbon nanotube line group is writable as

$$l(t,u,s,p) = (C_q^w|\frac{an}{q})^t C_n^s U^u \sigma_v^p$$

with

$$\begin{aligned} t &= 0, \pm 1, ...; \\ s &= 0, 1, ..., n-1; \\ u &= 0, 1; \\ p &= \begin{cases} 0,1 & achiral \\ 0 & chiral \end{cases} \end{aligned}$$

and w,n,q as give above.

These elements are given by the product of the point group $\boldsymbol{D}_n$ for chiral and $\boldsymbol{D}_{nh}$ for achiral nanotubes and the axial group $\boldsymbol{T}^w_q$, that form the line group $\boldsymbol{L}$:

$$\boldsymbol{L}_{\mathcal{AZ}} = \boldsymbol{T}^1_{2n}\boldsymbol{D}_{nh} = \boldsymbol{L}2n_n/mcm \qquad (armchair\, and\, zig-zag) \tag{E.0.3}$$

and

$$\boldsymbol{L}_{\mathcal{C}} = \boldsymbol{T}^w_q\boldsymbol{D}_n = \boldsymbol{L}q_p22 \qquad (chiral\, tubes). \tag{E.0.4}$$

Here $2\pi w/q$ determines the screw axis of the axial group[9].

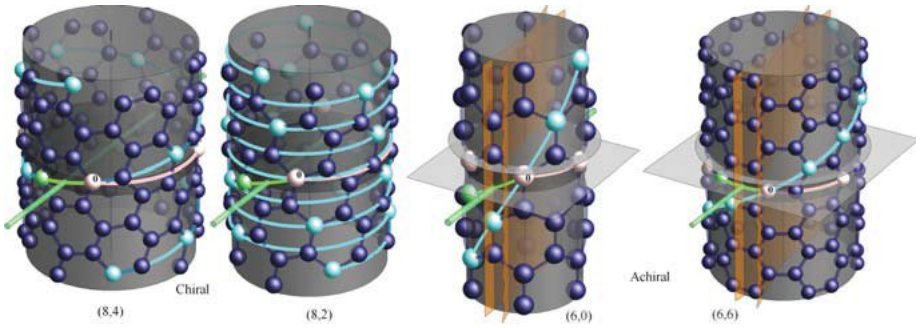

Figure E.0.4: Carbon nanotubes with symmetries. The symmetry groups of the depicted nanotubes (8,4), (8,2), (6,0), and (6,6) are $\boldsymbol{T}^{9}_{56}(0.8\mathring{A})\boldsymbol{D}_4$, $\boldsymbol{T}^{11}_{28}(0.46\mathring{A})\boldsymbol{D}^2$, $\boldsymbol{T}^{1}_{12}(2.14\mathring{A})\boldsymbol{D}_{6h}$, and $\boldsymbol{T}^{1}_{12}(1.24\mathring{A})\boldsymbol{D}_{6h}$, respectively. The symmetry elements are depicted by the action on the symcell atom C_{000} (indicated by 0). Helix and circle represent action of $\boldsymbol{T}^{w}_{q}$ and $\boldsymbol{C}_n$. Along x-axis is U-axis. Parallelograms are vertical and horizontal mirror planes, while zigzag plane and circle are glide and roto-reflectional plane. Taken from[94].

For some physical applications, like study of the excitations in the external fields (e.g., optical transition or first order Raman spectra), the translational parts of the symmetry transformations are not important. Therefore, for such purposes only the set of all the orthogonal parts X from the line group elements $(X|f)$ is relevant. This set is obviously an axial point group $\boldsymbol{P_I}$, called *isogonal point group*. As it includes all elements of the point factor, $\boldsymbol{P}$ is a subgroup of $\boldsymbol{P_I}$. Note that the elements of $\boldsymbol{P_I}$ being not in $\boldsymbol{P}$ are not the symmetries of the considered system. For an incommensurate line group, the isogonal group is infinite. For the commensurate line groups, the translational group $\boldsymbol{T}$ is an invariant subgroup, and the isogonal group is the factor group $\boldsymbol{P_I} = \boldsymbol{L}/\boldsymbol{T}$.This means that the line group may be partitioned into disjoint cosets:

$$\boldsymbol{L} = \sum_{X \in \boldsymbol{P_I}} (X|f_X)\boldsymbol{T}. \tag{E.0.5}$$

Only when $\boldsymbol{Z} = \boldsymbol{T}$ all of the elements $(X|f_X)$ may be taken from $\boldsymbol{P}$ (having $f_X = 0$), showing that then $\boldsymbol{P_I} = \boldsymbol{P}$. These line groups are called *symmorphic* [94].

The point groups isogonal to the carbon nanotube-line groups, *i.e.*, with the same order of the principal rotational axis, where the rotations include the screw axis operations, are

$$\boldsymbol{D}_q \text{ for chiral} \tag{E.0.6}$$

and

$$\boldsymbol{D}_{2nh} \text{ for achiral tubes.} \tag{E.0.7}$$

Since carbon nanotues line groups are non symmorphic groups because they always contain the screw axis, they. Consequently the isogonal point group is not a subgroup of the full symmetry group.

Among the symmetry operations, that leave the whole tube invariant, those that leave a single atom invariant form the site symmetry of the atom and are called *stabilizers*; the others operations form the *transverlas* of the group. By means of these operation it is possible to restrict the calculation for all the carbon atoms in the unit cell to those atoms that by application of the transversal form the whole system. For example the positions of the atoms of the whole tube can be found from any single carbon atom. Choosing arbitrarily a single carbon atom and applying U-axis operation one maps the atom onto the second atom of the graphene unit cell (hexagon). The applying the n-fold rotation about the tube axis one generates all others hexagons with the first atom on the circumference. The screw-axis operation (without pure translations) map these atoms onto the remaining atoms of the unit cell of the tube. Finally, translating the unit cell by the translational period a the whole tube is formed. The systems for which the symcell is formed by just a single atom to construct the whole system are called *single orbit system*. The stabilizer in chiral tube is the only identity element, because among all the line group operations needed to construct the tube, seen above, the identity is the only one leaving the atom invariant. In achiral tubes there are others symmetries operations that are stabilizers, in fact reflections in the σ_h plane in armchair tubes and in the $\sigma_v$plane in zigzag tubes leave the carbon atom invariant. Thus while in the chiral tubes the site symmetry is $\boldsymbol{C}_1$, for achiral tubes is $\boldsymbol{C}_{1h}$.

Using the symmetry operation is possible to find the position of each single atom of the tube. If the first carbon atom is defined at the position $\frac{1}{3}(\boldsymbol{a}_1 + \boldsymbol{a}_2)$ and the U-axis coincide with the x-axis (see figure E.0.5) , then in cylindrical coordinates the position of the first carbon atom is given by:

$$\boldsymbol{r}_{000} = (r_0,\, \Phi_0,\, z_0) = \left(\frac{d}{2},\, 2\pi\frac{n_1 + n_2}{2N},\, \frac{n_1 - n_2}{2\sqrt{3N}}a_0\right), \tag{E.0.8}$$

where $2N = nq\mathcal{R} = 2\left(n_1^2 + n_1 \cdot n_2 + n_2^2\right)$. Acting on the atom with an element $\left(C_q^w|\frac{na}{q}\right)^t C_n^s U^u$, a new position is obtained

$$\boldsymbol{r}_{tsu} = \left(C_q^w|\frac{na}{q}\right)^t C_n^s U^u \boldsymbol{r}_{000} = \left(\frac{d}{2},\, (-1)^u\Phi_0 + 2\pi\left(\frac{wt}{q} + \frac{s}{n}\right),\, (-1)^u z_0 + \frac{tn}{q}a\right), \tag{E.0.9}$$

where $u = 0, 1$, $s = 0, 1, \ldots, n-1$, and $t = 0, \pm1, \pm2, \ldots$. Below in E.4 are summarized the symmetry properties.

E.0.1 Translational Subgroup

As well as the geometrical descriptor, also the point group symmetry and the translational symmetry of the crystal lattice are incorporated into the formalism that describes the dispersion relations of elementary excitations in a solid.

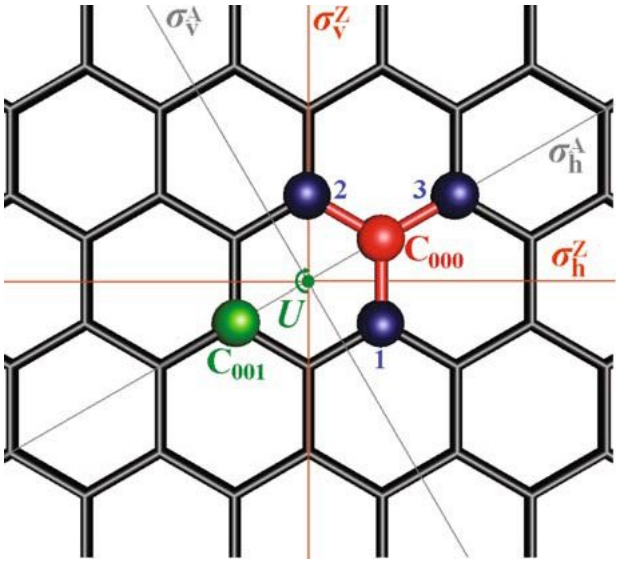

Figure E.0.5: Symcell atom C_{000} and its nearest neighbors 1,2, and 3 at honeycomb. Perpendicular to the plane C_2-axis (green dot with arrow), maps C_{000} to C_{001} and becomes U-axis of the nanotube (along x-axis). Lines depict the graphene mirror planes becoming σ_h and σ_v in the cases of zigzag (superscript Z) and armchair (A) tubes, when the chiral vector is in σ_h and perpendicular to σ_v. Taken from[94].

The way by which the classification of the symmetry properties in reciprocal space involves the concept of group of the wave vector. Considering a symmetry operator $\hat{P}_{(R_\alpha|\boldsymbol{\tau})}$ based on the space group element $(R_\alpha|\boldsymbol{\tau})$ that leaves the periodic potential $V(\boldsymbol{r})$ invariant, $\hat{P}_{(R_\alpha|\boldsymbol{\tau})}V(\boldsymbol{r}) = V(\boldsymbol{r})$. This invariance relation has important implications on the form of the wave function $\psi(\boldsymbol{r})$. In particular considering only translation subgroup $\boldsymbol{T}$ which is a subgroup of the space group, and the translation operator $\hat{P}_{(I|\boldsymbol{\tau})}$ based on the translation group elements $(I|\boldsymbol{\tau})$, the result obtained is $\hat{P}_{(I|\boldsymbol{\tau})}\psi(\boldsymbol{r}) = \psi(\boldsymbol{r}+\boldsymbol{\tau})$. Since every translation operation $\boldsymbol{\tau}$ can be written in terms of translations over the unit vectors $\boldsymbol{a}_i$, $\boldsymbol{\tau} = n_i\boldsymbol{a}_i$ with $i = 1, 2, 3$, it is possible to think the translation operators in each of the $\boldsymbol{a}_i$ directions as commuting operators: $(I|\boldsymbol{\tau}) = (I|\boldsymbol{\tau}_1)\,(I|\boldsymbol{\tau_2})\,(I|\boldsymbol{\tau}_3)$, where $\boldsymbol{\tau}_i = n_i\boldsymbol{a}_i$. The real space lattice vectors produced by the translation operator are denoted by $\boldsymbol{R}_n$. The commutativity of the $(I|\boldsymbol{\tau}_i)$ operations gives three commuting subgroups. Usually is convenient to use periodic boundary conditions and to relate them to cyclic subgroups, so that $(I|\boldsymbol{\tau}_i)^{\mathcal{N}_i} = (I|\boldsymbol{0})$, and $\mathcal{N}_i$ is the number of unit cells along $\boldsymbol{\tau}_i$. In a cyclic subgroup, since all symmetry elements commute with one another, the subgroup is Abelian and has only one-dimensional irreducible matrix representations, whose number equals the number of the group element. Since $(I|\boldsymbol{\tau}_i)^{\mathcal{N}_i} = (I|\boldsymbol{0})$, the irreducible repre-

Table E.4: Summary of the symmetry properties of armchair ($\mathcal{A}$), zigzag ($\mathcal{Z}$), and chiral ($\mathcal{C}$) nanotubes. From the position $\boldsymbol{r}_{000}$ of the first carbon atom the whole tube can be constructed by application of the line group symmetry operations. Taken from[95].

	Tube	Line Group	Isogonal Piont Group		$\boldsymbol{r}_{000}$
$\mathcal{A}$	(n,n)	$\boldsymbol{T}_{2n}\boldsymbol{D}_{nh}$	$\boldsymbol{D}_{2nh}$	$\boldsymbol{L}2n_n/mcm$	$\left(r_0,\ \frac{2\pi}{3n},\ 0\right)$
$\mathcal{Z}$	$(n,0)$	$\boldsymbol{T}_{2n}\boldsymbol{D}_{nh}$	$\boldsymbol{D}_{2nh}$	$\boldsymbol{L}2n_n/mcm$	$\left(r_0,\ \frac{\pi}{n},\ \frac{a_0}{2\sqrt{3}}\right)$
$\mathcal{C}$	(n_1,n_2)	$\boldsymbol{T}_q^w\boldsymbol{D}_n$	$\boldsymbol{D}_q$	$\boldsymbol{L}q_p22$	$\left(r_0,\ 2\pi\frac{n_1+n_2}{2N},\ \frac{n_1-n_2}{2\sqrt{3N}}a_0\right)$

sentation for the cyclic group can be written as a set of matrices which are phase factors or characters of the form $e^{(ik_in_ia_i)}$, and are the $\mathcal{N}_i$ roots of unity. In this context, the wave vector $\boldsymbol{k}$ serves as a quantum number for the translation operator.

At this point is fundamental to introduce the *Bloch's theorem,* which state that if an eigenfunction ψ_k transforms under the translation group according to the irreducible representation labeled by $\boldsymbol{k}$, then $\psi_k(\boldsymbol{r})$ obeys the relation $\hat{P}_{(I|\boldsymbol{\tau})}\psi_k(\boldsymbol{r}) = \psi_k(\boldsymbol{r}+\boldsymbol{\tau}) = e^{i\boldsymbol{k}\cdot\boldsymbol{\tau}}\psi_k(\boldsymbol{r})$ and $\psi_k(\boldsymbol{r})$ can be written in the form $\psi_k(\boldsymbol{r}) = e^{i\boldsymbol{k}\cdot\boldsymbol{r}}u_k(\boldsymbol{r})$, where $u_k(\boldsymbol{r}+\boldsymbol{\tau}) = u_k(\boldsymbol{r})$ has the full translational symmetry of the crystal.

Because of Bloch's theorem, the wave function $\psi(\boldsymbol{r})$ can be written in the form $\psi_k(\boldsymbol{r}) = e^{i\boldsymbol{k}\cdot\boldsymbol{r}}u_k(\boldsymbol{r})$, where $u_k(\boldsymbol{r})$ exhibits the full translational symmetry of the crystal. This result follows from: $\psi_k(\boldsymbol{r}+\boldsymbol{R}_n) = e^{i\boldsymbol{k}\cdot(\boldsymbol{r}+\boldsymbol{R}_n)}u_k(\boldsymbol{r}+\boldsymbol{R}_n) = e^{i\boldsymbol{k}\cdot\boldsymbol{R}_n}\left(e^{i\boldsymbol{k}\cdot\boldsymbol{r}}u_k(\boldsymbol{r})\right)$, where the first equality is obtained using the form given above for the wave function, and the second equality follows from Bloch's theorem. In these terms, Bloch's theorem is simply a statement of the translational symmetry of a crystal. The Bloch functions are the basis functions for the translation group $\boldsymbol{T}$. The wave vector $\boldsymbol{k}$ has a special significance as the *quantum number of translation* and provides a label for the irreducible representations of the translation group. If the crystal has a finite length, then the number of $\boldsymbol{k}$ vectors must be limited in order to insure that the number of irreducible representations is equal to the number of classes. Since the translation group is Abelian, every group element is in a class by itself, so that the number of irreducible representations must equal the number of possible translations. It is important to point out that all of these $\boldsymbol{k}$-vectors are contained within the first Brillouin zone. Thus, if we consider a vector in the extended Brillouin zone $\boldsymbol{k}+\boldsymbol{K}_m$, where $\boldsymbol{K}_m$ is a reciprocal lattice vector, the appropriate phase factor in Bloch's theorem is $e^{i(\boldsymbol{k}+\boldsymbol{K}_m)\cdot\boldsymbol{R}_n} = e^{i\boldsymbol{k}\cdot\boldsymbol{R}_n}$, where equation 2.2.1 has been used [95].

E.0.2 Symmetry of k-vectors and the group of wave vectors

Let $\hat{P}_{(R_\alpha|\mathbf{0})} \equiv \hat{P}_\alpha$ denote a symmetry operator of the point group of the crystal, then $\hat{P}_\alpha \boldsymbol{R}_n$ leaves the crystal invariant. If $\boldsymbol{R}_n$ is a translation operator, being the full symmetry of the lattice preserved, then $\hat{P}_\alpha \boldsymbol{R}_n$ is also a translation operator, *i.e.,* a lattice vector. In the same way $\hat{P}_\alpha \boldsymbol{K}_m$ is a translation operator in reciprocal space. Since $\hat{P}_\alpha \boldsymbol{R}_n$ is a lattice vector, one can write $(\hat{P}_\alpha \boldsymbol{R}_n) \cdot \boldsymbol{K}_m = 2\pi N_2$, where N_2 is an integer, not necessarily the same integer as N_1 in 2.2.1. Being α^{-1} also a symmetry operator of the group, one has $(\hat{P}_{\alpha^{-1}} \boldsymbol{R}_n) \cdot \boldsymbol{K}_m = 2\pi N_3$, and again N_3 is not necessarily the same integer as N_1 or N_2. Moreover, any scalar product, being a constant, must be invariant under any point symmetry operator. Therefore, performing the same symmetry operation on each member of the scalar product in the last relation, the scalar product has to remain invariant $\hat{P}_\alpha(\hat{P}_{\alpha^{-1}} \boldsymbol{R}_n) \cdot \boldsymbol{K}_m = 2\pi N_3 = \boldsymbol{R}_n \cdot (\hat{P}_\alpha \boldsymbol{K}_m)$. These last three equations give several results:

1. If $\hat{P}_\alpha$ is a symmetry operator of a point group of a crystal, and $\boldsymbol{R}_n$ is lattice vectors, then $\hat{P}_{\alpha^{-1}} \boldsymbol{R}_n$ is a lattice vector too. Analogously, if $\boldsymbol{K}_m$ is a reciprocal lattice vector, then $\hat{P}_\alpha \boldsymbol{K}_m$ is reciprocal lattice vectors too.

2. The effect of an operator $\hat{P}_\alpha$ on a direct lattice vector $\boldsymbol{R}_n$ is equivalent to the effect of operator $\hat{P}_{\alpha^{-1}}$ on the corresponding reciprocal lattice vector $\boldsymbol{K}_m$.

By definition, the *group of the wave vector* is formed by the *set of space group operations which transform* $\boldsymbol{k}$ *into itself, or into an equivalent* $\boldsymbol{k} = \boldsymbol{k} + \boldsymbol{K}_m$ *vector*. The addition of $\boldsymbol{K}_m$ does not change the energy of the system, in fact $e^{i\boldsymbol{k}\cdot\boldsymbol{R}_n} = e^{i(\boldsymbol{k}+\boldsymbol{K}_m)\cdot\boldsymbol{R}_n}$, which states that both $\boldsymbol{k}$ and $\boldsymbol{k} + \boldsymbol{K}_m$ belong to the *same translational irreducible representation*. The space group itself forms the group of the wave vector at $\boldsymbol{k} = 0$ because all the symmetry operations of the space group take the point $\boldsymbol{k} = 0$ into itself. Moreover, the group of the wave vector for nonzone center $\boldsymbol{k}$-vectors ($\boldsymbol{k} \neq 0$) remains a subgroup of the space group for $\boldsymbol{k} = 0$.

Consider the *action of the point group operations on a general vector* $\boldsymbol{k}$ in reciprocal space, not necessarily a reciprocal lattice vector. *The star of* $\boldsymbol{k}$ is defined as the set of wave vectors $\boldsymbol{k'}$ that are obtained by carrying out all the point group operations on $\boldsymbol{k}$. If $\boldsymbol{k}$ is a general point in the Brillouin zone, then only the identity will take $\boldsymbol{k}$ into itself and in this case the wave functions describing electron states only see the translational symmetry $(I|\boldsymbol{\tau})$ of the space group. On the other hand, if the $\boldsymbol{k}$-vector under consideration lies on a symmetry axis or is at a high symmetry point in the Brillouin zone, then perhaps several of the point group operations will transform $\boldsymbol{k}$ into itself or into an equivalent $\boldsymbol{k}$-vector $\boldsymbol{k} + \boldsymbol{K}_m$. Thus the star of $\boldsymbol{k}$ is formed by consideration of $\hat{P}_\alpha \boldsymbol{k}$ for all operators $\hat{P}_\alpha$ for the point group. Those $\hat{P}_\alpha$ for which $\hat{P}_\alpha \boldsymbol{k} = \boldsymbol{k} + \boldsymbol{K}_m$, where $\boldsymbol{K}_m$ is a reciprocal lattice vector (including $\boldsymbol{K}_m = 0$) form the group of the wave vector [95].

E.0.3 Effect of Translations and Point Group Operations on Bloch Functions

Let's now consider the effect of the symmetry operations on $\boldsymbol{k}$ respect to the eigenfunctions of Schrödinger's equation. From Bloch's theorem is known that the action of any pure translation operator $\hat{P}_{(I|\boldsymbol{\tau})}$ on wave function $\psi_k(\boldsymbol{r})$ (where $\boldsymbol{\tau} = \boldsymbol{R}_n$) gives a wave function $e^{i\boldsymbol{k}\cdot\boldsymbol{R}_n}\psi_k(\boldsymbol{r})$

$$\hat{P}_{(I|\boldsymbol{\tau})}\psi_k(\boldsymbol{r}) = e^{i\boldsymbol{k}\cdot\boldsymbol{\tau}}\psi_k(\boldsymbol{r}). \tag{E.0.10}$$

The translation vectors, each corresponding to the energy $E(\boldsymbol{k})$, labels the wave functions of this functional form. Therefore there will be as many Bloch functions as translation vector. These functions provide basis functions for irreducible representations for the group of the wave vector. As explained in the previous section, if $\boldsymbol{k}$ is a general point in the Brillouin zone, then the star of $\boldsymbol{k}$ contains wave vectors all equivalent to $\boldsymbol{k}$ from a physical standpoint. The space group for a general wave vector $\boldsymbol{k}$ will contain only the symmetry elements $(I|\boldsymbol{R}_n)$, because in this case all the $\boldsymbol{k}$-vectors are distinct. A wave vector having *higher symmetry*, for which operations $\hat{P}_\beta\boldsymbol{k} = \boldsymbol{k} + \boldsymbol{K}_m$ transform $\boldsymbol{k}$ into an equivalent wave vector, the space group of the wave vector contains the symmetry element $(\beta|\boldsymbol{R}_n)$ with equal energy at equivalent $\boldsymbol{k}$ points. A degeneracy in the energy bands will occur if the point group of the wave vector contains irreducible representations that have more than one dimension. Therefore along high symmetry axes and at high symmetry points bands tend to "stick together". The effect of a point group operation on this eigenfunction is $\hat{P}_{(R_\alpha|\boldsymbol{0})}\psi_{\boldsymbol{k}}(\boldsymbol{r}) = \hat{P}_{(R_\alpha|\boldsymbol{0})}e^{i\boldsymbol{k}\cdot\boldsymbol{r}}u_{\boldsymbol{k}}(\boldsymbol{r})$, where the eigenfunction is written in the Bloch form. To maintain invariance of scalar products one have to require $\boldsymbol{k}\cdot R_{\alpha^{-1}}\boldsymbol{r} = R_\alpha\boldsymbol{k}\cdot\boldsymbol{r}$, being the effect of a point group operation on a function equivalent to preserve the form of the function and rotate the coordinate system in the opposite sense. If $u_{R_\alpha\boldsymbol{k}}(\boldsymbol{r}) \equiv u_{\boldsymbol{k}}(R_{\alpha^{-1}}\boldsymbol{r})$ for the periodic part of the Bloch function and denoting the transformed wave vector by $\boldsymbol{k} \equiv R_\alpha\boldsymbol{k}$, then one has $\hat{P}_{(R_\alpha|\boldsymbol{0})}\psi_{\boldsymbol{k}}(\boldsymbol{r}) = e^{iR_\alpha\boldsymbol{k}\cdot\boldsymbol{r}}u_{R_\alpha\boldsymbol{k}}(\boldsymbol{r}) \equiv \psi_{R_\alpha\boldsymbol{k}}(\boldsymbol{r})$, which is of the Bloch form, because operating with the translation operator on $\psi_{R_\alpha\boldsymbol{k}}(\boldsymbol{r})$ one obtain $\hat{P}_{(I|\boldsymbol{\tau})}\psi_{R_\alpha\boldsymbol{k}}(\boldsymbol{r}) = \hat{P}_{(I|\boldsymbol{\tau})}e^{iR_\alpha\boldsymbol{k}\cdot\boldsymbol{r}}u_{\boldsymbol{k}}(R_{\alpha^{-1}}\boldsymbol{r}) = e^{iR_\alpha\boldsymbol{k}\cdot(\boldsymbol{r}+\boldsymbol{\tau})}u_{\boldsymbol{k}}(R_{\alpha^{-1}}\boldsymbol{r}+R_{\alpha^{-1}}\boldsymbol{\tau})$. Because of the periodicity of $u_{\boldsymbol{k}}(\boldsymbol{r})$ one has $u_{R_\alpha\boldsymbol{k}}(\boldsymbol{r}+\boldsymbol{\tau}) = u_{\boldsymbol{k}}(R_{\alpha^{-1}}\boldsymbol{r} + R_{\alpha^{-1}}\boldsymbol{\tau}) = u_{\boldsymbol{k}}(R_{\alpha^{-1}}\boldsymbol{r}) = u_{R_\alpha\boldsymbol{k}}(\boldsymbol{r})$

and noting the orthonormality relation 2.2.1 for the plane wave factor, one gets $\hat{P}_{(I|\boldsymbol{\tau})}\psi_{R_\alpha\boldsymbol{k}}(\boldsymbol{r}) = e^{iR_\alpha\boldsymbol{k}\cdot\boldsymbol{\tau}}u_{R_\alpha\boldsymbol{k}}(\boldsymbol{r})$ where $u_{R_\alpha\boldsymbol{k}}(\boldsymbol{r})$ is periodic in the direct lattice. The eigenfunctions $\psi_{R_\alpha\boldsymbol{k}}(\boldsymbol{r})$ thus forms basis functions for the $R_\alpha\boldsymbol{k}$-th irreducible representation of the translation group $\boldsymbol{T}$. As said in the previous section, the "star of k" is the set of distinct wave vectors in $\boldsymbol{k}$-space which can be generated by operating on one $\boldsymbol{k}$ vector by all the symmetry elements of the point group.

Considering the above arguments on symmorphic groups for simplicity, where the point group is isomorphic to $\boldsymbol{G}/\boldsymbol{T}$ (where $\boldsymbol{G}$ is the space group) and $\hat{P}_{(R_\alpha|\boldsymbol{\tau})} =$

$\hat{P}_{(I|\boldsymbol{\tau})}\hat{P}_{(R_\alpha|\mathbf{0})}$, one obtains:

$$\hat{P}_{(R_\alpha|\boldsymbol{\tau})}\psi_{\boldsymbol{k}}(\boldsymbol{r}) = \hat{P}_{(I|\boldsymbol{\tau})}\hat{P}_{(R_\alpha|\mathbf{0})}\psi_{\boldsymbol{k}}(\boldsymbol{r}) = \hat{P}_{(I|\boldsymbol{\tau})}\psi_{R_\alpha\boldsymbol{k}}(\boldsymbol{r}) = e^{iR_\alpha\boldsymbol{k}\cdot\boldsymbol{\tau}}\psi_{R_\alpha\boldsymbol{k}}(\boldsymbol{r}).$$

Similarly $\hat{P}_{(R_\beta|\boldsymbol{\tau})}\psi_{R_\alpha\boldsymbol{k}}(\boldsymbol{r}) = e^{iR_\beta R_\alpha\boldsymbol{k}\cdot\boldsymbol{\tau}}\psi_{R_\beta R_\alpha\boldsymbol{k}}(\boldsymbol{r})$. Therefore, since the product operation $R_\beta R_\alpha$ is contained in the point group, by taking the star of $\boldsymbol{k}$ one spans the invariant subspace of the point group and obtains the set of eigenfunctions $\psi_{R_\alpha\boldsymbol{k}}(\boldsymbol{r})$. If h is the order of the point group, then there are h functions in the set $\psi_{R_\alpha\boldsymbol{k}}(\boldsymbol{r})$. Here $\boldsymbol{k}$ completely specifies all these representations, which are equally well specified by any of the $\boldsymbol{k}$ vectors in the star of $\boldsymbol{k}$. Although all the functions in the set $\psi_{R_\alpha\boldsymbol{k}}(\boldsymbol{r})$ correspond to the same energy, one does not say that the functions $\psi_{\boldsymbol{k}}(\boldsymbol{r})$ and $\psi_{R_\alpha\boldsymbol{k}}(\boldsymbol{r})$ are degenerate. Instead one consider the extra point group symmetry to yield the relation $E(\boldsymbol{k}) = E(R_\alpha\boldsymbol{k})$ for all R_α and write $\psi_{\boldsymbol{k}}(\boldsymbol{r})$ for all the functions in the set $\psi_{R_\alpha\boldsymbol{k}}(\boldsymbol{r})$. In this way, it is guaranteed that the energy $E(\boldsymbol{k})$ shows the full point group symmetry of the reciprocal lattice. Thus for the two-dimensional hexagonal lattice, it is only necessary to calculate $E(\boldsymbol{k})$ explicitly for $\boldsymbol{k}$ points in 1/6 of the Brillouin zone contained within the sector ΓMK . These statements are generally valid for nonsymmorphic groups as well. The term "degeneracy" is used to describe states with exactly the same energy and the same wave vector. These degeneracies, which are called "essential", are produced by the symmetry restrictions at special high symmetry points or special k points in the Brillouin zone. On the contrary "accidental" (or "nonessential") degeneracies occur at arbitrary k points. *"Special" high symmetry points* in the Brillouin zone are those for which $R_\alpha\boldsymbol{k} = \boldsymbol{k}+\boldsymbol{K}_m$,where $\boldsymbol{K}_m$ is the reciprocal lattice vector including $\boldsymbol{K}_m = 0$. In the cases where the symmetry operation yields $R_\alpha\boldsymbol{k} = \boldsymbol{k} + \boldsymbol{K}_m$, being possible to have degenerate eigenfunctions with the same energy eigenvalue at the same $\boldsymbol{k}$ vector, then the eigenfunctions have essential degeneracies [95].

Bibliography

[1] Whitesides GM. The "right" size in nanobiotechnology. Nat Biotech. 2003;21:1161–1165.

[2] Lowe CR. Nanobiotechnology: The fabrication and applications of chemical and biological nanostructures. Curr Opin Chem Biol. 2000;10:428–434.

[3] Wang L, Zhao W, Tan W. Bioconjugated silica nanoparticles: Development and applications. Nano Res. 2008;1:99–115.

[4] Iijima S. Helical microtubules of graphitic carbon. Nature. 1991;354:56–58

[5] Dai H. Carbon nanotubes: Synthesis, integration, and properties. Acc Chem Res. 2002;35:1035–1044.

[6] Dresselhaus M, Dai H. MRS 2004 Carbon Nanotube Special Issue. Vol. 29. 2004.

[7] Golberg D, Costa PMFJ, Mitome M, Bando Y. Nanotubes in a gradient electric field as revealed by STM–TEM technique. Nano Res. 2008;1:166–175.

[8] Zhou W, Rutherglen C, Burke P. Wafer scale synthesis of dense aligned arrays of singlewalled carbon nanotubes. Nano Res. 2008;1:158–165.

[9] S.Reich,C.Thomsean, J.Maultzsch, Carbon Nanotubes: Basic Concepts and Physical Properties, Wiley-VCH Verlag, Weinheim, 2004.

[10] R.Saito, G.Dresselhaus, M.S.Dresselhaus, Physical Properties of Carbon Nanotubes, Imperial College Press, London, 1998.

[11] Z. Liu, S.Tabakman, K.Welsher, H.Dai, Carbon Nanotubes in Biology and Medicine: *In vitro* and *in vivo* Detection, Imaging and Drug delivery.Nano Res. 2009 Feb 1;2(2):85-120.

[12] IUPAC. Compendium of Chemical Terminology, 2nd ed. (the "Gold Book"). Compiled by A. D. McNaught and A. Wilkinson. Blackwell Scientific Publications, Oxford (1997). XML on-line corrected version: http://goldbook.iupac.org (2006-) created by M. Nic, J. Jirat, B. Kosata; updates compiled by A. Jenkins. ISBN 0-9678550-9-8. doi:10.1351/goldbook

[13] Liu Z, Sun X, Nakayama N, Dai H. Supramolecular chemistry on water--soluble carbon nanotubes for drug loading and delivery. ACS Nano. 2007;1:50–56.

[14] Kam NWS, O'Connell M, Wisdom JA, Dai H. Carbon nanotubes as multifunctional biological transporters and nearinfrared agents for selective cancer cell destruction. A setup for control the humidity and the external temperatureProc Natl Acad Sci USA. 2005;102:11600–11605.

[15] Welsher K, Liu Z, DD, Dai H. Selective probing and imaging of cells with single walled carbon nanotubes as nearinfrared fluorescent molecules. Nano Lett. 2008;8:586–590.

[16] Kam NWS, Liu Z, Dai H. Functionalization of carbon nanotubes via cleavable disulfide bonds for efficient intracellular delivery of siRNA and potent gene silencing. J Am Chem Soc. 2005;127:12492–12493.

[17] Liu Z, Chen K, Davis C, Sherlock S, Cao Q, Chen X, Dai H. Drug delivery with carbon nanotubes for in vivo cancer treatment. Cancer Res. 2008;68:6652–6660

[18] Liu Z, Cai WB, He LN, Nakayama N, Chen K, Sun XM, Chen XY, Dai HJ. In vivo biodistribution and highly efficient tumour targeting of carbon nanotubes in mice. Nat Nanotech. 2007;2:47–52.

[19] Liu Z, Davis C, Cai W, He L, Chen X, Dai H. Circulation and long-term fate of functionalized, biocompatible singlewalled carbon nanotubes in mice probed by Raman spectroscopy. Proc Natl Acad Sci USA. 2008;105:1410–1415.

[20] Liu Z, Winters M, Holodniy M, Dai HJ. siRNA delivery into human T cells and primary cells with carbonnanotube transporters. Angew Chem Int Ed. 2007;46:2023–2027.

[21] Lam CW, James JT, McCluskey R, Hunter RL. Pulmonary toxicity of singlewall carbon nanotubes in mice 7 and 90 days after intratracheal instillation. Toxicol Lett. 2004;77:126–134.

[22] Warheit DB, Laurence BR, Reed KL, Roach DH, Reynolds GAM, Webb TR. Comparative pulmonary toxicity assessment ofsinglewall carbon nanotubes in rats. Toxicol Lett. 2004;77:117–125.

[23] Shvedova AA, Kisin ER, Mercer R, Murray AR, Johnson VJ, Potapovich AI, Tyurina YY, Gorelik O, Arepalli S, SchweglerBerry D, et al. Unusual inflammatory and fibrogenic pulmonary responses to singlewalled carbon nanotubes in mice. Am J Phys Lung Cell Mol Physiol. 2005;289:L698–L708.

[24] Muller J, Huaux F, Moreau N, Misson P, Heilier JF, Delos M, Arras M, Fonseca A, Nagy JB, Lison D. Respiratory toxicity of multiwall carbon nanotubes. Toxicol Appl Pharmacol. 2005;207:221–231.

[25] Kam NWS, Jessop TC, Wender PA, Dai HJ. Nanotube molecular transporters: Internalization of carbon nanotubeprotein conjugates into mammalian cells. J Am Chem Soc. 2004;126:6850–6851.

[26] Dumortier H, Lacotte S, Pastorin G, Marega R, Wu W, Bonifazi D, Briand JP, Prato M, Muller S, Bianco A. Functionalized carbon nanotubes are noncytotoxic and preserve the functionality of primary immune cells. Nano Lett. 2006;6:1522–1528.

[27] Schipper ML, NakayamaRatchford N, Davis CR, Kam NWS, Chu P, Liu Z, Sun X, Dai H, Gambhir SS. A pilot toxicology study of single-walled carbon nanotubes in a small sample of mice. Nat Nanotech. 2008;3:216–221.

[28] Chen RJ, Zhang YG, Wang DW, Dai HJ. Noncovalent sidewall functionalization of single-walled carbon nanotubes for protein immobilization. J Am Chem Soc. 2001;123:3838–3839.

[29] Wu P, Chen X, Hu N, Tam UC, Blixt O, Zettl A, Bertozzi CR. Biocompatible carbon nanotubes generated by functionalization with glycodendrimers. Angew Chem Int Ed. 2008;47:5022–5025.

[30] Zheng M, Jagota A, Semke ED, Diner BA, Mclean RS, Lustig SR, Richardson RE, Tassi NG. DNA-assisted dispersion and separation of carbon nanotubes. Nat Mater. 2003;2:338–342.

[31] Tu X, Zheng M. A DNAbased approach to the carbon nanotube sorting problem. Nano Res. 2008;1:185–194.

[32] Welsher K., Liu Z.,Sherlock S.P.,Robinson J.T., Chen Z., daranciang D., Dai H. A route to brightly fluorescent carbon nanotubes for near-infrared imaging in mice. Nat Nanotech. 2009; 4(11): 773-780.

[33] Pantarotto D, Briand JP, Prato M, Bianco A. Translocation of bioactive peptides across cell membranes by carbon nanotubes. Chem Commun. 2004:16–17.

[34] Bianco A, Kostarelos K, Partidos CD, Prato M. Biomedical applications of functionalised carbon nanotubes. Chem Commun. 2005:571–577.

[35] Heller DA, Baik S, Eurell TE, Strano MS. Singlewalled carbon nanotube spectroscopy in live cells: Towards longterm labels and optical sensors. Adv Mater. 2005;17:2793–2799.

[36] Kam NWS, Liu ZA, Dai HJ. Carbon nanotubes as intracellular transporters for proteins and DNA: An investigation of the uptake mechanism and pathway. Angew Chem Int Ed. 2006;45:577–581.

[37] Chin SF, Baughman RH, Dalton AB, Dieckmann GR, Draper RK, Mikoryak C, Musselman IH, Poenitzsch VZ, Xie H, Pantano P. Amphiphilic helical peptide enhances the uptake of singlewalled carbon nanotubes by living cells. Exper Biol Med. 2007;232:1236–1244.

[38] Jin H, Heller DA, Strano MS. Single particle tracking of endocytosis and exocytosis of single-walled carbon nanotubes in NIH3T3 cells. Nano Lett. 2008;8:1577–1585.

[39] Kostarelos K, Lacerda L, Pastorin G, Wu W, Wieckowski S, Luangsivilay J, Godefroy S, Pantarotto D, Briand JP, Muller S, et al. Cellular uptake offunctionalized carbon nanotubes is independent offunctional group and cell type. Nat Nanotech. 2007;2:108–113.

[40] Dhar S, Liu Z, Thomale J, Dai H, Lippard SJ. Targeted singlewall carbon nanotubemediated Pt(IV) prodrug delivery using folate as a homing device. J Am Chem Soc. 2008;130:11467–11476.

[41] Zhang ZH, Yang XY, Zhang Y, Zeng B, Wang ZJ, Zhu TH, Roden RBS, Chen YS, Yang RC. Delivery of telomerase reverse transcriptase small interfering RNA in complex with positively charged singlewalled carbon nanotubes suppresses tumor growth. Clin Cancer Res. 2006;12:4933–4939.

[42] Mankoff D A, J. Nucl. Med. A definition of Molecular Imaging. 48 (2007) 18N.

[43] Hong H, Gao T, Cai W. Molecular imaging with single-walled carbon nanotubes. Nano Today (2009)4, 252-261.

[44] Yum K, McNicholas TP, Mu B, Strano MS, Single-Walled Carbon Nanotube-Based Near-Infrared Optical Glucose Sensors toward *In Vivo* Continuous Glucose Monitoring. J Diabetes Sci Technol. 2013 Jan; 7(1): 72-87.

[45] O'Connell MJ, Bachilo SM, Huffman CB, Moore VC, Strano MS, Haroz EH, Rialon KL, Boul PJ, Noon WH, Kittrell C, et al. Band gap fluorescence from individual singlewalled carbon nanotubes. Science. 2002;297:593–596.

[46] Leeuw TK, Reith RM, Simonette RA, Harden ME, Cherukuri P, Tsyboulski DA, Beckingham KM, Weisman RB. Singlewalled carbon nanotubes in the intact organism: NearIR imaging and biocompatibility studies in Drosophila. Nano Lett. 2007;7:2650–2654.

[47] Cherukuri P, Bachilo SM, Litovsky SH, Weisman RB. Nearinfrared fluorescence microscopy of singlewalled carbon nanotubes in phagocytic cells. J Am Chem Soc. 2004;126:15638–15639.

[48] Cherukuri P, Gannon CJ, Leeuw TK, Schmidt HK, Smalley RE, Curley SA, Weisman RB. Mammalian pharmacokinetics of carbon nanotubes using intrinsic nearinfrared fluorescence. Proc Natl Acad Sci USA. 2006;103:18882–18886.

[49] Jeng ES, Moll AE, Roy AC, Gastala JB, Strano MS. Detection of DNA hybridization using the nearinfrared bandgap fluorescence of singlewalled carbon nanotubes. Nano Lett. 2006;6:371–375.

[50] Barone PW, Baik S, Heller DA, Strano MS. Near-infrared optical sensors based on single-walled carbon nanotubes. Nat Mater. 2004;4:86–92.

[51] Satishkumar BC, Brown LO, Gao Y, Wang CC, Wang HL, Doorn SK. Reversible fluorescence quenching in carbon nanotubes for biomolecular sensing. Nat Nanotech. 2007;2:560–564.

[52] Reich S, Dworzak M, Hoffmann A, Thomsen C, Strano MS. Excited-state carrier lifetime in singlewalled carbon nanotubes. Phys Rev B. 2005;71:033402.

[53] Cognet L, Tsyboulski DA, Rocha JDR, Doyle CD, Tour JM, Weisman RB. Stepwise quenching of exciton fluorescence in carbon nanotubes by singlemolecule reactions. Science. 2007;316:1465–1468.

[54] Heller DA, Mayrhofer RM, Baik S, Grinkova YV, Usrey ML, Strano MS. Concomitant length and diameter separation of single-walled carbon nanotubes. J Am Chem Soc. 2004;126:14567–14573.

[55] Wang F, Dukovic G, Brus LE, Heinz TF. Time-resolved fluorescence of carbon nanotubes and its implication for radiative lifetimes. Phys Rev Lett. 2004;92:177401.

[56] Lefebvre J, Austing DG, Bond J, Finnie P. Photoluminescence imaging of suspended single-walled carbon nanotubes. Nano Lett. 2006;6:1603–1608.

[57] Rao AM, Richter E, Bandow S, Chase B, Eklund PC, Williams KA, Fang S, Subbaswamy KR, Menon M, Thess A, et al. Diameter-selective Raman scattering from vibrational modes in carbon nanotubes. Science. 1997;275:187–191.

[58] Liu Z, Li X, Tabakman SM, Jiang K, Fan S, Dai H. Multiplexed multicolor Raman imaging of live cells with isotopically modified single walled carbon nanotubes. J Am Chem Soc. 2008;130:13540–13541.

[59] Ruoslahti, Erkki; Pierschbacher, Michael D. "Arg-Gly-Asp: a versatile cell recognition signal". Cell. (1986). 44 (4): 517–18.

[60] Keren S, Zavaleta C, Cheng Z, de la Zerda A, Gheysens O, Gambhir SS. Noninvasive molecular imaging of small living subjects using Raman spectroscopy. Proc Nat Acad Sci USA. 2008;105:5844–5849.

[61] Zavaleta C, Zerda Adl, Liu Z, Keren S, Cheng Z, Schipper M, Chen X, Dai H, Gambhir SS. Noninvasive Raman spectroscopy in living mice for evaluation of tumor targeting with carbon nanotubes. Nano Lett. 2008;8:2800–2805.

[62] Chakravarty P, Marches R, Zimmerman NS, Swafford AD, Bajaj P, Musselman IH, Pantano P, Draper RK, Vitetta ES. Thermal ablation oftumor cells with antibodyfunctionalized singlewalled carbon nanotubes. Proc Natl Acad Sci USA. 2008;105:8697–8702.

[63] Xu MH, Wang LHV. Photoacoustic imaging in biomedicine. Rev Sci Instrum. 2006;77:041101.

[64] Zerda Adl, Zavaleta C, Keren S, Vaithilingam S, Bodapati S, Liu Z, Levi J, Ma TJ, Oralkan O, Cheng Z, et al. Photoacoustic molecular imaging in living mice utilizing targeted carbon nanotubes. Nat Nanotech. 2008;3:557–562.

[65] P. Avouris, Z. Chen, V. Perebeinos, Carbon-based electronics, Nature Nanotech. 2, 605-615 (2007)

[66] R. Bruce Weisman, Optical Spectroscopy of Single-Walled Carbon Nanotubes. Contemporary Concept of Condensed Matter Science, Volume 3: Nanotubes (Elsevier).

[67] L. Mino, G. Agostini, E. Borfecchia, D. Gianolio, A. Piovano, E. Gallo and C. Lamberti1, Low-dimensional systems investigated by x-ray absorption spectroscopy: a selection of 2D, 1D and 0D cases. 2013 J. Phys. D: Appl. Phys. 46 423001

[68] T.Ando, Theory of Electronic States and Transport in Carbon Nanotubes, Journal of the Physical Society of Japan Vol. 74, No. 3, March, 2005, pp. 777–817

[69] J.Lefebvre, S. Maruyama and P. Finnie, Photoluminescence in Science and application, Topic in Applied Physics 111: Carbon Nanotubes, 287–319, Berlin (2008).

[70] W Y Liang 1970 Phys. Educ. 5 226

[71] C. D. Spataru, S. Ismail-Beigi, R. B. Capaz and S. G. Louie, Quasiparticle and Excitonic Effects in the Optical Response of Nanotubes and Nanoribbons, Topic in Applied Physics 111: Carbon Nanotubes, 287–319, Berlin (2008).

[72] James W. Robinson, Atomic spetroscopy, 2nd ed.,rev.and expanded, Marcel Dekker, Inc. 1996

[73] N.M. Uzunov, K. Atroshchenko, C.L. Fontana, M. Bello, A. Rosato, L. Melendez-Alafort, L. Manov, E. Menna, P. Salice, G. Moschini, Study of Photoluminescence Properties of Single-Walled Carbon Nanotube, INFN-LNL Report 239 (2013), available URL: http://www.lnl.infn.it/~annrep/read_ar/2012/index_contrib.htm .

[74] Y. Y. Huang and E. M. Terentjev , Dispersion of Carbon Nanotubes: Mixing, Sonication, Stabilization, and Composite Properties, Polymers 4 (2012) 275 doi:10.3390/polym4010275.

[75] https://www.thorlabs.com/thorproduct.cfm?partnumber=M9-830-0150

[76] Bahaa E. A. Saleh, Malvin Carl Teich. Fundamentals of Photonics. Whiley, 2007.

[77] http://www.hamamatsu.com/resources/pdf/ssd/C11482GA_kacc1212e.pdf

[78] http://www.hamamatsu.com/resources/pdf/ssd/mini-spectrometer_kacc9003e.pdf

[79] http://www.hamamatsu.com/resources/pdf/ssd/g9203-256d_etc_kmir1013e.pdf

[80] De Rosa M., De Nardo L., Bello M., Uzunov N., Electronic setup for fluorescence emission measurements and long-time constant-temperature maintenance of Single-Walled Carbon Nano-Tubes in water solutions, ASN, Vol 4, No 1, Pages 61-69, 2017.

[81] T. Guo, P. Nikolaev, A. Thess, D. T. Colbert, R. E. Smalley, Catalytic growth of single-walled nanotubes by laser vaporization Chem. Phys. Lett. 1995, 243 (1, 2), 49-54.

[82] M. Endo, K. Takeuchi, S. Igarashi, K. Kobori, M. Shiraishi, H. W. Kroto , The production and structure of pyrolytic carbon nanotubes (PCNTs), J. Phys. Chem. Solids 1993, 54 (12), 1841-1848.

[83] Ebbesen, T. W.; Ajayan, P. M., Large-scale synthesis of carbon nanotubes, Nature 1992, 358 (6383), 220- 222.

[84] Y. Tan, D. Resasco, Dispersion of Single-Walled Carbon Nanotubes of Narrow Diameter Distribution, J. Phys.Chem. B, 109, 14454, 2005.

[85] W. Wenseleers, I. I. Vlasov, E. Goovaerts, E. D. Obraztsova, A. S. Lobach, A. Bouwen, Efficient Isolation and Solubilization of Pristine Single-walled Nanotubes in Bile Salts Micelles, AdV. Funct. Mater. 2004, 14, 1105.

[86] S. Lin, D. Blankschtein, Role of the Bile Salt Surfactant Sodium Cholate in Enhancing the Aqueous Dispersion Stability of Single-Walled Carbon Nanotubes: A Molecular Dynamics Simulation Study, J. Phys. Chem. B, 2010, 114, 15616–15625.

[87] S. Lin, A. J. Hilmer, J. D. Mendenhall, M. S. Strano, D. Blankschtein, Molecular Perspective on Diazonium Adsorption for Controllable Functionalization of Single-Walled Carbon Nanotubes in Aqueous Surfactant Solutions, J. Am. Chem. Soc. 2012, 134, 8194−8204.

[88] Strano, M. et al., The role of surfactant adsorption during ultrasonication in the dispersion of single-walled carbon nanotubes, J. Nanosci. Nanotechnol., 3 (1/2), 81, 2003.

[89] B. Kitiyanan, W.E. Alvarez, J.H. Harwell, D.E. Resasco, Controlled production of single-wall carbon nanotubes by catalytic decomposition of CO on bimetallic Co–Mo catalysts, Chem. Phys. Lett. 2000, 317 (3, 4, 5), 497-503.

[90] N. Nair, M. L. Usrey, W. Kim, R. D. Braatz, M. S. Strano, Estimation of the (n,m) Concentration Distribution of Single-Walled Carbon Nanotubes from Photoabsorption Spectra, Anal. Chem. 2006, 78, 7689-7696.

[91] R. B. Weisman , S. M. Bachilo, Dependence of Optical Transition Energies on Structure for Single-Walled Carbon Nanotubes in Aqueous Suspension: An Empirical Kataura Plot, Nano Lett., Vol. 3, No. 9, 2003.

[92] M. Jones, C. Engtrakul, W. K. Metzger, R. J. Ellingson, A. J. Nozik, M. J. Heben, G. Rumbles, Analysis of photoluminescence from solubilized single-walled carbon nanotubes, PHYSICAL REVIEW B 71, 115426 (2005).

[93] Giuseppe Grosso, Giuseppe Pastori Parravicini, Solid State Physics, Academic Press,2000.

[94] Damnjanovic M., Milosevic I., Line Groups in Physics, Lect. Notes Phys. 801 (Springer, Berlin Heidelberg 2010), DOI 10.1007/978-3-642-11172-3

[95] M.S. Dresselhaus G. Dresselhaus A. Jorio, Group Theory Application to the Physics of Condensed Matter (Springer, Berlin Heidelberg 2008), DOI 10.1007/978-3-540-32899-8

[96] A.Cotton, Chemical Application of Group Theory,J.Wiley& Sons, 3rd Edition,1990.

[97] Hart D., Power Electronics. McGraw - HIll. (2010)

[98] https://en.wikipedia.org/wiki/Pulse-width_modulation

[99] https://www.its.bldrdoc.gov/fs-1037/dir-013/_1849.htm